Space Charge Pulsed Electro Acoustic Method, Calibration for Flat Samples and Crosstalk Reduction for HVDC Cable Measurements

Mier Escurra, G.A.

DOI
10.4233/uuid:7fa4684e-87f9-45fa-b283-7b79e3679883

Publication date
2022

Document Version
Final published version

Citation (APA)
Mier Escurra, G. A. (2022). *Space Charge Pulsed Electro Acoustic Method, Calibration for Flat Samples and Crosstalk Reduction for HVDC Cable Measurements*. [Dissertation (TU Delft), Delft University of Technology]. https://doi.org/10.4233/uuid:7fa4684e-87f9-45fa-b283-7b79e3679883

Space Charge Pulsed Electro Acoustic Method, Calibration for Flat Samples and Crosstalk Reduction for HVDC Cable Measurements

Dissertation

for the purpose of obtaining the degree of doctor
at Delft University of Technology
by the authority of the Rector Magnificus, prof. dr. ir. T.H.J.J. van der Hagen,
chair of the Board for Doctorates
to be defended publicly on
Tuesday 22 February 2022 at 15:00 o'clock

By

Guillermo Andres MIER ESCURRA

Master of Science in Electrical Engineering
Delft University of Technology, The Netherlands

Born in Aguascalientes, México

This dissertation has been approved by the promotors.

Composition of the doctoral committee:

Rector Magnificus,	Chairperson
Prof. ir. P.T.M. Vaessen	Delft University of Technology, promotor
Prof. dr. ir. P. Bauer	Delft University of Technology, promotor
Dr. A. Rodrigo Mor	Delft University of Technology, copromotor

Independent members:

Prof. Dr. P. Palenski	Delft University of Technology
Prof. Dr. P.C.J.M. van der Wielen	Eindhoven University of Technology
Dr. M. Mudarra López	Polytechnic University Catalunya
Prof. Dr. S. Holé	École supérieure de physique et de chimie industrielles de la Ville de Paris
Prof. Dr. ir. A.H.M. Smets	Delft University of Technology, reserve member

Printed by IPSKAMP printing

ISBN 978-94-6421-645-5

An electronic copy of this dissertation is available at http://repository.tudelft.nl

When in doubt, ride the horse in the direction it is going.

Werner Erhard

Table of Contents

Summary

The continuous increase of HVDC technologies in the energy sector has inherently increased the demand of HVDC cables aiming towards higher voltages. There are several advantages to the use of extruded polymeric cables against mass impregnated cables, but in contrast to HVAC cables, their usage has been restricted due to premature aging and breakdown attributed to the formation of space charges. This is the motivation for the relevance of space charge measurements.

Nowadays there exist several space charge measurement methods which are able to estimate the space charge distribution across dielectric materials. One of the most common methods utilized is the Pulsed Electro-Acoustic (PEA). While the PEA method is widely used, its implementation and results interpretation require special attention and further improvement.

This thesis aims to contribute to the optimization of the PEA method by being able to make measurements from different test setups comparable and enhance the reliability of the results interpretation. This work is divided in two main parts with different scopes. In the first part, the work is focused utilizing flat samples, in which the effects of the different electrode materials at the dielectric interface and the use of reference samples for measurement characterization is analyzed. In the second part of this work, the focus is on measurements at HVDC cables for which the effects of different pulsed voltage injection configurations are tested, with a special focus in reduction of the crosstalk between the applied pulse and the acoustic sensor.

Flat samples with different electrode materials and configurations were investigated to analyze its influence in the calculation of the acoustic attenuation and dispersion parameters normally utilized during the post-processing stage of the PEA method. The experiments show that different electrode-dielectric interfaces between both electrodes used during a PEA measurement can potentially lead to erroneous calculations of the sample acoustic parameters during the post-processing.

The use of reference samples for characterization of PEA setups was analyzed utilizing multilayer samples with internal thin electrodes. By applying a voltage at the internal electrode, the existence of internal known charges at a localized position in the dielectric can be emulated and measured. The fact that the charge values are known at the internal and external electrodes, allow to use them for reference and calibration and calculation of post-processing parameters without the interference of the acoustic impedance mismatch at the external electrode interface.

For the analysis of the pulsed voltage injection in HVDC cables, a PEA test cell was developed for space charge measurements in full size HVDC cables. The PEA test cell was then utilized to perform space charge measurements on a HVDC cable for which several pulsed voltage injection configurations were analyzed and compared with respect to the reduction of the crosstalk between the pulsed voltage and the acoustic sensor. It was observed that the location of the pulsed voltage physical connection has a significant impact in the magnitude of the crosstalk, mainly attributed to the pulsed current distribution in combinations with the position of the acoustic sensor. It is also recommended to keep the PEA test cell isolated from ground and diminish as much as possible parasitic capacitances towards ground, as it has an impact in the generated crosstalk.

There can be situations in which, for special reasons or purposes, the PEA test cell must be grounded. For these cases, different impedances (using different exposed outer semiconductor distances) between the pulsed voltage injection electrodes were tested with positive results. At the same time the use of inductance impedance at the PEA test cell grounding can also reduce the magnitude of the crosstalk.

Testing of a developed coaxial injection for crosstalk reduction was performed, but the effect in the crosstalk magnitude was neglective, the behavior was similar to standard injection configurations.

The obtained results contribute to optimize the application of the PEA method for measurements of the space charge phenomena in HVDC components.

1. Introduction

1.1. HVAC vs HVDC

While AC technologies had been the standard for transmission and distribution during the past decades, with the continuous development of HVDC power converters, HVDC is increasing its presence in the transmission network, and in the future, it might step into the distribution network as well. There are many drivers for using HVDC systems in comparison with AC systems including:

- Asynchronous coupling capabilities and fast power flow control.
- HVDC lines allow for long transmission distances with low losses without compensation requirements.
- Higher transfer of power in HVDC cables with the same maximum electric field in the dielectric.
- DC cables do not require charging current during steady state conditions, negligible screen and sheath losses, and negligible dielectric losses.
- For long underground and submarine connections, the high value of the capacitive reactive power for AC cables makes the HVDC the only technically feasible solution.

Figure 1 shows a popular graph which depicts the break-even distance for the cost of DC systems in comparison with AC systems. For cable is typically in the range between 60 to 100 km.

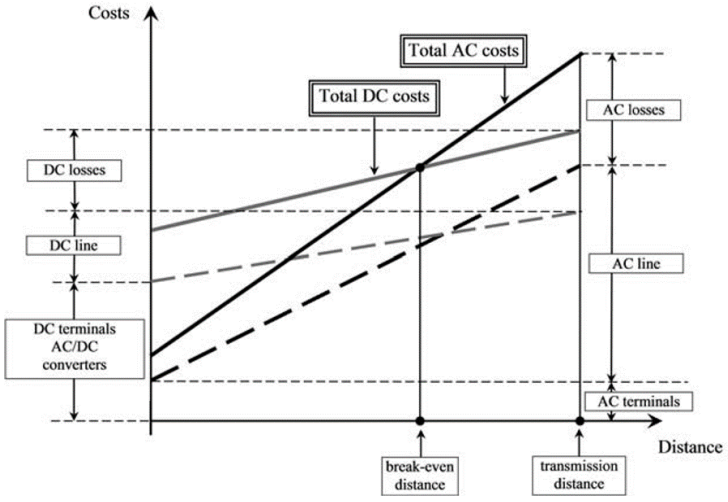

Figure 1. Qualitative plot comparing the costs of HVAC (black lines) and HVDC (gray lines) transmission systems. Dashed and solid lines represent, respectively, the costs without and with actualized energy losses. [1]

1.2. HVDC cables and Space Charge Phenomena

The transmission of electrical power can be accomplished through overhead transmission lines or underground cables. Overhead transmission lines play a dominating role in existing power systems, nevertheless cable systems use for power transmission have been increasing. This can be attributed to factors such as the maturity of the cable technology. In the other hand, the use of HVDC cable systems is considered environmentally friendly respective to their low visual impact and are widely more accepted in high-density populated regions. In the case of large water crossing energy transport, HVDC cable systems are the only economically and technically viable option.

Since the 1990s, extruded polymeric cables had been the main technology for HVAC cable systems. This is due to several advantages in comparison with mass-impregnated cables such as simpler and cheaper manufacture process [2,3], higher maximal working temperatures , easier maintenance and component mounting and replacement, no oil leakage, higher mechanical strength. In the case of HVDC cable systems, extruded polymeric cables usage has been relatively restricted due to premature breakdown problems attributed to space charge formation [4,5].

The reason space charges are not as relevant for AC systems, is the fact that the constant polarity change of the voltage (50 or 60 Hz) does not give enough time for the accumulation of charges in the bulk material. On the other hand, the mass-impregnated cables have higher conductivity compared to polymeric cables, resulting in less charge accumulation and shorter charge removal time constants. The formation of space charges is highly dependent on the physical and chemical structure of the dielectric [6,7].

The existence of space charges in the main insulation bulk, modify the electric field by creating local electric field enhancement at the insulation system [8,9] and influencing the electric behaviour of dielectric materials [10]. In [11], it was observed that the local enhancement due to space charges led to electrical treeing and, finally, failure. The authors of [12] used a thermoelectrical model to analyse the aging by space charge phenomena in dielectric materials. In [13], the role of space charges in multilayer epoxy commonly utilized in power electronics was studied. The authors of [14] analysed the aging that occurs during the de-trapping of space charges. Articles [15–17] present different aging and life models and their relationship with space charge phenomena. The effect of aging in space charge behaviour was analysed in [18] for epoxy and polyethylene, and for XLPE HVDC cable insulation in [19,20]. At [21] it was investigated the effect of additives in long term aging of XLPE in relation to space charges. Promising HVDC cable materials were the focus of [22]. Put briefly, space charge behaviour in solid dielectrics impacts upon the reliability of HVDC cable systems.

1.2.1. Space Charge Measurements

As mentioned before, space charge accumulation plays a vital role for solid dielectrics under DC electric fields. For this reason, several techniques have been developed for the measurement of space charges. For HVDC applications, the main measurement techniques are the acoustic and thermal methods; for literature reviews, see [23–27]. Even though a lot of research had been done for the improvement of these measuring methods, most efforts have been put into flat samples and mini cables. In late years, the effort for measurements in full size cables has increased as they can more accurately reproduce the conditions of the HVDC cables in the field. At the same time, it is desired to introduce space charge measurements as part of the qualification procedures for HVDC cables. To date there is a proposed protocol by the IEEE Std titled "IEEE Recommended Practice for Space Charge Measurements on High Voltage Direct-Current Extruded Cables for Rated Voltages up to 550 kV for space charge measure" [28] and the IEC-62758 "Calibration of space charge measuring equipment based on the pulsed electro-acoustic (PEA) measurement principle" [29].

Among the acoustic methods, the Pulsed Electro Acoustic Method has been utilized for the measurement of space charges in dielectric materials including flat samples, HVDC mini cables. Nevertheless, since the 1990s, successful space charge measurement had been performed in HVDC full size cables [30–32] and measurement of extruded HVDC cable qualification tests are being performed worldwide [33]. The practice of measuring space charges in full-size cables, instead of mini cables, has the advantages of assessing the manufacturing process of cables, and allowing the testing of relationships between a combination of variables that can only be achieved in full-size cables. This includes the combined variables of absolute temperatures and temperature gradients [34], and the relation of insulation thickness with trap distribution characteristics [35]. Still the PEA method requires further improvements to be accepted as the measurement protocol.

1.3. Scope of this Thesis

The PEA method faces some challenges such as the quality of the measured signal. The signal is influenced by several factors such as the parameters of the measuring test cell in combination with the test sample and the configuration and arrangement of the measurement setup including connections, parasitic capacitances and inductances, exposed semiconductor lengths and grounding, between others. This can create errors in the post processing and interpretation of the measured space charge values.

The research presented in this thesis aims to contribute to the optimization of the PEA method in order that measurements trough different setups can be comparable and enhance the

reliability of the results interpretation. For this purpose, the goal of this thesis is presented as two objectives.

First subobjective is the development of flat samples for reference, which can be used to calibrate and characterize acoustic space charge measurement methods. Second subobjective is to optimize the application of the pulsed voltage at the PEA method for measurements at full size HVDC cables to enhance the quality of the measured signal with focus in electromagnetic crosstalk.

To accomplish the above-mentioned objectives, the following five research questions were formulated:

1. What is the effect of different electrode materials for the acoustic calibration?
2. Can multilayer flat samples be utilized for the characterization and calibration of space charge measurement equipment?
3. Can the pulse injection configuration be optimized to reduce the electromagnetic interaction between the applied pulsed voltage and the piezo sensor in HVDC full size cables PEA measurements?
4. How can the electromagnetic crosstalk during pulse injection can be reduced when the PEA test cell requires to be grounded in full size HVDC cable measurements?
5. Can the utilization of a coaxial pulse injection have an impact between the pulsed voltage and piezo-sensor interaction?

1.4. Thesis Layout

Chapter 2 introduces the space charge phenomena in solid dielectrics. The main scenarios that lead to space charge generation are described from a macroscopic point of view. Afterwards, the PEA method principle is described, followed by the calculations required for the postprocessing of the measured signal.

In **Chapter 3,** a method to use premade samples for calibration and characterisation of equipment is presented. The method consists in the generation of known charge at multilayer samples applying external voltage. With the generation of the charges at thin electrodes built inside the dielectric samples, the spatial resolution of the system can be assessed. At the same time, these reference samples can be used to calculate the attenuation and dispersion factors of the travelling acoustic signals, without the possible misinterpretation caused by acoustic discontinuities.

Chapter 4 describes the main characteristics of the built PEA test cell for space charge measurements in full size cables including the reasoning behind the design and main factors to consider. Moreover, the characteristics of the utilized HVDC cable sample is also presented in this section. This PEA test cell and HVDC cable were then utilized for the experiments in Chapter 5

Chapter 5 starts with a description of the electromagnetic crosstalk between the applied pulsed voltage for the PEA method, and the piezo sensor, including its impact in the postprocessing of the measurements. From this, experimental analysis for the reduction of the crosstalk between the pulsed voltage and the acoustic sensor was performed. The first analyzed factors are the physical location of the pulse injection connection at the electrodes and the location of the grounding connection was performed. For the second experimental analysis, the analysis is performed for the specific case in which the PEA test cell is required to be grounded. For this case the influence of the exposed semiconductor between the injection electrodes, and the influence of adding a reactance to the PEA test cell grounding are considered. The chapter finalizes with the application of a coaxial connection for the application of the pulsed voltage, in which its influence with the electromagnetic crosstalk is compared with a non-coaxial application.

Chapter 6 presents the main conclusions of this work and answers the research questions.

2. Space Charges and PEA Method

Electrical charges that are present in the bulk of a dielectric are defined as space charges. This work focuses on the space charge in solid dielectrics. These charges can be formed either by irradiation by a beam of charged particles or by the existence of an electric field across an insulation under certain conditions. As previously mentioned, the existence of space charges in the dielectric bulk affects the electric field distribution which can affect the reliability and life expectancy of HVDC components.

In this chapter, a brief description of space charge formation from a macroscopic point of view is presented, followed by a description of the PEA method, the measurement method utilized in this thesis.

2.1. Space Charge Formation

Space charge formation in insulating materials is generated due to a current divergence at a localized region due to an inequality between the injection and extraction of charges. This accumulated charge has its associated electric field E_ρ, which contributes to the total electric field distribution across the dielectric [36].

$$\nabla \cdot \vec{j} = -\frac{\partial \rho}{\partial t} \tag{2.1}$$

$$\rho = \nabla \cdot \left(\varepsilon_o \varepsilon_r \vec{E}_\rho\right) \tag{2.2}$$

$$E_{total} = \vec{E}_{ext} + \vec{E}_\rho \tag{2.3}$$

where j is the current density, ρ is the charge density, t is the time, ε_0 is the vacuum permittivity, ε_r is the relative permittivity of the insulation, E_ρ is the electric field associated to a charge distribution, E_{ext} is the electric field induced by the applied voltage and E_{total} is the total electric field across the insulation. In Figure 2 we can see an example of the evolution in time of space charge formation across the insulation of a cable and the resultant local enhancement of the electric field.

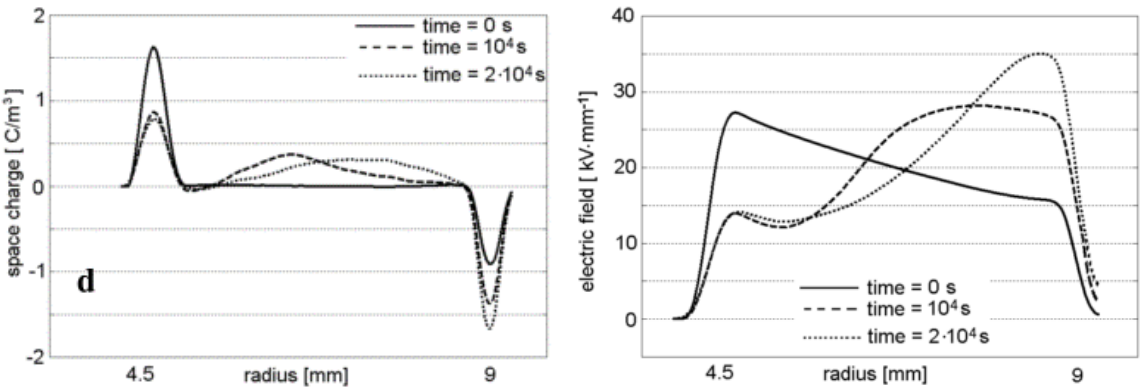

Figure 2. Space charge accumulation and the resultant electric field enhancement [36].

In a HVDC dielectric system, there are several scenarios which can lead to accumulation of space charges. From a macroscopical point of view, these are the existence of material interfaces such as dielectric-dielectric or dielectric–electrode interfaces, temperature gradient across the dielectric and structural inhomogeneities [37].

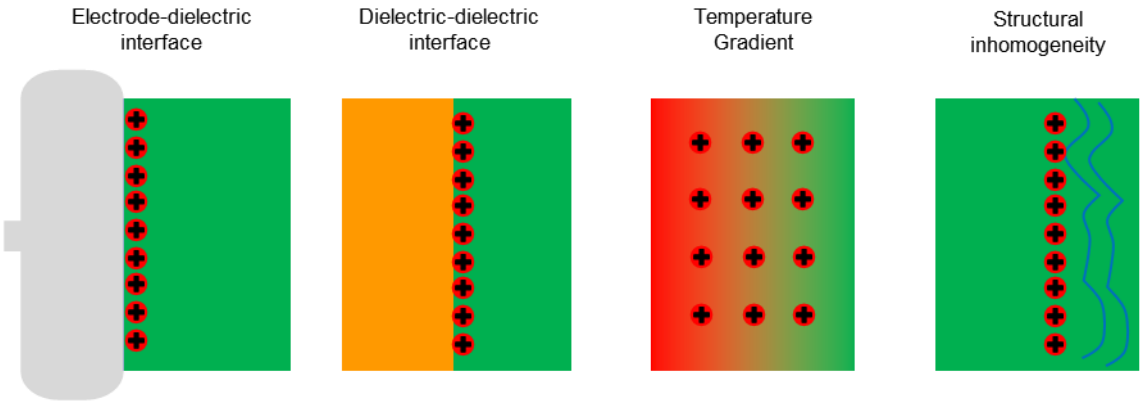

Figure 3. Different causes of charge accumulation.

Electrode-dielectric interface

For the electrode-dielectric case, the accumulation of charges is the result of the difference between the injected charges across the interface, and the conduction rate of the charges of the dielectric bulk. For the electrode dielectric interface, the flow of charges is dictated by the injection and extraction mechanisms. These mechanisms are dependent of the electric field and temperature together with interface conditions such as electrode and dielectric materials, surface defects and impurities. Meanwhile, the transportation of charges at the dielectric bulk are dictated by the conduction mechanisms which are also material, electric field, and temperature dependent.

There are three scenarios that might occur at the interface:

- The rate of charge injection/extraction is the same as the rate of charge conduction. In this case the accumulation of charges in the dielectric is zero, as there is no current divergence in the system.

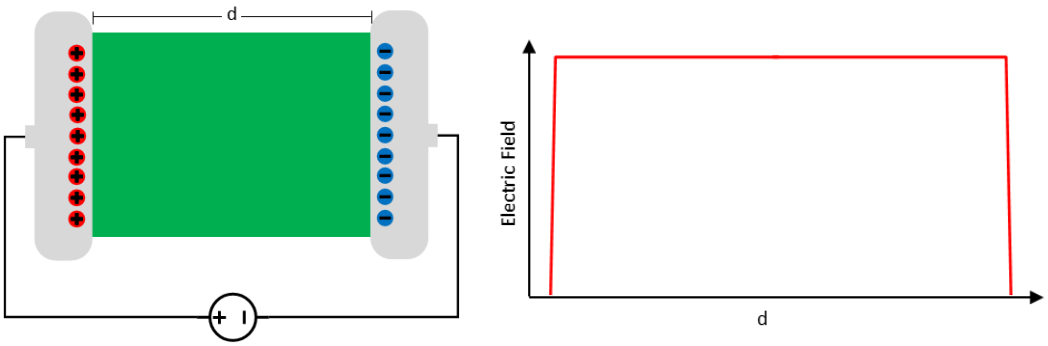

Figure 4. Electric field for a flat sample with no space charges accumulated.

- The rate of charge injection/extraction is higher than the rate of charge conduction at the interface. In this case, the mechanism of charge injection allows for a higher charge flow than the flow of charges across the dielectric. In this case, the current divergence will produce charge accumulation with the same polarity as the electrode, this is called homocharge formation. The existence of homocharges at the interface produce a local reduction of the electric field (transferring it to a different location in the dielectric) which results in a reduction of injected charges until the system reaches a steady state.

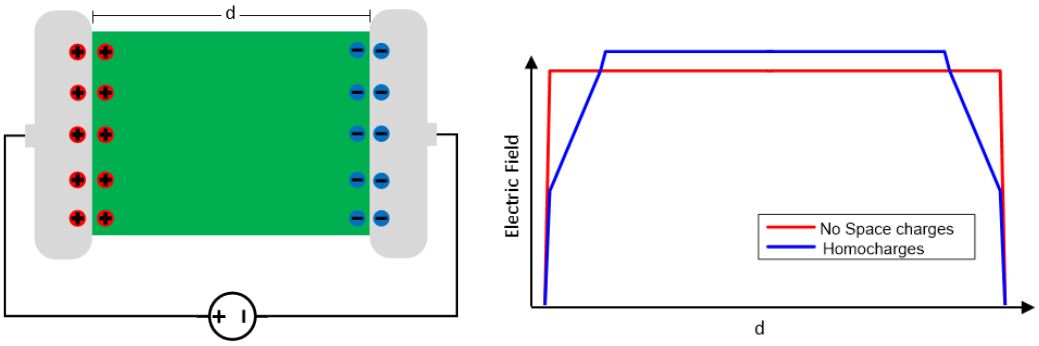

Figure 5. Electric field for a flat sample with homocharge accumulation.

- The rate of charge injection/extraction at the interface is lower than the charge conduction across the dielectric. In this case, the injection of charges is not high enough to compensate for the charges that are being depleted at the interface vicinity. This will result in local accumulation of charges with different polarity from the ones at the

electrode, known as heterocharges. The existence of heterocharges, leads to local enhancement of the electric field at the interface (reducing it at another location), which results in a local enhancement of charge injection at the electrodes until the system reaches a steady state.

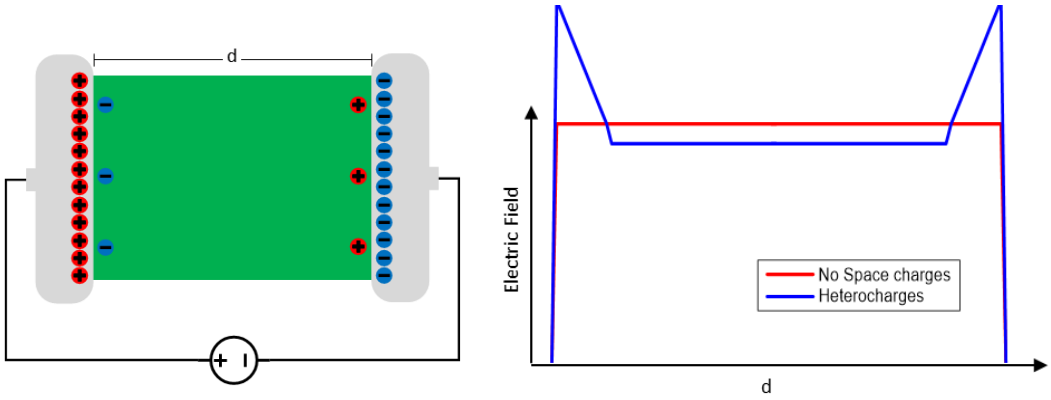

Figure 6. Electric field for a flat sample with heterocharge accumulation.

Dielectric-Dielectric interface

At this kind of interfaces, charges tend to accumulate at the interface due to the difference in the electrical properties of the materials. This configuration can be commonly found in HVDC cable accessories such as joints and terminations, where its charge behaviour requires special attention [38,39]. A common way to model the accumulation of charges at dielectric interfaces is the Maxwell-Wagner capacitor. It consists of a hypothetical 2 dielectric configuration as the one that can be seen in Figure 7.

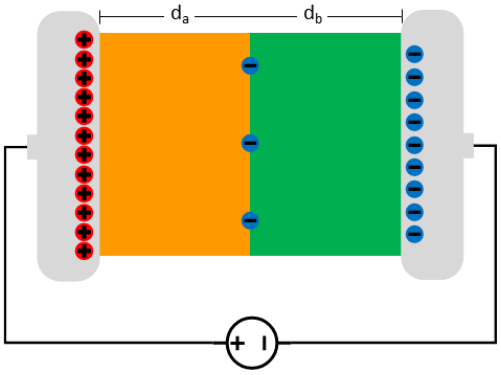

Figure 7. Space charge accumulation at a dielectric-dielectric interface of a flat sample.

The arrangement is two dielectrics connected in series between two electrodes. At the dielectric interface exists a step function for the electric properties of both dielectrics. The electrical contact between the dielectrics is considered ohmic. Using this configuration, we can

arrive to a mathematical expression for the time dependent surface charge $\kappa(t)$ when applying a DC voltage across the electrodes.

$$\kappa(t) = \frac{\sigma_b \varepsilon_a - \sigma_a \varepsilon_b}{\sigma_b \varepsilon_a + \sigma_a \varepsilon_b} U_0 \left(1 - e^{-\frac{t}{\tau}}\right) \tag{2.4}$$

where ε is the material constant, σ is the conductivity, U_0 is the applied DC voltage and τ is the time constant which can be calculated using:

$$\tau = \frac{d_a \varepsilon_b + d_b \varepsilon_a}{d_b \sigma_a + d_a \sigma_b} \tag{2.5}$$

It must be taken into account that the conductivity is highly dependent on the electric field, which is influenced by the accumulation of space charges, meaning that in order to solve equation (2.5) with electric field dependent conductivity, numerical procedures are required.

This ideal model has some limitations for practical cases [40]. In real materials, the dielectric surface does not have the same electric properties as the bulk materials due to exposure or manufacture process. Another factor is that the interface is not mechanically perfect. The rugosity of materials may produce air pockets (or the existence of other materials such as lubricants) which change the electrical properties of the interface. In [28, 50, 51] is shown that interface charge exists at the interface of two identical dielectrics due to these factors.

The main cause is the rate injection and extraction of charges against the bulk transport of charges, as well as the inhomogeneity of the material. There are different mechanisms responsible for the conduction of charges in a dielectric. Some of these mechanisms are responsible for the charge injection and extraction at the material interfaces, while others dictate the charge conduction across the dielectric.

Temperature gradient

The existence of temperature gradient in dielectric materials produces accumulation of space charges across the insulation bulk. This is because the conductivity is highly dependent of the temperature, creating a conductivity gradient across the material. At the same time, the permittivity of the material changes because of the thermal expansion, this reduces the number of polarisable molecules per unit volume. Both changes in conductivity and permittivity affect the ε/σ ratio resulting in the accumulation of charges.

$$\rho = j \cdot \nabla \left(\frac{\varepsilon}{\sigma}\right) \tag{2.6}$$

This temperature gradient can exist in systems such as HVDC cables. The accumulation of charges by temperature gradient distorts the Laplacian electric field and produces field inversion, where the electric field is higher (lower temperature) at the external electrode and lower (higher temperature) at inner conductor.

Structural inhomogeneity

The polyethylene materials consist of an arrangement of long molecular chains. It is formed by the combination of parallel chains (crystalline region) and by arbitrary arrangement of chains (amorphous regions). Each region has different conductivity which leads to accumulation of charges at their boundaries. The existence of fillers also accumulates charges due to their interface with the host material, having each one their own conductivity and permittivity.

2.2. PEA Measuring Method

Since more than 40 years, several non-destructive methods (in the case of HVDC cables, the outer semiconductor needs to be exposed in which the term "non-destructive" is not completely accurate) have been introduced for the measurement of space charges [23,24,36,41]. These methods follow the same principle: The charges are excited by an external transient, whose response can then be either electrically or mechanically measured. The methods can be classified in three main families which include: First, the methods that use thermal diffusion. Second, the methods that utilize an elastic wave propagation. And the third family are the methods which use an electrical stress, to which the PEA belongs.

The focus of this work is the PEA method, whose functioning principle is described in the next section.

2.2.1. PEA Method Principle

In a dielectric under an electric field, the force for a unit volume can be described by [42]:

$$f = \rho E - \frac{1}{2}E^2\nabla\varepsilon - \frac{1}{2}\nabla(E^2 a) + \Pi\nabla E \tag{2.7}$$

where f is the electrostatic force density, ρ is the charge density, E is the electric field, ε is the permittivity of the material, a is the electrostrictive coefficient ($a \approx -\varepsilon/2$ for most materials) [43] and Π is the permanent dipole density.

The PEA method consists of applying a voltage pulse across a test object, which can be superimposed with an applied Direct Current (DC) voltage. In this case the total applied electric field becomes:

$$E = E_{DC} + e_p \tag{2.8}$$

E_{DC} representing the electric field from the DC source and e_p the electric field from the voltage pulse. The application of the pulsed voltage will disrupt the electrostatic and elastic force balance, where the transient of the force unbalance creates acoustic waves at the charge locations (and at permittivity discontinuity regions such as in samples with different dielectric layers) which propagate across the materials.

The propagating acoustic waves can then be measured by an acoustic transducer at one of the electrodes as shown in Figure 8.

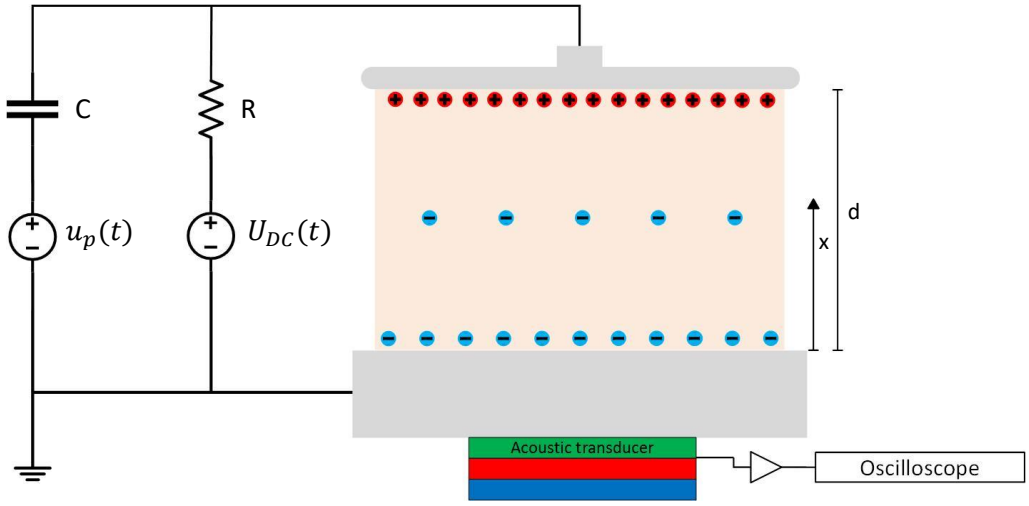

Figure 8. Schematic configuration of space charge measurements using PEA method for flat samples.

Figure 8 represents a PEA configuration for flat samples. In the figure, the voltage pulse generator is represented by $u_p(t)$ from which the pulse propagates across the decoupling capacitor to the sample. The decoupling capacitor "C" decouples the pulse source from the HVDC generated at U_{DC}. The resistance "R" gives a high impedance path to the pulse, so it does not reach the HVDC source, at the same time reduces the short circuit current in case of dielectric failure at the sample. The application of $u_p(t)$ across the sample creates a pressure force in the charge locations which propagate across the sample arrangement. Part of these acoustic propagating waves will reach an acoustic transducer installed at one of the electrodes, which generates an electric signal from the acoustic waves. The sensor, which is most of the time a piezo film, is terminated by a backing material that acoustically matches the sensor to avoid acoustic reflections during the measurement.

PEA measurements for cable sample geometries follow the same principle as for flat samples, and they are treated in more detail at Section 4 and 5.

2.2.2. PEA Post-Processing

During measurements, the signal measured at the scope does not directly represent the space charges across the material. The measured signal needs to be calibrated and mathematically processed. This is to correct the distortions caused by the sensor amplifiers circuit response, the geometric divergence (in case of coaxial samples) and the acoustic attenuation-dispersion across the material and the effect of the acoustic generation. At the same time, other factors such as reflection, and transmission of the acoustic wave across the different materials needs to be considered for the design of the PEA test setup and the interpretation of results.

2.2.2.1. Sensor-Amplifier Response

In the PEA method, the combination of the transducer and amplifiers has a specific response H, in which the expected measured signal is distorted, mainly because of its high-pass filter behaviour. To recover the deconvoluted voltage signal $V_d(t)$ from the measured output signal $V_{meas}(t)$ a deconvolution procedure [44–46] can be performed following that:

$$V_{meas}(t) = F^{-1}[H(\omega)V_d(\omega)] \tag{2.9}$$

$$V_d(t) = F^{-1}\left[\frac{V_{meas}(\omega)}{H(\omega)}\right] \tag{2.10}$$

where F^{-1} is the inverse Fourier transformation.

To calculate $H(\omega)$, it is required to have known values for $V_{meas}(\omega)$ and $V_d(\omega)$. This requires utilizing a measured signal in which the space distribution is known and with special care of the signal processing requirements. A space charge distribution that can accurately be predicted in samples with applied DC voltage when there are no space charges in the dielectric bulk (in [47] it is described how to obtain an equivalent free charge sample measurement from a sample with pre-existing space charges at the dielectric). In this case, the first measured voltage peak belonging to the charges from the closest electrode towards the acoustic sensor named as $V_{e1}(t)$ (because the pressure wave originating from this electrode has not suffered from acoustic attenuation and dispersion in the sample). The considered waveform for the deconvoluted signal of $V_{e1}(t)$, is named $K_d(t)$ which consist of a pulse whose magnitude is one and its width is equal

to the pulsed voltage duration (the electrode charges are in a very thin surface for which the pressure wave follows the pulsed voltage). From where we can get:

$$H(f) = \frac{V_{meas}(\omega)}{V_d(\omega)} = \frac{V_{e1}(\omega)}{K_d(\omega)} \tag{2.11}$$

2.2.2.2. Geometric Divergence Factor

In coaxial geometries, it is required to correct the measured signal due to the divergence at the applied electric field $e_p(r)$ from the pulsed voltage across the sample radius r:

$$e_p(r) = \frac{u_p}{r ln\left({}^{r_{out}}/_{r_{in}}\right)} \tag{2.12}$$

The correction factor $K_p$can be defined as:

$$K_p = \frac{e_p(r_{out})}{e_p(r)} = \frac{r}{r_{out}} \tag{2.13}$$

At the same time, it can be considered for HV cables that the r_{in} is big enough in relation with the thickness of the dielectric. In this case, the acoustic waves magnitude reduces with the square root of the radius as they propagate towards the acoustic sensor .

$$K_g = \sqrt{\frac{r_{out}}{r}} \tag{2.14}$$

From where the total geometric divergence correction factor K_{div} is the combination of K_p and K_g:

$$K_{div}(r) = K_p(r)K_g(r) = \sqrt{\frac{r}{r_{out}}} = \frac{V_{meas}(vt)}{V_{meas}(vt)} \tag{2.15}$$

where v stands for the average value of acoustic propagation speed in the sample material.

2.2.2.3. Acoustic Attenuation and Dispersion

As previously mentioned, in the PEA method, the measured space charge signal is obtained from acoustic waves generated due to their interaction with a transient electric field. These acoustic waves require to travel across different materials before they reach the acoustic transducer. The dielectric sample materials generally consist of lossy materials which attenuate and disperses the pressure waveform as it propagates.

The expression for a planar acoustic wave $p(x,t)$ traveling through a lossy medium can be represented as [36,48,49]:

$$p(x,t) = F^{-1}\left[P(0,\omega)e^{-\alpha(\omega)x}e^{-i\beta(\omega)x}\right] \tag{2.16}$$

$$G(x,\omega) = e^{-\alpha(\omega)x}e^{-i\beta(\omega)x} \tag{2.17}$$

where $P(0,\omega)$ is the is magnitude of the pressure wave component at the location $x = 0$ (before losses), $\alpha(\omega)$ is the frequency dependent attenuation factor which takes into account the decrease of the wave magnitude while it travels through the medium, $\beta(\omega)$ is the frequency dependent phase factor, which is the dispersion and takes into account that the acoustic speed is frequency dependent.

To recover the original acoustic signals before losses, it is required to know the $G(x,\omega)$ of the material. The function $G(x,\omega)$ can be obtained by utilizing two acoustic waveforms from two different locations which should be equal in a non-lossy medium. Commonly, the utilized signals are the one belonging to the measuring electrode $p(0,t)$ and HV electrode $p(d,t)$ in a measurement with no space charge in the dielectric bulk (for coaxial geometries, the geometric divergence needs to be considered. From here we get that:

$$G(d,\omega) = \frac{F[p(d,t)]}{F[p(0,t)]} = e^{-\alpha(\omega)d}e^{-i\beta(\omega)d} \tag{2.18}$$

where F is the Fourier transform. From here we can obtain $\alpha(\omega)$ and $\beta(\omega)$ as follows:

$$\alpha(\omega) = -\frac{1}{d}ln|G(d,\omega)| \tag{2.19}$$

$$\beta(\omega) = -\frac{1}{d}angle(G(d,\omega)) \tag{2.20}$$

With $G(x,\omega)$ we can recover an equivalent measured voltage from the acoustic waves generated by the distribution of space charges (before propagation losses) by:

$$V_{sc}(x,t) = F^{-1}\left[\frac{V_d(x,\omega)}{G(x,\omega)}\right] \tag{2.21}$$

With the relation of measurement time with sample position $t = {}^{x}/_{v}$, where v is the average value of acoustic propagation speed in the sample material; we can utilize $V_{sc}(x,t)$ as $V_{sc}(x)$.

2.2.2.4. Calibration Factor

To convert the acquired measured voltage signal into space charge density, it is used a calibration factor K_{cal}. This factor is normally calculated using the known charge value at the electrode with the acoustic transducer. As in previous sections, this is true for samples with known applied voltage and no space charges in the dielectric bulk, where the surface charges in the measurement electrode is:

$$\sigma_{e1} = \frac{V_{DC}\varepsilon_0\varepsilon_s}{d} \tag{2.22}$$

for planar samples and

$$\sigma_{e1} = \frac{V_{DC}\varepsilon_0\varepsilon_s}{r_{out} ln {}^{r_{out}}/_{r_{in}}} \tag{2.23}$$

for coaxial samples.

From where K_{cal} can be calculated with:

$$K_{cal} = \frac{\int_{x_1}^{x_2} V_{sc}(x)dx}{\sigma_{e1}} \tag{2.24}$$

2.3. Chapter Summary

In this chapter, space charge formation from a macroscopic point of view was presented. Afterwards, a description of the working principle for the space charge measurements using the PEA method was presented, followed by its most common procedure method for the postprocessing of the measured signal.

3. Thin Electrode Flat Samples for reference and calibration of Acoustic Space Charge Measurements

3.1. Introduction

Due to the acoustic distortion and the transducer-amplifier response, the PEA method require mathematical post-processing to obtain accurate quantitative values [50–54]. The post-processing involves deconvolution methods whose calibration is obtained by measurement of known surface charge values at the electrodes when a known voltage is applied at a space charge free sample. Following this procedure, the existence of acoustic discontinuities for the generation and the propagation of the acoustic signals at the dielectric electrode interfaces are not fully taken into account, which can create misinterpretations, resulting in inaccuracy and errors [55–57].

This chapter covers the use of solid flat dielectric samples with known charge values controlled by an external voltage source that can be used for calibration and equipment characterization.

In Section 3.2 the influence of different electrode materials at the calculation of the attenuation factors is shown by means of experimental tests.

In Section 3.3, the validity of using multilayer-samples to emulate known values of space charges in the dielectric is demonstrated with the use of the pulse-electroacoustic (PEA) method. In [58], corona charged samples were used for calibration and equipment characterization but it was concluded that the method is not suitable for calibration purposes because of inconsistency in the samples. In [59,60] a method is presented in which solid dielectric samples with known charge values controlled by an external voltage source, can be used for calibration and equipment characterization, a similar approach is proposed and extended in this work.

This Chapter is based on:

Mier-Escurra, G.A.; Rodrigo-Mor, A. Influence of Electrode Material in Acoustic Attenuation Factors Calculation in Space Charge Measurements. ICEMPE 2019 - 2nd Int. Conf. Electr. Mater. Power Equipment, Proc. 2019, 166–169, doi:10.1109/ICEMPE.2019.8727373.

Mier Escurra, G.; Rodrigo Mor, A.; Vaessen, P. A Calibration Method for Acoustic Space Charge Measurements Using Multilayer Samples. Sensors 2018, 18, 2508, doi:10.3390/s18082508.

Section 3.4 summarizes the conclusions of this chapter.

As mentioned in the previous chapter, the common calibration procedure involves the calculation of a transfer function using deconvolution processes. For the PEA method, deconvolutions are a common practice in the post-processing of the measurements. Using a space charge free sample with a known voltage, deconvolutions are performed using the actual measured signal and the expected calculated signal before electric and acoustic distortions. From this process, errors may arise, as the transfer function is calculated by comparing the pressure waves generated at the external electrodes, where the top electrode may have a different impedance mismatch than the signal coming from charges at the dielectric bulk. Equations (3.1)–(3.3) represent the pressure waves generated at the bottom electrode, top electrode, and the insulation bulk respectively, after traveling through the sample and transmitted to the bottom electrode:

$$\tilde{p}_{bot}{}'(t_0) = G_{bot}\tilde{p}_{bot}(t) \tag{3.1}$$

$$\tilde{p}_{top}{}'\left(t_0 + {}^{d}/_{v}\right) = G_{top}T_{s-bot}k_g(d)F^{-1}[P(d,\omega)G(d,\omega)] \tag{3.2}$$

$$\tilde{p}_{s}{}'(t_0 + {}^{x}/_{v}) = G_{s}T_{s-bot}k_g(x)F^{-1}[P(x,\omega)G(x,\omega)] \tag{3.3}$$

$$P(d,\omega) = F[\tilde{p}_{top}(t_0)] \tag{3.4}$$

$$P(x,\omega) = F[\tilde{p}_{s}(t_0)] \tag{3.5}$$

$$G(x,\omega) = e^{-\alpha(\omega)x}e^{-i\beta(\omega)x} \tag{3.6}$$

where $\tilde{p}_{bot}(t)$, $\tilde{p}_{top}(t)$ and $\tilde{p}_{s}(t)$ are the transient pressure waves [Pa] generated at the bottom electrode, top electrode and inside the sample respectively; while $\tilde{p}_{bot}{}'$, $\tilde{p}_{top}{}'$ and $\tilde{p}_{s}{}'$ represent the pressure waves after they propagated to the bottom electrode (refer to Figure 9 for electrode naming). F represents the Fourier transform, $k_g(x)$ is the geometric factor (in case of flat samples it can be considered equal to one). The factor $\alpha(\omega)$ is the frequency dependent attenuation [neper/m] and takes into account the decrease of the wave magnitude while it travels through the medium. The factor $\beta(\omega)$ is the frequency dependent phase factor [1/m], which is the dispersion and takes into account that the speed of sound is frequency dependent [49]. The t_0, d and v represent the time of the applied pulsed voltage [s], the sample thickness [m] and the average value of propagation speed [m/s] of the acoustic wave across the sample for spatial location purposes. G_{bot}, G_{top} and G_s are the generation coefficients at the bottom and top electrode interface and at the insulation bulk respectively; as the generated pressure waves are divided and travel in two directions, but only the wave traveling towards the electrode with the transducer (bot electrode) is detected. T_{s-bot} is the

transmission coefficient at the bottom electrode due to the acoustic impedance mismatch. The generation and transmission coefficients can be calculated as [61,62]:

$$G_{bot} = \frac{Z_{bot}}{Z_s + Z_{bot}} \tag{3.7}$$

$$G_{top} = \frac{Z_s}{Z_{top} + Z_s} \tag{3.8}$$

$$G_s = \frac{Z_s}{Z_s + Z_s} \tag{3.9}$$

$$T_{s-bot} = \frac{2Z_{bot}}{Z_s + Z_{bot}} \tag{3.10}$$

Z_{top}, Z_s and Z_{bot} represents the acoustic impedances [kg·m^{-2}·s^{-1}] of the top electrode, the insulation bulk, and the bottom electrode, respectively.

As can be seen in equations (3.7)–(3.9), the fraction of the traveling pressure waves towards the sensor are different if they are generated at the bot electrode, at the insulation bulk or the top electrode, ($G_{bot} \neq G_{top} \neq G_s$). This pressure waves are then affected by the transfer coefficient at the interface, compensating for the waves generated at the sample but not for the top electrode. Because the transfer function is commonly calculated using the external electrode signals, this might result in a deviation to the measured signals originated at the insulation bulk. The configuration of the electrodes in a normal PEA setup for flat samples is represented in Figure 9.

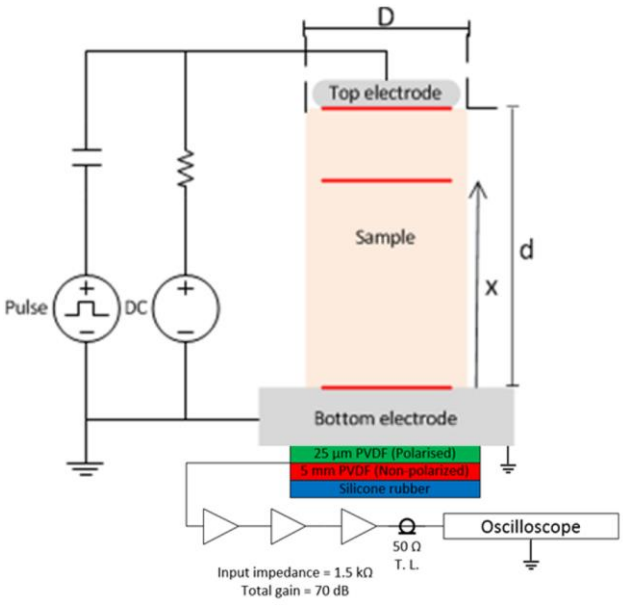

Figure 9. Schematic representation of a PEA measurement for a flat sample. The sample diameter is several times bigger than the height (D >> d), but the scale is modified for representation purposes.

3.2.Influence of Electrode Material in Acoustic Attenuation Factors

PEA tests in flat samples were performed to analyse how the electrode materials affect the calibration for acoustic losses. The comparison was performed by measuring same material sample, utilizing different top electrode (the electrode father away from the acoustic sensor) materials and configurations, to which then the corresponding transfer function for the acoustic losses were calculated.

3.2.1. PEA test cell

The common arrangement for a PEA method was used where an equivalent circuit of the setup is shown in Figure 9. The pulse is generated by the switching of a pulse generator switch (HTS 80-12-UF, Behlke). The used oscilloscope is a Waverunner 44 Xi-A 400 MHz (Lecroy). The acoustic sensor consists of a 25 µm film of polarized polyvinylidene fluoride (PVDF) with an area of 20 mm x 6 mm and relative permittivity of ε_0= 11, backed by 5 mm of non-polarized PVDF. The PVDF piezo film is connected to a charge amplifier with 1.6 kΩ input impedance and 30 dB gain (giving an RC time constant of RC = 748 kHz), in series with two 20 dB amplifiers for a total of 70 dB. The amplified voltage signal reaches the oscilloscope through a 50 Ω transmission line.

3.2.2. Sample Preparation

The material used for the flat samples is a two-part (resin and hardener) epoxy resin. The epoxy has a resistivity of 10^{14} ohm·cm and a relative permittivity of 4. Two HV electrode configurations were used with an internal electrode and with an external electrode. For the flat samples with an internal HV electrode, a gold plating of approximately 30 nm was deposited in the top surface of the first layer of epoxy, before the second layer of epoxy was cast on top of it. For the external HV electrodes, a single layer epoxy was used with different electrode materials. The external electrodes used were aluminium electrode, semiconductor electrode (commonly used for PEA measurements), and a 0.06 mm aluminium electrode layer of aluminum backed with a layer of 1 mm thick epoxy. The last-mentioned electrode is to observe the influence in the thickness of the electrode when is not thin enough for all the waveform frequency components to be considered negligible. Table 1 shows the acronyms of the different electrode configurations used in this work. The electrodes ES, EA and EAE share the same diameter and are used at sample 2. In the case of EA and EAE, silicon oil was used to improve the acoustic contact.

Table 1. Electrode Configuration Acronyms. © 2019 IEEE

Electrode Configuration	Acronym
30 nm gold plating at sample 1	EGET (Epoxy Gold Epoxy Thick)
30 nm gold plating at sample 2	EGES (Epoxy Gold Epoxy Small)
Semiconductor electrode	ES (Epoxy Semiconductor)
Aluminium electrode	EA (Epoxy Aluminium)
0.06 mm aluminium epoxy backed	EAE (Epoxy Aluminium Epoxy)

Table 2 shows the geometry of the different samples used for the experiments. Sample 1 and 3 have internal electrodes while sample 2 used external electrodes.

Table 2. Geometric Properties of Samples. © 2019 IEEE

Sample	Diameter		Thickness	HV electrode type
	Epoxy	HV Electrode	Ground to HV electrode	
Sample 1	56 mm	36.7 mm	3.3 ± 0.06 mm	EGET
Sample 2	56 mm	36 mm	3.25 ± 0.06 mm	ES EA EAE
Sample 3	56 mm	36.7 mm	1.27 ± 0.06 mm	EGES

3.2.3. Measurement Procedure for influence of electrode material comparison

The HVDC and voltage pulse were applied to the HV electrode described at Table 2. The measurement process was the following: Sample 1 and 2 from Table 2 were subjected to 10 kV to produce surface charges of equal and opposite polarity at each electrode. With the PEA, these equal charges produce acoustic propagating waves that reach the acoustic sensor (piezo-transducer), located at the ground electrode, where the measured signal differs from the generated one due to the acoustic losses [63]. By Performing deconvolution between the propagating waves of the HV and ground electrode in a space charge free sample, it is possible to extract the frequency-dependent attenuation factor and phase factor for the transfer function $G(\omega, x)$ following the procedure described at Section 2.2.2.3.

Because the magnitude of the propagating waves is influenced by the materials at the interface of the electrodes, the deconvolution of these two signals may not match to the transfer function for pressure waves that are generated in the dielectric bulk, creating deviations in the calibration.

Sample 3 was used to analyze and compare the deviation of the calculated transfer functions of Samples 1 and 2 when applied to compensate its attenuation. A voltage of 5 kV was applied to its internal HV electrode to produce surface charges of equal magnitude but opposite polarity as in Sample 1 and 2. In this case, the configuration of a 30 nm thickness gold

plating electrode between layers of the epoxy, is considered to resemble the situation of a pressure wave generated directly at the insulation bulk. Afterwards, the $G(\omega, x)$ calculated with each configuration of Sample 1 and 2 was applied to Sample 3 to restore the signal coming from the HV electrode and the results were compared.

3.2.4. Influence of electrode material comparison

To keep the accumulation of charges at a minimum and just measure surface charges at the electrodes, the duration of the measurements was less than 15 seconds. In Figure 10 can be observed the measured values of the PEA Method for different electrode configurations. The magnitudes are normalized for easier comparison. The difference in magnitude of the arriving signal at the HV electrode can be directly observed from the figure, this is due to the different acoustic properties of the materials at the interface. The expected acoustic impedances for the different materials are presented in Table 3.

Table 3. Acoustic properties, electrode acoustic influence comparison. © 2019 IEEE

Material	Acoustic impedance [kg·m-2·s-1]
Aluminium	$17.3 \cdot 10^6$
Epoxy	$4.9 \cdot 10^6$
Semiconductor	$\approx 2.5 \cdot 10^6$ (Pressure dependent)

These results match what is expected due to the acoustic divergence. For the EA case, the higher acoustic impedance of the aluminum against the epoxy produces that most of the generated pressure wave propagates towards the aluminium, and a smaller pressure wave propagates across the dielectric towards the piezo transducer, which results in a barely visible signal. In the case of the ES, the opposite happens, where a higher magnitude pressure wave propagates through the dielectric in comparison to the semiconductor. For the EGET case, the electrode mechanical properties are considered negligible due to the thickness in comparison to the wavelength of the wave components so the fraction of the generated pressure wave reaching the sensor is considered to be 0.5 (as would be the case in pressure waves generated at the dielectric bulk). The EAE electrode thickness is not thin enough to be considered negligible, creating a behaviour which seems somewhere between the EGET and ES electrodes.

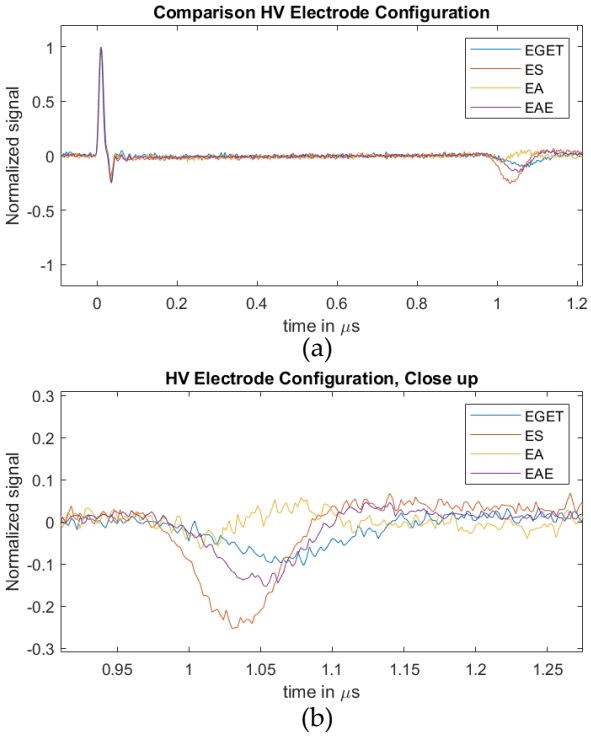

Figure 10. Normalized PEA measurement Samples 1 and 2 at 10 kV: (a) Full signal, (b) Close up at the HV electrode.

The procedure used to compute $G(\omega, x)$ can be found in [63] and is described in Section 2.2.2.3. The computation was limited to the frequency components of 0 to 12.5 MHz. This is because the signal to noise ratio at higher frequencies due to attenuation, does not allow to use the full bandwidth.

In Figure 11 we can observe the transfer function components extracted from the PEA measurements at Sample 1 and 2, were the difference in the transfer function between the different configurations is clearly visible. In the EA case, the attenuation factor α, does have a high value for low frequencies as it is expected but on the other side, at higher frequencies α does not significantly increase as it is common in lossy materials. This is attributed to the low signal to noise ratio of the EA at the HV electrode which precludes its proper calculation of $G(\omega, x)$ at high frequencies. Note that, although the trends are clearly visible, even when acoustic impedance mismatch is taken into account the calculated attenuation and dispersion factors have errors. In reality the materials should not attenuate at 0 Hz, which for none of the calculated cases is obtained, not even for the EGET in which there should not be acoustic impedance mismatch. This can be attributed to small errors introduced due to the bandwidth of the piezo-amplifier al low frequencies.

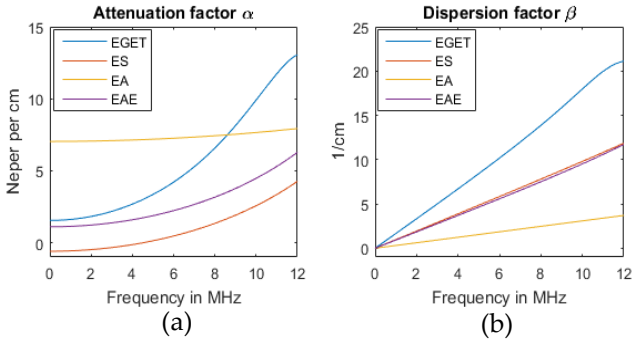

Figure 11. Transfer function components for each electrode configuration at Sample 1 and 2. (a) Attenuation factor α, (b) Dispersion factor β. © 2019 IEEE

The calculated transfer functions were used to correct the attenuated signal from the sample 3 with the EGES electrode. In Figure 12 we can appreciate the results for each case, where the EGES before attenuation and dispersion correction is compared with the EGES signal after its correction utilizing the different transfer function components from Figure 11. For the results on the graph, a low-pass filter with a cut-off frequency of 12.5 MHz was applied. The filter is necessary for a quantitative comparison between the electrodes, as the loss of information at the higher frequencies due to the attenuations does not allow for signal recovery for the same bandwidth of the unfiltered ground electrode signal.

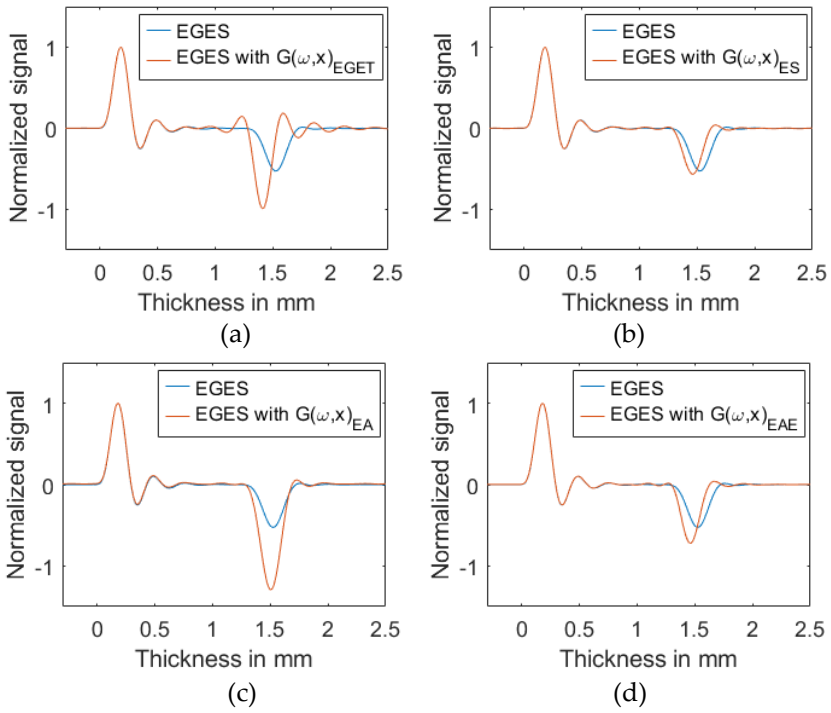

Figure 12 EGES measured signals, before and after applying $G(\omega, x)$. The signals have a low-pass filter of 12.5 MHz. © 2019 IEEE

From Figure 12 we can observe that using $G(\omega, x)_{EA}$, the amplification of the HV electrode results in a higher peak than the ground electrode. This is expected due to the low fraction of energy that propagates towards the sensor at an epoxy-aluminum interface, resulting in a higher calculated attenuation factor. At the same time, using $G(\omega, x)_{ESem}$ we observe a minimum change. This can be attributed to the fact that the epoxy-semiconductor interface generates a bigger signal propagating towards the sensor than a generated signal at the dielectric bulk, both suffering attenuation during propagation. Nevertheless, the attenuation is higher at high frequencies and in this case because the used bandwidth was limited to 12.5 MHz, we cannot appreciate the effect. On the other side, using $G(\omega, x)_{EGET}$ the HV electrode was able to almost fully recover the signal to a value similar to the ground electrode magnitude. Some oscillations can be appreciated because the bandwidth for this transfer function loses accuracy below the cut-off frequency of the filter due to low signal to noise ratio. As can be appreciated, applying attenuation and dispersion correction without correct consideration of electrode materials will lead to incorrect results, because the effect of the impedance mismatch and acoustic properties of the dielectric material will be mixed. In [64] is presented a method for the consideration of the top electrode acoustic mismatch in the postprocessing.

3.2.5. Acoustic Attenuation and Dispersion Coefficients Calculation

Considering that the electrode arrangement of gold plating inside the dielectric can emulate the conditions of a pressure wave generated at the dielectric bulk, the acoustic waveforms generated at the dielectric and the electrodes before attenuation and distortion can be recovered. This can be done avoiding the dielectric-electrode interface by using a reference sample with a thin electrode built between dielectric layers (as the ones used in this work) to obtain $G(\omega, x)$ as was done in Figure 12 EGES measured signals, before and after applying $\mathbf{G}(\boldsymbol{\omega}, \mathbf{x})$. The signals have a low-pass filter of 12.5 MHz. The reference sample should be the same dielectric material as the sample of interest. Equation (3.11) can be used to obtain the full acoustic signal in a PEA measurement for a sample of interest.

$$p(x) = F^{-1}[P_x(\omega, x_s)] + F^{-1}[P_d(\omega, d)] \tag{3.11}$$

$$P_x(\omega, x) = P(\omega, x_s)G_1(\omega, x_s) \tag{3.12}$$

$$P_d(\omega, d) = P(\omega, d)G_2(\omega, d) \tag{3.13}$$

where $p(x)$ is the processed signal for acoustic losses across the whole sample thickness x, including the electrodes at 0 and d. $P(\omega, x)$ is the Fast-Fourier Transform of the generated pressure wave propagating towards the sensor. x_s is the dielectric thickness, $0 < x_s < d$. $G_1(\omega, x_s)$ is the transfer function calculated from a prebuilt sample. $G_2(\omega, d)$ is the transfer

function calculated using the common procedure by comparing the ground and HV electrode signal of the main sample.

3.3.Use of multilayer samples for calibration

As previously mentioned, the use of multilayer samples with known charge values can be utilized for calibration and characterization of space charge measurement equipment. The multilayer sample method consists in using a fixed voltage at thin electrodes in the different layer interfaces to generate known values of charges, and subsequently measure them as space charges using the acoustic methods for calibration purposes. This is performed using samples built of a stack of dielectric layers with a nanometric thickness electrode at the dielectric-dielectric interfaces to form a single sample.

By having control of the geometry and material of the layers, the capacitances between the electrodes are known. The relation between capacitances, voltages, and charges at each electrode is represented in the following equation:

$$\begin{pmatrix} Q_1 \\ Q_2 \\ \vdots \\ Q_N \end{pmatrix} = \underbrace{\begin{bmatrix} \sum_{i=1}^{N} C_{1i} & -C_{12} & \cdots & -C_{1N} \\ -C_{21} & \sum_{i=1}^{N} C_{2i} & \cdots & -C_{2N} \\ \vdots & \vdots & \ddots & \vdots \\ -C_{N1} & -C_{N2} & \cdots & \sum_{i=1}^{N} C_{Ni} \end{bmatrix}}_{\text{Maxwell capacitance matrix}} \begin{pmatrix} U_1 \\ U_2 \\ \vdots \\ U_N \end{pmatrix} \tag{3.14}$$

where the elements of the Maxwell capacitance matrix can be calculated utilizing the mutual capacitances between electrodes as shown in Figure 13. Q and U represent the charge and voltage respectively, at each of the electrodes of the calibration sample.

An example of a two layers sample and its electrodes are represented in Figure 13. In the figure, the outer circle represents a grounded spherical shell with an infinite radius. Even though the spherical shell at infinity and the lower electrode (represented as “electrode 1” in Figure 13 have the same grounded voltage, it is advantageous to consider it as an independent electrode, to calculate the existing charges in this electrode due to the voltage at the other electrodes.

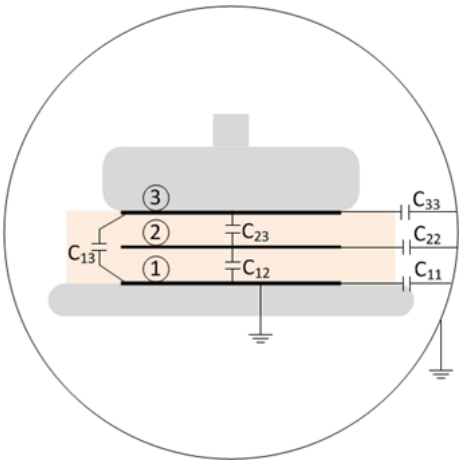

Figure 13. Two layers sample, with the representation of the bottom electrode (1), interface electrode (2), top electrode (3), and their mutual capacitances.

For the multilayer sample to resemble as much as possible a single layer dielectric with trapped charges, the interface should be as invisible as possible for the mechanical wave. This means that the interface electrode should have a thickness smaller than a tenth of the higher frequency wavelength component of the traveling acoustic signal used for the measurement. The small thickness allows us to neglect the acoustic interaction of the interface electrode and to avoid distortion in the acoustic signal due to differences in acoustic impedance and acoustic attenuation. A thin interface electrode also allows us to consider the different charges generated by the different mutual capacitances in the same electrode as an average value at the electrode position because of the limited resolution of the space charge measurement system in comparison with the thickness of the electrode.

Two methods to apply a voltage at the interface electrodes are discussed. First, a fixed electric connection between the interface electrode and a DC voltage source through a high resistance. Second, a removable connection between the interface electrode and a DC voltage source. Each method has its strengths and weaknesses.

A fixed electric connection between the interface and the DC voltage source can modify the voltage value at any time and keeps a constant value of charges to compensate for current leakage. The reason for the resistance is to avoid the free flow of charges during the transient of the space charge measurement. The RC time constant between the resistance and the sample capacitance should be several times higher than the pulse duration, so it does not affect the measurement. At the same time, it protects the DC voltage source from the pulsed voltage utilized for the PEA method.

The temporal connection method consists of applying a voltage at the electrode and then physically disconnecting the voltage source without reducing the voltage, so the charges stay in the electrode. The advantage is that the high resistance is not necessary because the voltage source is not capable of providing charges during the transient, and there is not an alternative route for the voltage pulse in case of the PEA method. The disadvantage is the

continuous depletion of charges at the interface because of leakage currents, which makes this method hard to apply.

3.3.1. Sample Preparation

The dual layer sample consists of two epoxy layers (Araldite MY 740, hardener HY 918), each one with a gold plating electrode of approximately 30 nm at the interface between layers, as shown in Figure 14. For the top electrode, it consists of 1 mm thickness semiconductor backed by 1 mm thickness aluminium electrode.

Figure 14. Dual layer epoxy sample with a 30 nm thickness gold electrode in-between layers.

The geometric characteristics of the samples are presented in Tables 1 and 2. It can be observed that as the thickness has a variation of approximately 0.06 mm across the samples, this will result in a small measurement distortion which can be seen in the measurements of Section 4. A small amount of silicon oil was used at the interface to improve the acoustic contact.

Table 4. Geometric properties of the dual layer sample.

Property	Top Layer	Bottom Layer
Diameter	41.5 mm	55.8 mm
Thickness	0.91 ± 0.06 mm	0.67 ± 0.06 mm
Gold plating diameter	37.4 mm	37.4 mm

Table 5. Geometric properties of the single layer sample.

Property	Single Layer
Diameter	55.8 mm
Thickness	1.86 ± 0.06 mm
Gold plating diameter	37.4 mm

3.3.2. Measurement Test setup for the multilayers sample.

In Figure 15 it can be observed the equivalent circuit of the PEA test cell including the multilayer flat sample utilized for the experiments. A fixed DC voltage source connection was utilized to control the voltage at the inner interface electrode. The DC source is connected through a resistance of 200 MΩ to increase the time constant and make the change in charges at the electrode during the pulse injection neglective.

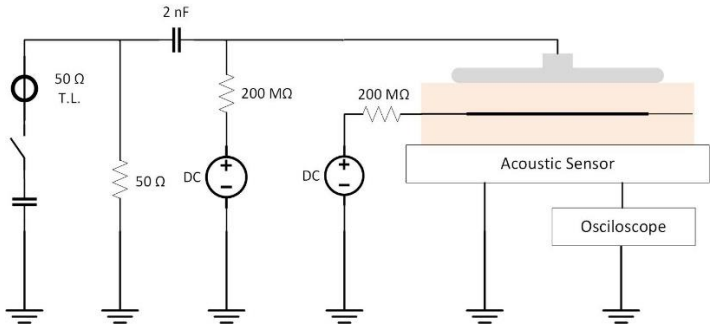

Figure 15. Test setup utilized in the multilayer sample.

The expected charge-voltage relation at each of the electrodes was calculated with the aid of finite element software to get the values for the mutual capacitance matrix. The geometric characteristics of Table 5 were utilized for the modeling of the Multilayer samples with each of the electrodes (top electrode, internal interface electrode and bottom electrode) modeled, because of the nanometer thickness of the interface internal electrode, it was modeled as an infinitely thin boundary. The relative permittivity used for the epoxy was 4.1.

Utilizing the obtained mutual capacitances from the finite element simulation. The charge values at different applied voltage levels can be calculated using Equation (11). Figure 16 shows the relation of the surface charge density at each electrode and the voltage at the interface, keeping a fixed 5 kV voltage at the top electrode while grounding the bottom electrode. For the performed tests, low voltage values were used to avoid space charge accumulation in the epoxy during the short duration of each test. Because of the interface electrode thickness, the charges at each electrode are treated as surface charge density instead of volume charge density, which is more common for PEA measurements.

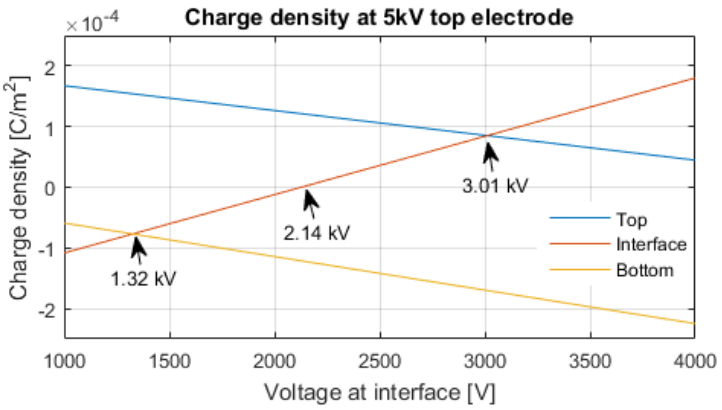

Figure 16. Dual layer sample interface voltage-charge relation for each electrode.

In Figure 16, three interface voltage values that were used in the tests are shown. Applying 5 kV at the top electrode and different voltages at the interface electrode, different charge values will be present at the different electrodes. With 1.32 kV at the interface electrode, the charge density at the bottom electrode is equal to the charge density at the interface. With 2.14 kV at the interface electrode, the charge density is zero. With 3.01 kV at the interface electrode, the charge density at the top electrode is equal to the interface charge density.

As seen in Table 4 and Table 5, the single layer electrode is thicker than the total dual layer sample. To make a meaningful comparison between the two samples, the electric field between the top and bottom electrodes should be the same to generate an equal amount of surface charges. To achieve this, the top electrode voltage and the pulse voltage used at the dual layer sample are multiplied by a k_d factor for the single layer sample:

$$k_d = \frac{d_s}{d_d} \tag{3.15}$$

where d_s is the single layer sample thickness [m] and d_d is the total dual layer sample thickness [m]. This means that the applied voltage at the single layer sample will be k_d times the voltage at the external electrodes of the dual layer sample. The applied pulse voltage was also multiplied by this constant.

3.3.3. PEA measurements using multilayer sample: Results

For all the tests, the duration of the measurements was less than 30 s. With the short duration of the tests and the low electric fields, no significant space charge is considered to develop. The measurement results are shown as the voltage signal without any post-processing involved, in order to compare the electric and mechanical distortions at each

sample. Practically this means that the results are shown as the measured voltage signal at the oscilloscope and not in charge values.

For the experimental results, first a comparison between the single layer sample and the dual layer sample at zero interface charge were performed. A voltage of 5 kV at the top electrode and 2.14 kV at the interface (see Figure 5) was used for the dual layer sample. For the single layer sample, following the Equation (3.15), 5.9 kV were used at the top electrode to keep the electric field equal (≈3.17 kV/mm) at both samples.

3.3.3.1. Comparison between Single Layer and Dual Layer Sample

From Figure 17a and Figure 17b, we can compare the signal from the single and dual layers samples. It is observed that the signal voltage which represents the charges at the bottom electrode for both samples are equal. For the top electrode, the magnitude looks almost equal. Nevertheless, it can be observed that in the dual layer sample the value is slightly bigger. This difference is attributed to the smaller thickness of the sample which results in less traveling path for the acoustic signal and therefore it has suffered less attenuation.

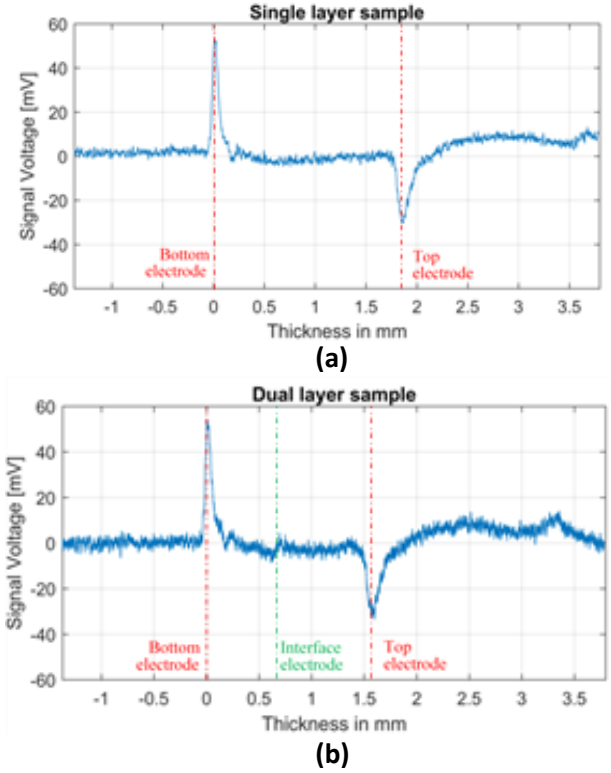

Figure 17. PEA signal without post-processing of 500 averaged measurements. (a) Single layer sample at 5.9 kV top electrode. (b) Dual layer sample at 2.14 kV interface and 5 kV top electrode.

In Figure 17b, at the interface, small disturbance peaks can be distinguished which resembles heterocharges. These peaks can be attributed to two factors: First the non-uniform thickness of the built samples (not to be confused with surface roughness), which results in a not-completely uniform electric field across the interface electrode resulting in a measured signal. The second factor is the polarization at the interface electrode (non-uniform permittivity at the interface because of the silicon oil), which even with the minimum thickness of the interface electrode in comparison to the resolution of the measuring system, it can be noticeable. The inhomogeneity of the interface such as the oil, and on a microscale the existence of oxidation layers, cavities and impurities between the layers can also produce the accumulation of charges [65–67]. Nevertheless, because of the short duration of the test and the low electric field, the accumulation is estimated to be negligible.

Even with the measured signal at the interface of the dual layer sample, the top and bottom electrode measured signals are consistent between both samples. Meaning that in the case of a non-zero total amount of charges at the interface of Figure 17b, the influence is not significant enough to affect surface charges at the electrodes.

It is worth to mention that the negative peak just after the bottom electrode peak, is not accumulated space charge, but the combination of the piezo-amp response and the direct response of the acoustic signal due to the non-ideal voltage pulse waveform which has a small undershoot. In the consecutive peaks, this pulse distortion cannot be seen because the acoustic losses have dissipated it.

3.3.3.2. Measurement of Generated Charges at the Interface Electrode

Figure 18a and Figure 18b show the measured values in the dual layer sample with different voltages at the interface electrode. In Figure 18a we can observe the measured signal with the epoxy-epoxy interface voltage at 1.32 kV. With this voltage at the interface, the charge value at the epoxy-epoxy interface should be equal to the charge value at the bottom electrode. The measured difference in the experimental test is because of the acoustic attenuation of the material. The difference in the acoustic impedance mismatch at the bottom electrode-epoxy interface and the dielectric-dielectric interface should not affect the signal as it is shown in Equations (3.1)–(3.10), because both layers of the dielectric are of the same material. It can be explained in the following way:

$$\tilde{p}_{bot}(t_0) = \tilde{p}_s(t_0) \tag{3.16}$$

Combining Equations (3.1) and (3.3) with (3.7)–(3.10), and neglecting the acoustic losses for a moment, it gives us:

$$\tilde{p}_{bot}{}'(t_0) = \left(\frac{Z_{bot}}{Z_s + Z_{bot}}\right)\tilde{p}_{bot}(t_0) \tag{3.17}$$

$$\tilde{p}_s{}'(t_0 + {}^{x}/_{v}) = \left(\frac{Z_s}{Z_s + Z_s}\right)\left(\frac{2Z_{bot}}{Z_s + Z_{bot}}\right)\tilde{p}_s(t_0) \tag{3.18}$$

where x is the distance from the bottom electrode to the dielectric-dielectric interface [m]. As we can see, the coefficients are the same for both signals:

$$\left(\frac{Z_{bot}}{Z_s + Z_{bot}}\right) = \left(\frac{Z_s}{Z_s + Z_s}\right)\left(\frac{2Z_{bot}}{Z_s + Z_{bot}}\right) \tag{3.19}$$

$$\therefore \quad \tilde{p}_{bot}{}'(t_0) = \tilde{p}_s{}'(t_0 + {}^{x}/_{v}) \tag{3.20}$$

Figure 18b shows the measurement where the inner interface is at 3.01 kV. In this case, the acoustic attenuation (which should reduce the top electrode measurement because of the longer distance) and the acoustic impedance mismatch at the epoxy-electrode interface (which might increase the measured value at this interface) play a role and influence the measurement from which they are expected to have the same charge values. Following the same procedure as before and considering d as the distance between the top and the bottom electrode:

$$\tilde{p}_{top}(t_0) = \tilde{p}_s(t_0) \tag{3.21}$$

$$\tilde{p}_{top}{}'\left(t_0 + {}^{d}/_{v}\right) = \left(\frac{Z_s}{Z_{top} + Z_s}\right)\left(\frac{2Z_{bot}}{Z_s + Z_{bot}}\right)\tilde{p}_{top}(t_0) \tag{3.22}$$

$$\tilde{p}_s{}'(t_0 + {}^{x}/_{v}) = \left(\frac{Z_s}{Z_s + Z_s}\right)\left(\frac{2Z_{bot}}{Z_s + Z_{bot}}\right)\tilde{p}_s(t_0) \tag{3.23}$$

$$\left(\frac{Z_s}{Z_{top} + Z_s}\right)\left(\frac{2Z_{bot}}{Z_s + Z_{bot}}\right) \neq \left(\frac{Z_s}{Z_s + Z_s}\right)\left(\frac{2Z_{bot}}{Z_s + Z_{bot}}\right) \tag{3.24}$$

$$\therefore \quad \tilde{p}_{top}{}'\left(t_0 + {}^{d}/_{v}\right) \neq \tilde{p}_s{}'(t_0 + {}^{x}/_{v}) \text{ if } Z_{top} \neq Z_s \tag{3.25}$$

It must be taken into account that in Equations (3.17) to (3.25), the mechanical losses of the sample ($\alpha(\omega)$ and $\beta(\omega)$) are not considered, which adds to the difference in the results of Figure 18.

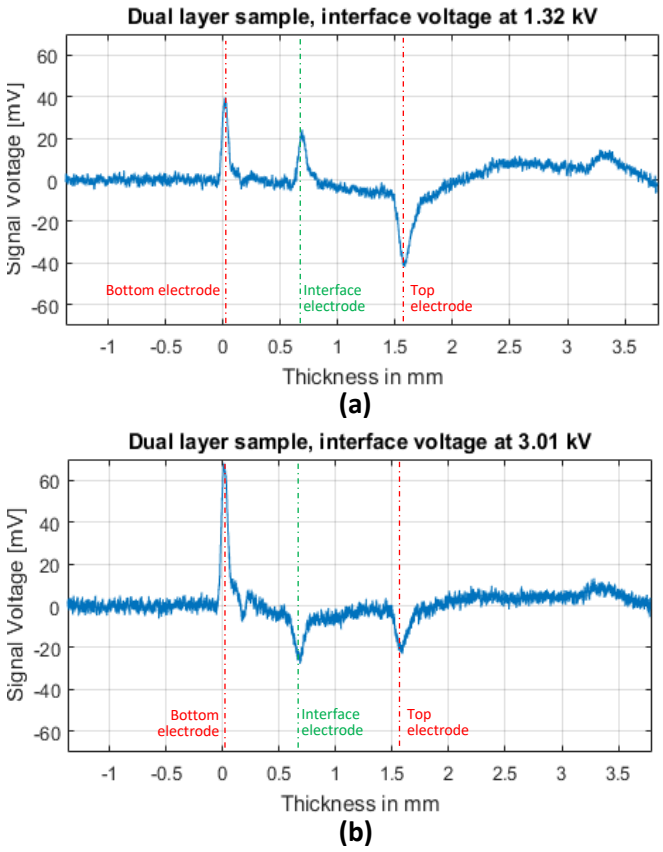

Figure 18. PEA signal without post-processing of 500 averaged signals, at 5 kV top electrode using the dual layer sample. (a) 1.32 kV at the interface electrode. (b) 3.01 kV at the interface electrode.

3.3.4. Equipment Characterization

The use of the calibrated samples presented in this work can be used to compare and analyse the accuracy of space charge measuring systems (including equipment setup and post-processing analysis).

The procedure consists in performing short time duration measurements at the proposed calibrated samples. The short duration of the measurements is to avoid significant accumulation of space charges and only measure the surface charges induced at the electrodes. The resultant values of space spaces after the post-processing can then be compared with the pre-calculated values of charge density at each electrode of the calibrated sample. The deviation of the comparison reflects the accuracy of the measurement system under test.

An example of the process is shown in Figure 19. In the figure, the previous measurements using the dual layer sample with voltages at the interface of 2.14 kV (Figure 17b) and 1.32 kV (Figure 18a) were utilized. As a first step, the measurement with 2.14 kV at the interface (which represents a space charge free sample), was utilized to obtain the postprocessing parameters (post-processing procedure is described in Chapter 2). Once these

parameters are calculated, they can be utilized for the postprocessing to obtain the space charge density values from the dual layer sample with 1.32 kV interface voltage (which represents a surface charge accumulation at the internal electrode location).

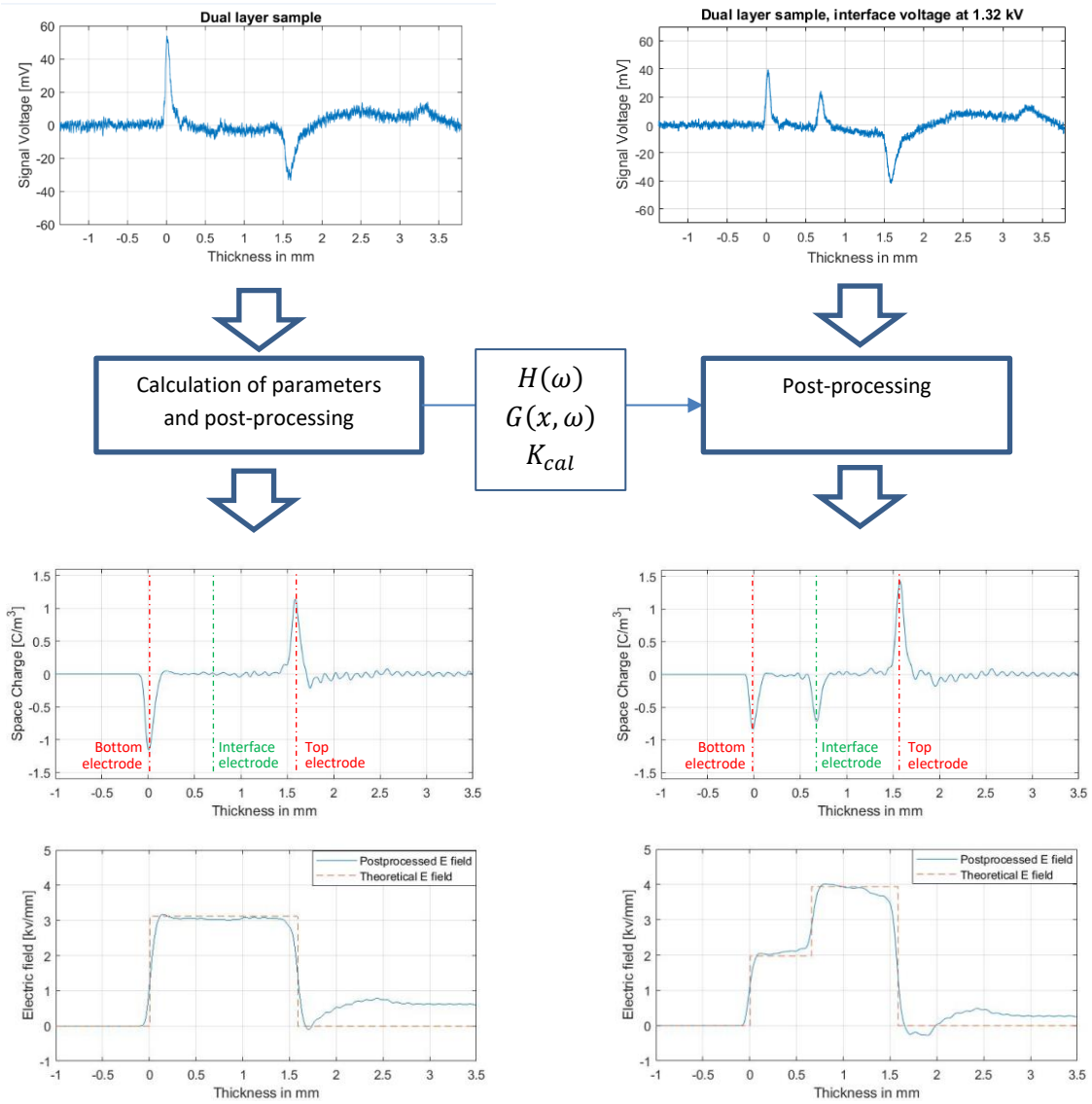

Figure 19. Postprocessing of measured values for space charge distribution calculations of the dual layer sample with 1.32 kV inner electrode voltage, using the measured signal with 2.14 kV inner electrode voltage to calculate the post-processing parameters.

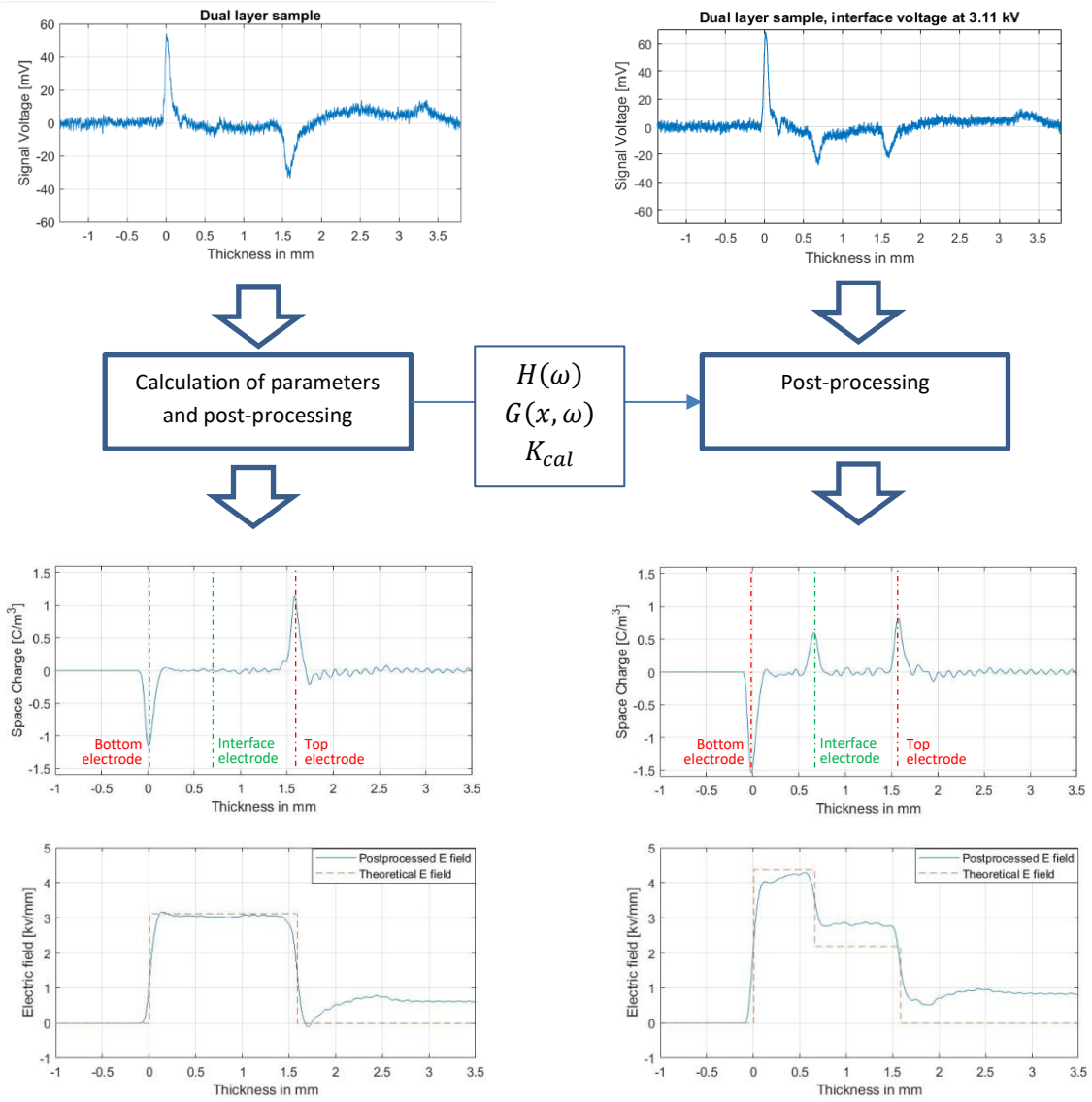

Figure 20. Postprocessing of Measured values for Space Charge distribution calculations of the dual layer sample with 3.11 kV inner electrode voltage, using the measured signal with 2.14 kV inner electrode voltage to calculate the post-processing parameters.

Afterwards, both processed measurements can be compared with the precalculated charge values expected at the different electrodes (including the internal interface electrode). The surface charge values at each electrode can be calculated by the integration of the space charges at each of the electrode peaks (see Figure 19). The comparison from the calculated values from the measurements, and the expected values (see Figure 16) is shown at Figure 21. The difference between the measured values and the expected values is attributed to inaccuracy due to the postprocessing and small deviations in the applied voltage. Small errors due to possible imperfect acoustic continuity at the interface are not discarded.

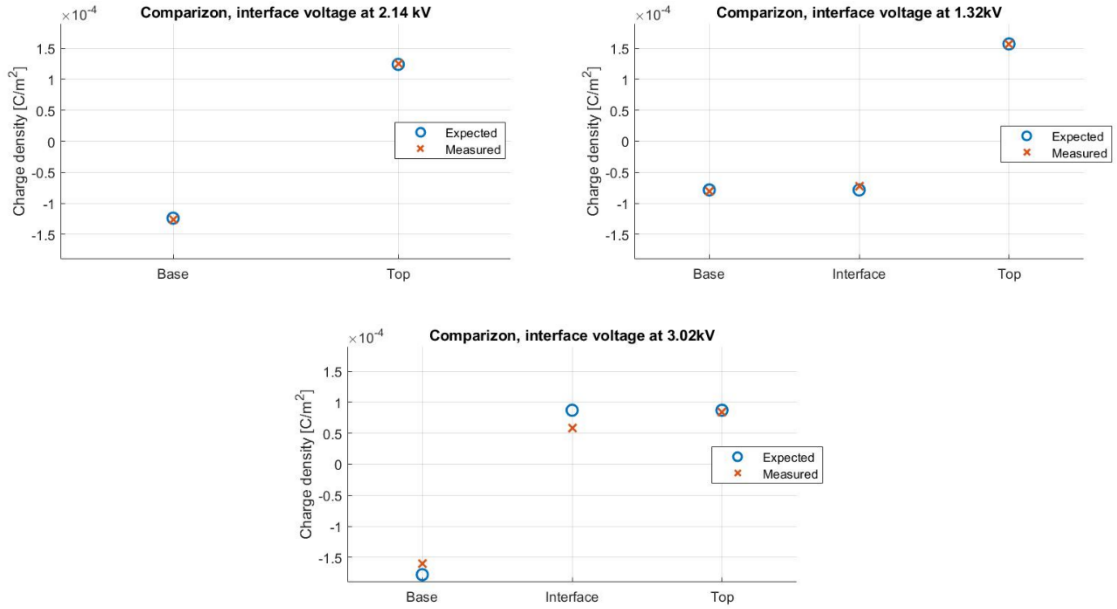

Figure 21. Comparison of post-processed charge values and expected values.

3.4. Chapter Summary

The difference in the acoustic properties of the electrodes have a relevant impact in the calibration of the acoustic methods to measure space charges.

The use of a reference sample with thin electrodes can be used to calculate the transfer function for the attenuation and dispersion of the acoustic signal across the sample and used for the post-processing of the measurements at the actual sample of interest as the conditions of the testing may require the use of electrodes that create acoustic inhomogeneities at the electrode interface.

Two factors that should be considered for the use of a reference sample are: First, the mechanical properties of the reference sample need to match the mechanical properties status at the sample of interest. For example, if the acoustic properties of the dielectric are highly temperature dependent, the transfer function from the reference sample should be calculated matching the temperature to which the sample of interest will be subjected, the same applies with the applied pressure to the sample and electrodes. Second, the thickness of the reference sample has an impact in the maximum frequency to which the calculated transfer function is valid, the thinner the sample, the more frequencies that do not become totally attenuated and that can be recovered.

The use of multilayer samples with electrodes at the layers interface can represent a single layer dielectric with known charge values in a localized region. The sample can be used for reference measurements and calibration of measuring equipment because of its capability of having known charges at each electrode. Because of the small thickness of dielectric-

dielectric interface electrode, it can be considered as an area distribution of charges instead of a volume and use it to verify the spatial resolution of the space charge measuring system.

The PEA method was used as an experimental test, but the multilayer samples with an interface electrode are expected to work for any acoustic or thermal method, but further research might be required.

The construction of the multilayer samples requires special attention to keep each layer with a constant thickness and to avoid the effect of the small distortion at the interface as the one observed in Figure 17.

A sample with several layers can be used to quantify the acoustic attenuation by comparison of the internal electrodes, without the interference of the acoustic impedance mismatch at the external electrode interfaces. The proposed method could apply to multilayer samples with different dielectric materials, but further research is required.

4. PEA test cell for full size HVDC cables

In the previous chapter the focus was on flat samples for the calibration and characterization of the measurements. In the following chapters the focus is on measurements at HVDC cables, which have a direct application in laboratory measurements an in real components in HVDC systems.

For the following chapters of this work, it was required to build a PEA setup for space charge measurements in full size cables (20 mm dielectric thickness or higher). This will allow to observe and analyse the challenges that arise in the measurement of full-size cables. The minimum desired cable length to be utilized for the measurements of space charges should allow for enough space to be able to produce appropriate terminations for the applied DC voltage at each of the extremes and have enough space for the optimum installation of the PEA test cell.

For this purpose, a specific PEA test cell was developed which should be able to produce optimum measurements.

4.1. PEA test cell

4.1.1. Base Electrode

The PEA test cell was built considering the geometry of the cable sample. The detecting electrode at the PEA test cell was built from aluminium due to its optimum conductive and acoustic properties.

A flat geometry electrode was considered to facilitate the contact with the cylindrical geometry of the HVDC cables without the restriction of specific diameters [68], together with the easier manufacture process that it requires. Between the base electrode and the HVDC cables, silicon oil was utilized as coupling medium.

Base Electrode Thickness

For the aluminium electrode thickness, the dielectric thickness of the cable test sample needs to be considered. As described in [69] the minimum thickness of the aluminium required to avoid overlapping of the signal due to acoustic reflections follows:

$$d_{Al} > \frac{v_{AL}\tau_{SC}}{2} \tag{4.1}$$

$$\tau_{SC} = \frac{d_d}{v_d} + \frac{d_{os}}{v_{os}} + \tau_p \tag{4.2}$$

where d_d, d_{os} and d_{Al} are the thicknesses of the sample dielectric, the outer semiconductor and aluminum electrode, respectively; v_d, v_{os} and v_{AL} represent the average acoustic propagation velocities of the dielectric sample material, the outer semiconductor and the aluminum electrode, respectively; and τ_p is the applied voltage pulse duration. The τ_p is the pulsed voltage duration, and it is considered in order to allow the measurement of the whole duration of the acoustic signal belonging to the inner conductor of the cable without being distorted by the overlap of any reflection. The considered acoustic propagation speeds for the aluminum and XLPE were 6420 m/s and 2000 m/s, respectively, as mentioned in Table 6.

Table 6. Considered acoustic propagation speeds

Material (symbol)	Acoustic speed (m/s)
XLPE (v_{XLPE})	2000
Cable semiconductor (v_{os})	2000
Aluminium (v_{Al})	6420
PVDF (v_{PVDF})	2260

With a cable insulation thickness of 21.5 mm, an outer electrode thickness of 1.5 mm and a pulsed voltage duration of 300 ns, the minimum thickness of the aluminum electrode required to avoid the overlapping of the signal due to reflections is 37.86 mm. A representation of the acoustic propagation and reflections at the base electrode for these geometries is represented in Figure 22.

Two flat electrode thicknesses were utilized for the experiments as can be seen in Table 7. The 120 mm was utilized for the PEA measurements performed in KEMA labs and for the experiments for the pulsed voltage connection configuration at chapter 5.2. The 40 mm thickness was utilized at the experiments for the electromagnetic reduction by impedance grounding and pulsed voltage electrode configuration.

Table 7

Aluminium Electrode	Thickness	Lateral dimenxions
Configuration A	120 mm	300 mm x 300 mm
Configuration B	40 mm	300 mm x 300 mm

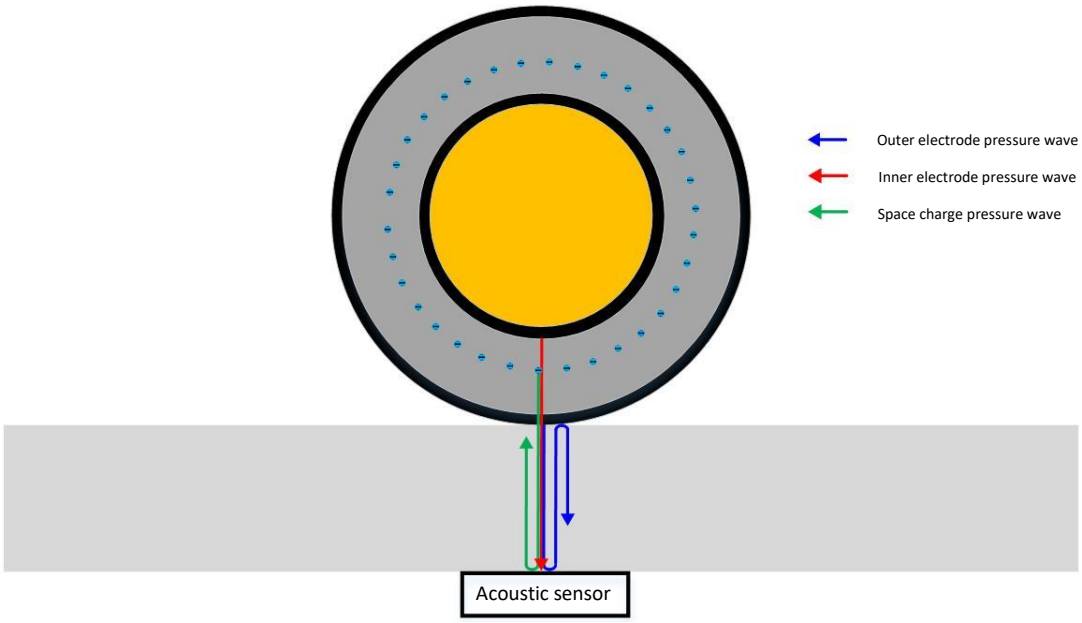

Figure 22. Representation of the acoustic propagation of the pressure waves generated at the inner electrode, outer electrode and at internal space charges for a 21.5 mm dielectric thickness, 1.5 mm outer electrode thickness and 40 mm aluminium base electrode thickness.

Base Electrode Lateral Dimensions

The lateral dimensions of the base electrode need to be considered, as the reflection of the acoustic waves will also reflect at the lateral faces and may overlap with the useful signal at the acoustic measurement window.

Considering an infinitesimal contact point between the HVDC cable and the aluminium electrode, at the moment of applying a voltage pulse across the cable dielectric, the acoustic signals generated at the outer electrode will propagate as depicted in Figure 23. To avoid the reflection at the lateral walls to reach the acoustic sensor during the space charge measurement window, the minimum lateral dimension w_{al} of the measuring electrode should be [70]:

$$w_{al} \geq v_{al}\tau_{SC}\sqrt{1+\frac{2d_{al}}{v_{al}\tau_{SC}}} \tag{4.3}$$

In Figure 23 is represented the fraction of the initial acoustic signal which is reflected at the lateral walls of the base electrode (blue arrows), together with the acoustic signal from the inner electrode that directly reaches the acoustic sensor (red arrow). To avoid overlapping, the reflected acoustic signal at the lateral walls of the base electrode must reach the acoustic sensor after the useful measuring window is finished, which is dictated by the acoustic signal of the inner electrode. In a real case the represented acoustic signal paths will slightly deviate

because contact area between cable and electrode creates a non-infinitesimal contact point. Still, equation (4.3) can be utilized to set a dimensional limit consideration for the geometric dimensions of the electrode.

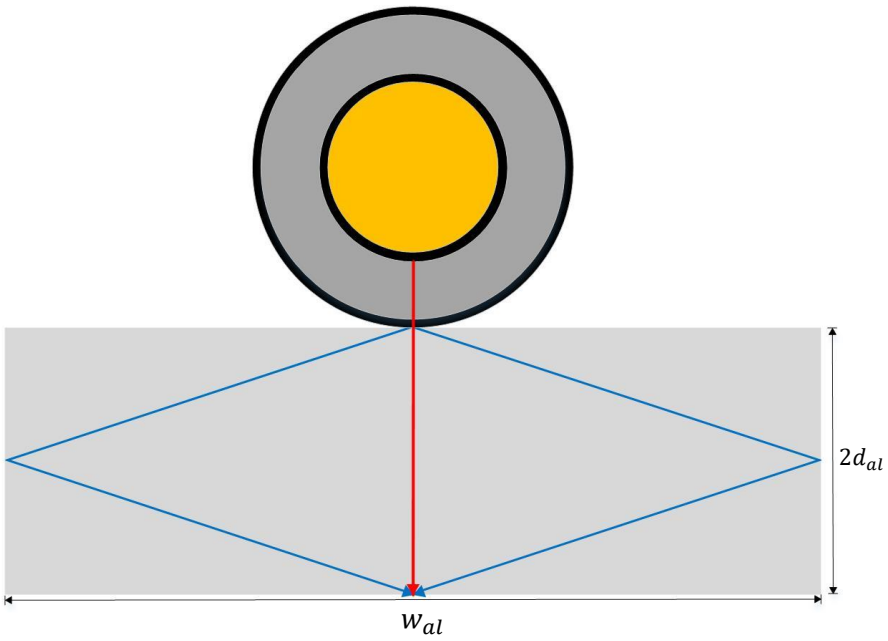

Figure 23. Comparison of traveling distances between the last useful acoustic wave from the measuring window belonging to the inner electrode and the component of the acoustic waves belonging to the outer electrode that reflect at the base electrode lateral walls.

4.1.2. Acoustic Sensor

The design of the acoustic sensor plays a key role for the optimum performance of the measurement cell. The transducer consists of a polarized PVDF piezo film.

Sensor Thickness

The selected thickness must be small enough to achieve a desired spatial resolution while at the same time a higher thickness achieves a higher output signal magnitude, increasing the signal to noise ratio.

The induced voltage across the piezo film sensor is due to the integral of the existing pressure waves across its thickness. This means that to optimize the spatial resolution, the sensor thickness must be smaller than the minimum wavelength of the acoustic pressure wave across the PVDC film. The acoustic wavelength depends on the applied pulsed voltage (the acoustic dispersion as it propagates across the different materials will have an influence) and the acoustic propagation speeds of the material.

$$\tau_p v_{PVDF} \gg d_{PVDF} \tag{4.4}$$

where τ_p is the pulsed voltage duration and d_{PVDF} is the thickness of the polarized PFDV piezo film.

Sensor Area

Increasing the area of the piezo film has the advantage to increase the RC constant of the sensor and in consequence increasing the bandwidth for the low frequency components. This is true as long as the acoustic pressure waves reach the whole piezo film area approximately at the same time, if this is not accomplished, the measured signal will be distorted, and the spatial resolution will be reduced.

Due to the coaxial geometry of cables, and the flat geometry of the sensor electrode, the acoustic waves will follow a circular wavefront from the sample-electrode point of contact, as they propagate. This will limit the width that can be applied to the sensor because the pressure waves reach the sensor with an increasing delay in relation to the distance from the center of the sensor.

Sensor Backing Material

Another important factor is the backing of the PVDF piezo film. The acoustic impedance between the piezo film and the backing materials needs to be as close as possible to avoid reflections at the interface which will have an impact in the output signal. At the same time, the thickness of the backing material needs to be big enough to avoid that the signal reflected at the end of the backing material reaches the sensor before the end of the measuring window. In other words:

$$d_b > \frac{v_b}{2}\left(\frac{d_d}{v_d} + \tau_p\right) \tag{4.5}$$

where d_b and v_b refers to the thickness and the propagation speed of the backing material, respectively.

4.1.3. PEA test cell construction

For the built PEA test cell, the acoustic sensor consists of a 52 µm thick polyvinylidene fluoride (PVDF) piezo film, backed with 20 mm of non-polarized PVDF to avoid reflections and terminated with rubber for damping purposes. The contact area of the piezo film is 5 × 65

mm^2, with the longest side parallel to the length of the HVDC cable. The capacitance of the piezo is 0.83 nF. The PVDF piezo film was connected to two different amplification configurations:

- Charge amplifier with 1.6 kΩ input resistance and 30 dB gain, in series with two amplifiers of 20 dB (Mini Circuits ZFL-500-BNC), all of them battery powered.
- Charge amplifier with 1.6 kΩ input resistance and 30 dB gain, in series with one amplifier of 20 dB (Mini Circuits ZFL-500-BNC), all of them battery powered.

In Figure 24 can be observed an equivalent circuit diagram of the built charge amplifier directly connected to the piezo film, while Figure 25 shows a picture of the acoustic sensor and charge amplifier construction inside a shielding box. The design bandwidth of the amplifier is from 100 kHz to 100 MHz. In Figure 25 the PVDF material is not visible as this is below the visible brass plate utilized to apply pressure towards the aluminium electrode.

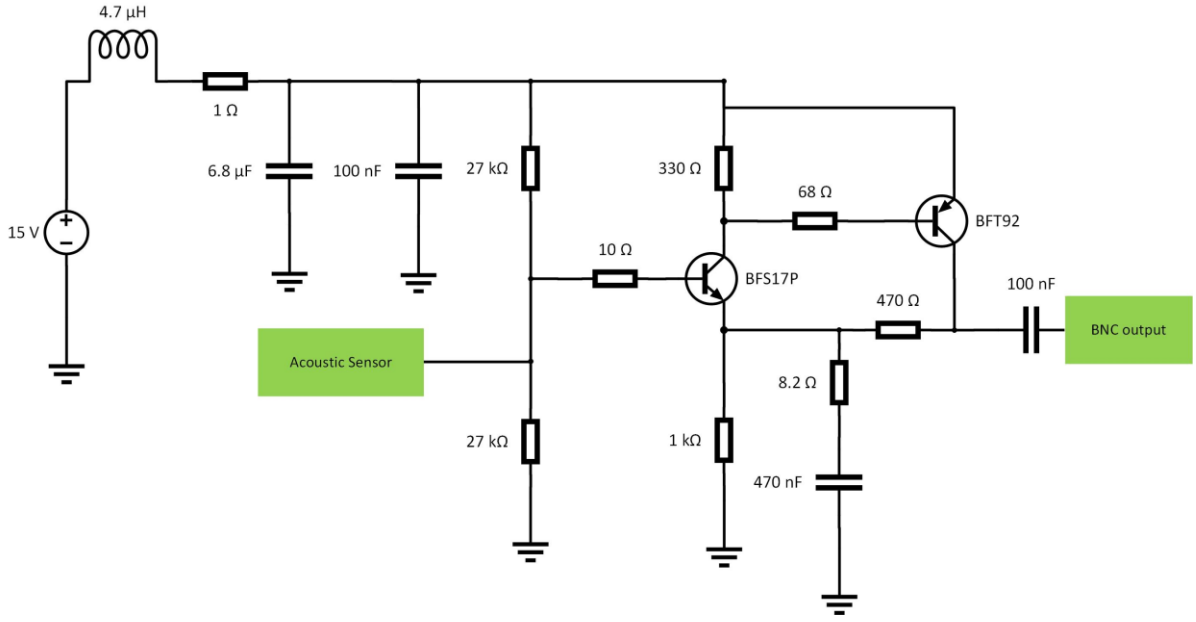

Figure 24. Charge amplifier equivalent circuit diagram.

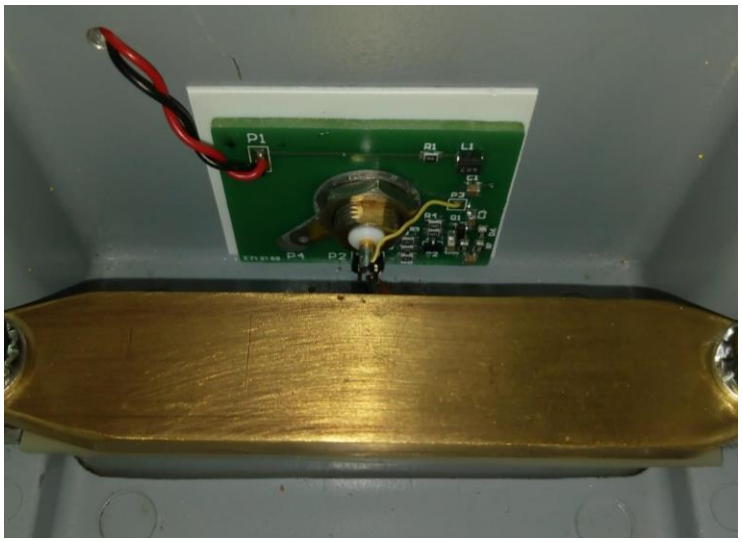

Figure 25. Shielding box containing the acoustic sensor and the charge amplifier.

A schematic representation of a PEA test cells is shown in Figure 26. The piezo film and the amplifiers are contained in an aluminum box of 400 mm × 200 mm × 120 mm external dimensions and 4 mm wall thickness. The pulse injection into the measurement electrode and guard electrodes shown in the figure is suitable for space charge measurements on full-size long cables [71].

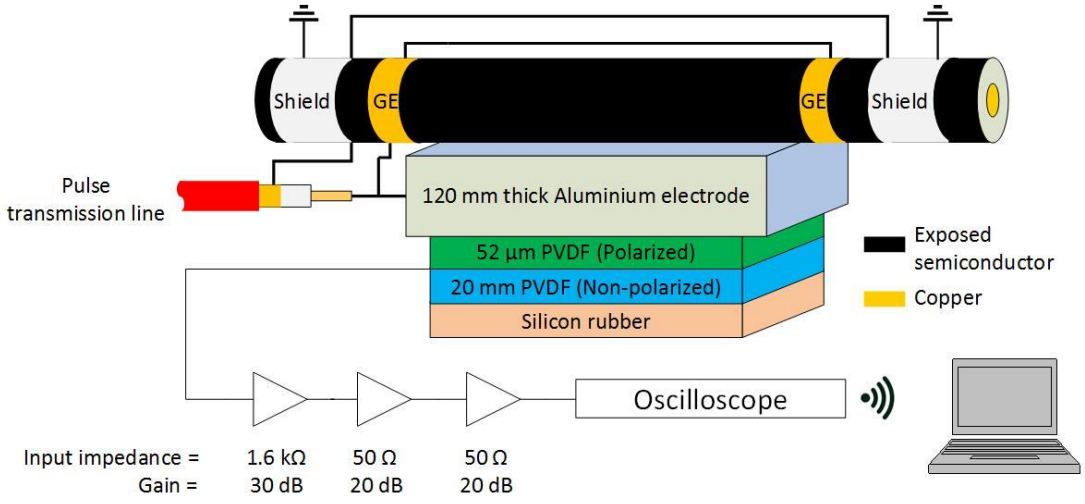

Figure 26. Representation of the PEA test cell including the acoustic sensor, amplifiers and oscilloscope. "GE" stands for Guard Electrode.

In Figure 27 is shown the construction inside the 400 mm x 200 mm x 120 mm aluminium box of the PEA test cell. During measurements the box is completely closed by an aluminium lid. The aluminium box contains the amplifier stages which are connected to the charge amplifier, an oscilloscope (Red Pitaya), the batteries for powering the electronic components and a second shielding box which contains the acoustic sensor and the charge

amplifier. The charge amplifier output is connected to the amplifiers utilizing a BNC connector wall plate. Using an USB wall through, the oscilloscope connects to a Wi-Fi antenna utilized to communicate to an external computer. The utilized battery does not utilize switching elements, to reduce any generated electrical noise. At the moment of the picture in Figure 27, only one 20 dB amplifier was connected to the charge amplifier.

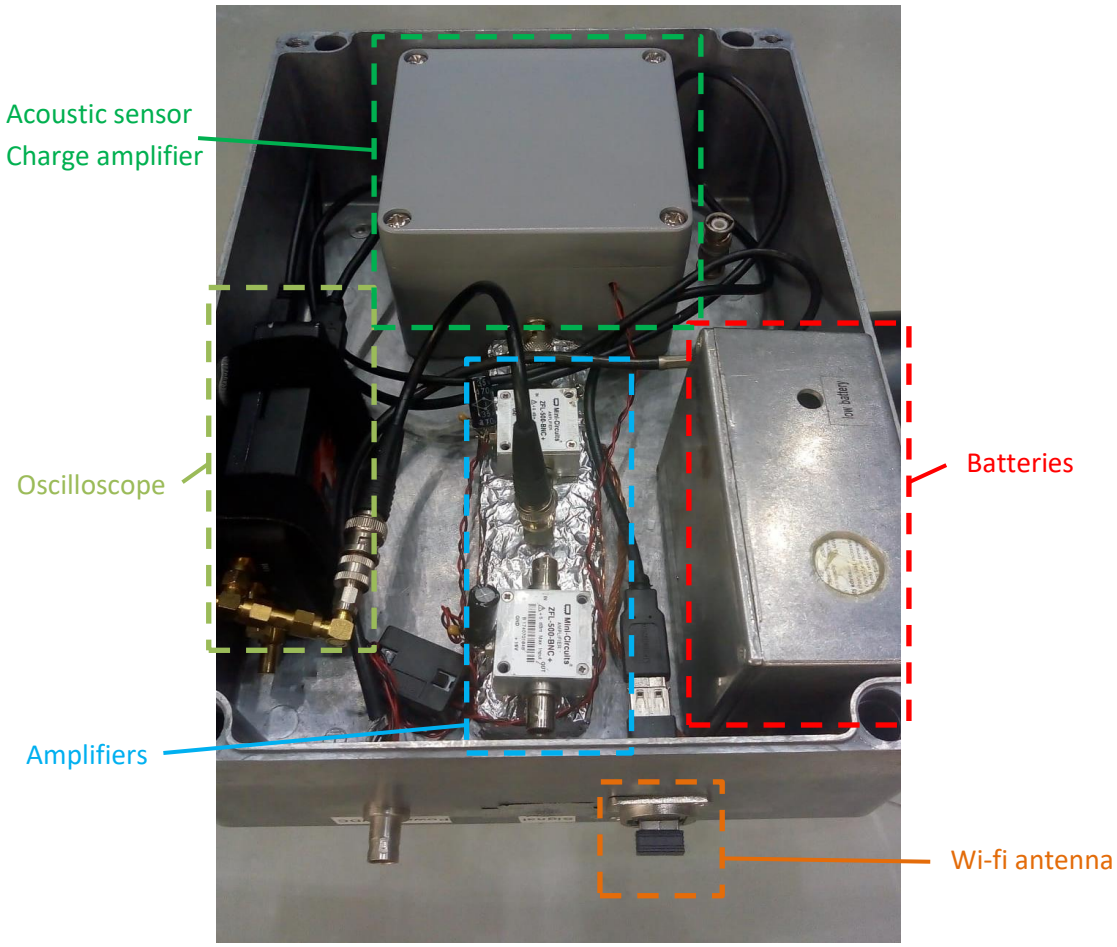

Figure 27. Interior of the 400 mm x 200 mm x 120 mm aluminium box of the PEA test cell. The aluminium box contains the second stage amplifiers, the oscilloscope, batteries and a second shielding box which contains the acoustic sensor and the charge amplifier. At the exterior of the box is visible the antenna utilized to send the measured data to an external computer.

4.2. Pulse Voltage Circuit

Due to the direct relation between the applied pulsed voltage across the dielectric and the generated acoustic signal, the pulsed voltage width has a direct relation with the maximum spatial resolution of the measuring system.

The voltage impulse is generated using a fast switch metal-oxide-semiconductor field-effect transistor (MOSFET) Behlke HTS 61-40 using a total of 150 nF from parallel connected discharge capacitors and a DC source to recharge the capacitors between each pulse. The

maximum charging voltage which the pulse voltage box can handle is 6 kV DC. The pulse width can be controlled by the length of the switch trigger with a minimum duration (on state of the switch) of 300 ns. The pulse box equivalent circuit is shown in Figure 28, where the circuit of the applied voltage pulse and the terminal connections of the transmission line that brings the voltage pulse to the PEA test setup side are named ICP for the inner conductor and OCP for the outer conductor. The OCP conductor is grounded at the switch

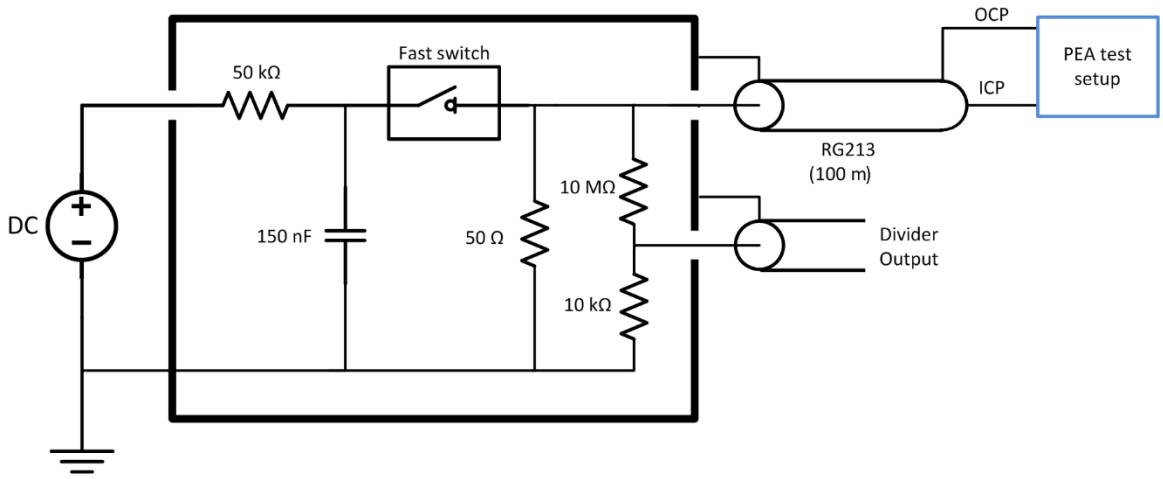

Figure 28. Voltage pulse generator equivalent circuit. OCP stands for the outer conductor terminal of the pulsed voltage cable at the PEA setup side, and ICP stands for the inner conductor terminal of the pulsed voltage cable at the PEA setup side.

The pulse travels from the switch box to the PEA test cell through a coaxial cable (RG213) of 50 Ω as characteristic impedance. The coaxial cable is approximately 100 m long to electrically decouple the switch from the test cell, as due to the propagation time and the pulse voltage duration, the pulsed voltage wavelength across the coaxial cable is shorter than twice the length of the coaxial cable. The cable is non-terminated at the PEA test cell side to maximize the applied voltage at the PEA test cell, due to the impedance mismatch between the coaxial cable and the PEA test cell connection. At the same time, the coaxial cable is terminated at the pulse generator side (switch box) to avoid multiple pulse reflections [72]. In Figure 29 can be seen an example of the measured voltage signal at the voltage divider built in the switch box (see Figure 28).

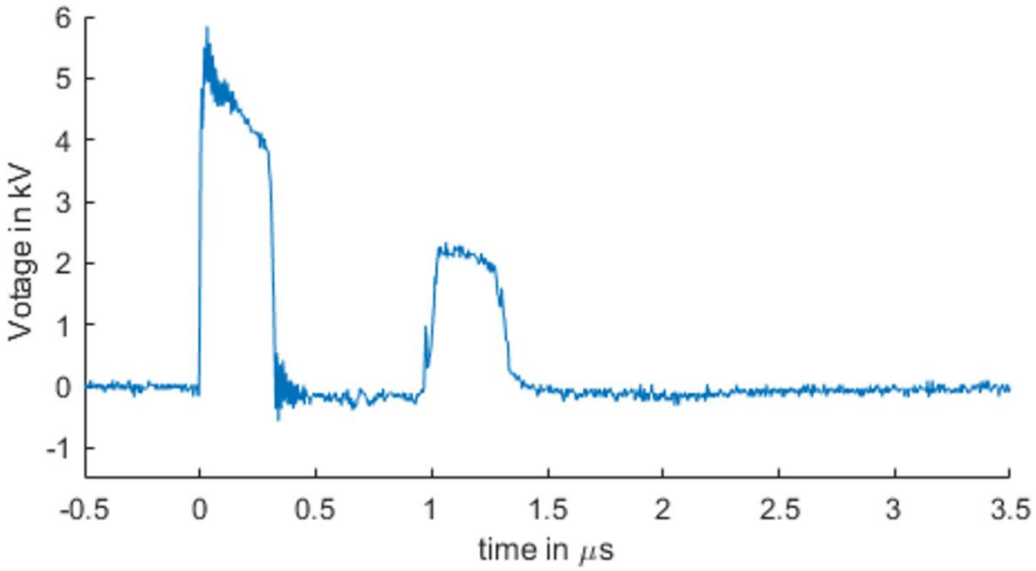

Figure 29. Measured voltage at the pulsed voltage generator. The signal from 0 to 0.3 µs belongs to the outgoing pulse; the signal after 0.9 µs is the reflected voltage at the HVDC connection.

In Figure 29, the first pulsed voltage initiated at measuring time = 0, belongs to the moment the pulse switch closes. At this moment, the voltage starts to propagate towards the connection at the PEA test cell and the HVDC cable. At approximately 0.5 µs (the velocity of propagation at the RG213 coaxial cable is 66% speed of light in vacuum) the pulsed voltage reaches the injection point, where a fraction of the voltage is reflected (increasing locally the voltage at the injection point). The reflected voltage reaches the switch box at approximately 1 µs as can be seen in the second measured voltage pulse in Figure 29. At the switch box arrival moment, the pulse switch is already closed, and the parallel 50 Ω resistance properly terminates the cable, to avoid further reflections which would affect the measurements. A graphical representation of the pulsed voltage propagation and reflection is depicted in Figure 30.

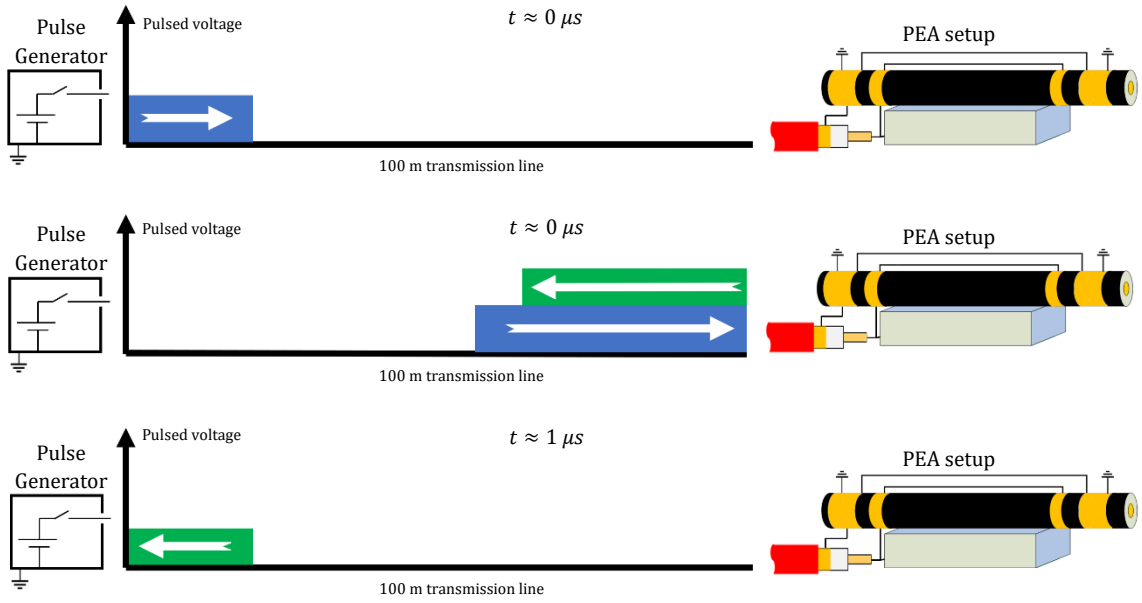

Figure 30. Representation of the pulsed voltage propagation and reflection between the pulse generator and the PEA setup.

It needs to be considered, that terminating the coaxial box at the switch box means that at the instant the pulse switch closes, it will feed an impedance half the value of the coaxial cable impedance (coaxial cable in parallel with the termination resistance). This means that the charging capacitors needs to be able to provide enough energy for the coaxial cable and the resistance termination during the pulse duration without having a significant voltage drop following the known equation:

$$V_c = V_0 e^{-t/RC} \tag{4.6}$$

where V_c stands for the voltage at the capacitor after t discharge time, R is the total equivalent resistance to which they are discharged (switch resistance, termination resistance and transmission line), C is the capacitance from the charging capacitors. At the same time, the current rating of the switch needs to be selected considering the total discharge current of the capacitors due to the equivalent impedance of the coaxial cable and the termination connected in parallel.

4.3. HVDC cable under test

For the tests, a 320 kV HVDC cable was utilized as a test object. Previous to this work, the cable was subjected to several type testing including HVDC application with nominal current during long time periods for both polarities, HV impulse, etc.

The cable uses copper as the inner conductor, and aluminum as the outer conductor. The dielectric material is cross-linked polyethylene (XLPE). The geometric characteristics of the HVDC cable sample are shown in Table 8.

Table 8

Property	Value
Inner conductor (diameter)	62.3 mm
Inner semi-conductive layer thickness	1.9 mm
Insulation thickness (XLPE)	21.5 mm
Outer semi-conductive layer thickness	1.5 mm
Cable weight	34.1 kg/m

The cable length utilized for measurements at KEMA laboratories was around 60 meters; later a 9 meters section of the same cable was translated to TUDelft HV laboratories to continue with the experiments. For both cases, at the middle section of the 9-meter cable, the outer layers of the HVDC cable were removed to expose the outer semiconductor and to mechanically fix the cable to the PEA test cell. The semiconductor layer was kept continuous, meaning that no section has been cut or removed to modify its electric continuity between electrodes. The outer semiconductor is in direct contact with the aluminum electrode of the PEA test cell. To ensure a good acoustic contact, silicone oil is used in the interface and compressive mechanical force is applied using screws.

4.3.1. TUDelft HV laboratory testing termination

For the experiments performed in TUDelft HV laboratories, it was designed a temporal HVDC termination for both extremes of the HVDC cable.

The termination consisted in removing the external shield from for a length of 2 meters at both sides of the HVDC cable. At the extreme of the HVDC cable, a section of the exposed inner conductor and around 20 cm of the exposed XLPE was covered with semiconductive tape 3M Scotch. Later, for electric field grading purposes, the rest of the exposed XLPE was covered by a dielectric tape with higher conductivity values than the XLPE. The applied dielectric tape was the Vinyl Mastic Tape: HelaTape Power 670 VM which has an electrical

conductivity of $1 \cdot 10^{-10}$ S/m. Figure 31 shows a graphical representation of the termination, while in Figure 32 it can be appreciated a picture of the termination.

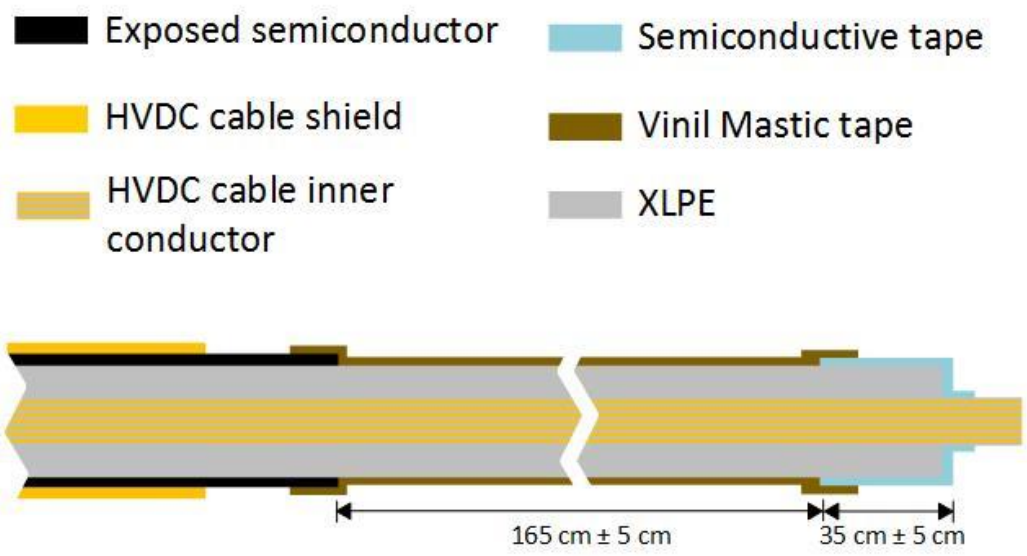

Figure 31. Graphical representation of TUDelft HV laboratory HVDC cable testing termination. The figure dimensions are not at scale, and the material colors are mainly for indicative purposes

Figure 32. Photo of one of the temporal terminations at the HVDC cable.

4.4. Measurements at KEMA laboratories

In order to test the built PEA test cell, the HVDC cable mentioned at section 4.3 was utilized as a test sample at the HVDC lab of KEMA laboratories. As previously mentioned, this cable had been previously subjected to several type testing, for which the existence of space charges was suspected.

In Figure 33 is presented a graphical description of the setup utilized in the tests. The cable was subjected to a thermal gradient by using the induced-current heating technique. This consists of inducing an AC current at the inner conductor. This was accomplished using current transformers while having the HVDC cable connected as a loop.

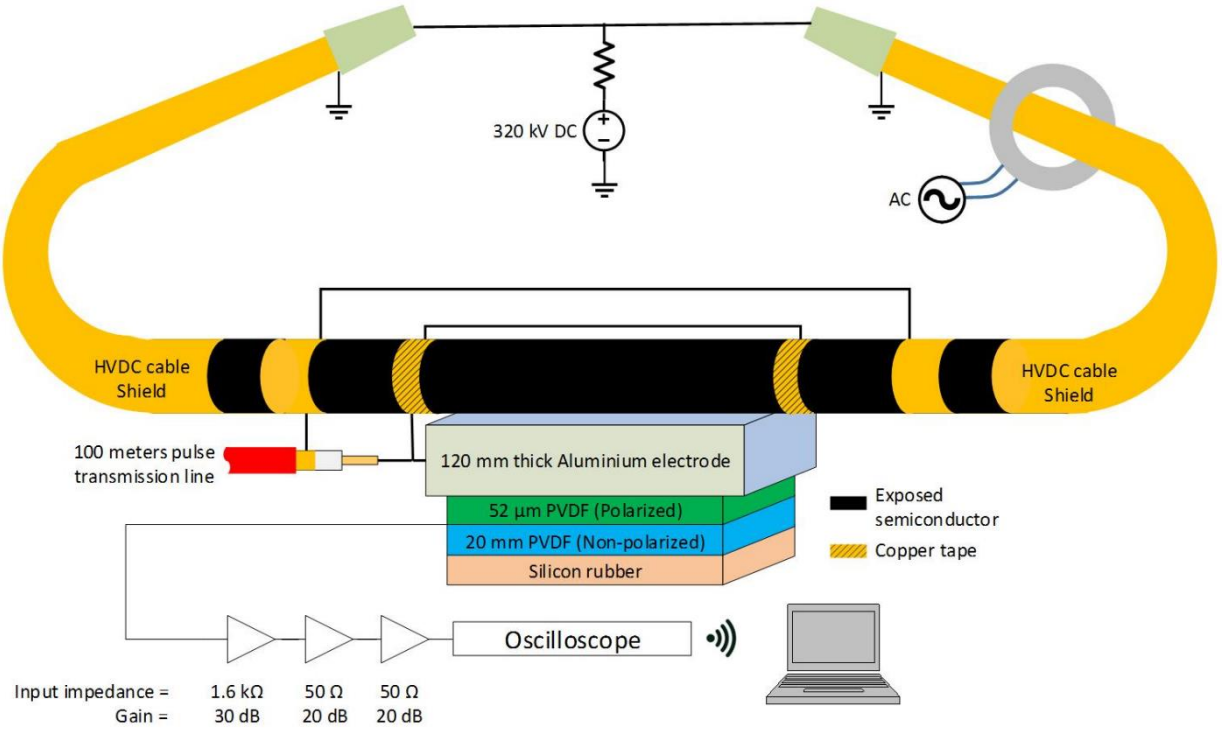

Figure 33. Representation of the PEA setup for measurements in a HVDC cable at KEMA laboratories.

The space charge measurements were done with 320 kV DC applied to the HVDC cable while the cable was being heated. The cable reached stable temperature in around 25 hours. During this transient, measurements with the PEA test cell were performed every 3 hours.

The measurements were performed with a 5.5 kV pulsed voltage generated at the pulsed voltage generator, which reaches the PEA test cell and is then partially reflected to the terminated pulsed voltage generator. In Figure 34, it is shown the measurements with 0 kV and 320 kV before heating the HVDC cable (no temperature gradient), and after 26.5 hours of heating (stable temperature gradient). The shown measured signals have not undergone through any post processing. In the figure, the time stamp 0 µs, represents the arrival time of the pulsed voltage at the PEA setup and the instant that the acoustic waves are generated. Around 19 µs it is observed that the acoustic signal from the outer electrode reaches the acoustic sensor, and at 32.5 µs the acoustic signal from the inner electrode.

From Figure 34, it can be observed the existence of space charges even before the application of the 320 kV and temperature gradient. Comparing the measured signals before and after the temperature gradient, the change due to accumulation of space charge during

the 26 hours of cable heating can be observed, specially at the inner electrode peak of the acoustic signal (around 32.5 µs).

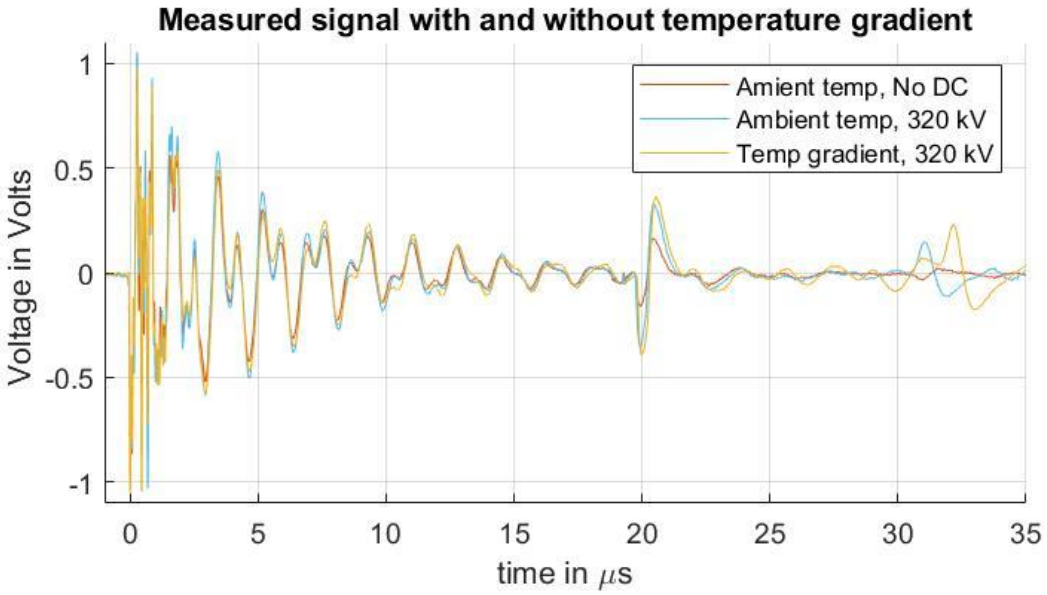

Figure 34. Measured signals at KEMA laboratories for a 320 kV HVDC cable including the measured signals before and after applying 320 kV HVDC without cable heating (no temperature gradient) and the measured after applying 320 kV HVDC after 26.5 hours of cable heating with a temperature gradient of 70° C at the inner conductor and 30° C at the outer conductor.

In Figure 34 can be observed several decaying oscillations initiating from time 0 µs which are attributed to the crosstalk of the pulsed voltage with the piezo amplifier.

For further testing, a section of 9 meters from the HVDC cable was transferred to TU Delft High Voltage Laboratory to perform further experiments to optimize the application of the pulsed voltage, which are described in Section 5.

5. Practical aspects for the pulsed voltage configuration and PEA test cell grounding for the influence at the electromagnetic distortion between pulsed voltage and piezo amplifier

5.1.Introduction

As described in Section 2.2.1, the PEA method consists of applying a pulsed voltage across the sample dielectric which temporary modifies the electrostatic force balance across the sample. This generates acoustic waves which can be measured to calculate the charges at the sample.

The PEA test cell forms part of the circuit for the application of the pulsed voltage. This fact has the consequence that during the application of the pulsed voltage at the sample, the transient voltage also interacts with the acoustic sensor. This interaction induces a disturbance in the sensor- amplifier circuit. Such a spurious signal can superimpose on the useful PEA signal, which can potentially lead to incorrect post-processing and analysis.

In Figure 35 it is shown an example of an induced distortion during the application of a voltage pulse of 300 ns at the time = 0 µs. The measurement was done for the HVDC cable sample described in Section 4.3. As can be observed, the application of the pulsed voltage, induced a measured distortion whose duration can be long enough to overlap with the relevant acoustic measurement window. In this case, the acoustic measurement from the charges due to the applied voltage reaches the acoustic sensor around 19 µs after the application of the voltage pulse, and we can see that there is a fraction of the distortion signal still present at the measurement to which the relevant acoustic signal is mounted.

This Chapter is based on:

Mier Escurra, G.; Rodrigo Mor, A.; Vaessen, P. Influence of the Pulsed Voltage Connection on the Electromagnetic Distortion in Full-Size HVDC Cable PEA Measurements. Sensors 2020, 20, 3087, doi:10.3390/s20113087.

Mier Escurra, G.; Rodrigo Mor, A.; Castro L.C.; Vaessen P. PEA Electromagnetic Distortion Reduction by Impedance Grounding and Pulsed Voltage Electrode Configurations. Sensors 2021, 21, 5837, doi:10.3390/s21175837.

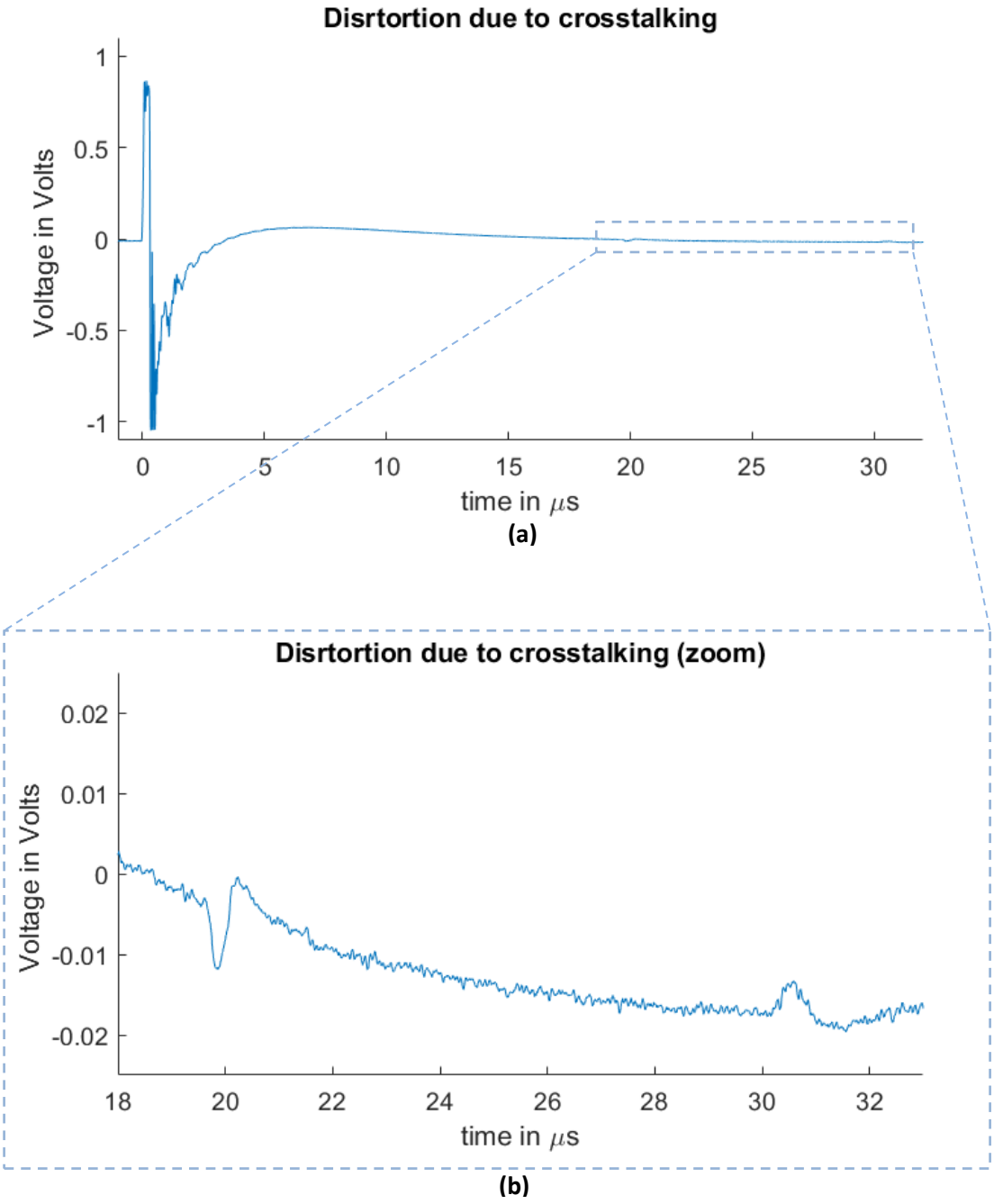

Figure 35. Example signal with the distortion due to the pulsed voltage and piezo amplifier crosstalk. The distortion duration is long enough to overlap with the relevant acoustic signal for the space charge measurements. (a) Full measured signal ranging from the instant of the pulsed voltage application up to 32 µs. (b) Zoom to the time instant of the acoustic signal arrival belonging to the charge measurements

A common procedure to compensate for the effect of the voltage impulse disturbance is to use measured signals without applied direct current (DC) voltage on the sample before it has accumulated space charges and to subtract it from subsequent measurements by software. This procedure may prove ineffective for measurements with pre-charged samples, as subtracting the disturbance will also subtract the space charge components. Moreover, in

extreme cases of pulse disturbance, the magnitude and duration of the distortion results in an effective reduction of the vertical resolution of the acoustic signal and may even result in the saturation of the amplifiers.

In most measurements using the PEA method, the post-processing calibration factors are obtained using a reference measured signal, whose charge values at the electrode's interfaces are known. This is the case for a sample with an applied DC voltage when the sample is space charge free. If the sample already has space charges, meaning that the reference signal cannot be directly measured, the reference signal can be obtained by means of two measurements: The first measurement is done by applying a known DC voltage, and the second measurement is done without DC voltage, as stated in [47]. These measurements are then subtracted, obtaining the reference signal in Equation (5.3):

$$V_{on}(t) = Ke_p[\sigma_{1-SC} + \sigma_{2-SC} + \delta_1 + \delta_2 + \sigma_1(E_{DC}) + \sigma_2(E_{DC}) + v\Delta T\rho(vt)] \quad (5.1)$$

$$V_{off}(t) = Ke_p[\sigma_{1-SC} + \sigma_{2-SC} + \delta_1 + \delta_2 + v\Delta T\rho(vt)] \quad (5.2)$$

$$V_{ref}(t) = V_{on}(\mathrm{t}) - V_{off}(\mathrm{t}) = Ke_p[\sigma_1(E_{DC}) + \sigma_2(E_{DC})] \quad (5.3)$$

where V_{on} and V_{off} represent the measured signal when DC is on or off, respectively. Subscripts "1" and "2" refer to the closest and farthest electrode, with respect to the acoustic sensor. e_p is the amplitude of the pulse voltage, σ_{1-SC} and σ_{2-SC} are the induced charges at electrodes 1 and 2 due to the trapped space charges, σ_1 and σ_2 are the capacitive charges at electrodes 1 and 2 due to the external applied DC voltage, δ_1 and δ_2 are the charges at each electrode due to the applied pulse voltage, E_{DC} is the external applied DC voltage, ρ is the bulk charge at the dielectric, v is the acoustic propagation speed at the dielectric, ΔT is the width of the voltage pulse and K represents the conversion factor of the acoustic sensor.

The previous procedure allows us to calibrate the measurements of a pre-charged sample, except in the case when the pulse disturbance time duration is longer than the acoustic propagation delay. In this case, the reference signal can still be obtained using the previous procedure, but it does not consider the distortion, as it gets eliminated during calculations. The problem arises when the calculated calibration factors from this reference signal are applied to the measurements with space charges and disturbance that are overlapped, as these two components cannot be separated. Equations (5.4) and (5.5) shows the calculation of the reference signal, where the distortion component named as K_{dist} gets eliminated so that the distortion will not be compensated in subsequent calculations:

$$V_{refdist}(t) = V_{ref}(t) = V_{on+dist}(\mathrm{t}) - V_{off+dist}(\mathrm{t}) \quad (5.4)$$

$$V_{on+dist}(\mathrm{t}) - V_{off+dist}(\mathrm{t}) = (V_{on}(t) + K_{dist}(t)) - (V_{off}(t) + K_{dist}(t)) \quad (5.5)$$

The optimal situation is to keep the influence of the distortion K_{dist} at a minimum. For this purpose, different construction factors which have an impact in the magnitude of the distortion were analyzed.

In section 5.2 it was analyzed the influence at the crosstalk between the pulsed voltage and the acoustic sensor due to the physical location of the pulse injection connection at the injection electrodes and the location of the grounding connection.

In section 5.3 the influence of the crosstalk is analyzed for the specific case when the PEA test cell is grounded. The grounding of the PEA test cell might be required due to specific requirements such as having a continuous measurement during long periods of cable testing which might require the powering of the PEA test cell devices during several days. The factors in consideration are the influence of the exposed semiconductor distance between the injection electrodes and the PEA test cell, and the influence of adding a reactance at the grounding circuit of the PEA test cell.

5.2. Influence of the Pulsed Voltage Connection and Grounding Connection on the Electromagnetic Distortion

In this section it is analysed the impact that different physical locations for the injection connection of the pulsed voltage at the PEA test cell has towards the magnitude of the generated distortion due to the crosstalk between the pulsed voltage and the acoustic sensor. Furthermore, the same analysis is conducted for the impact that the grounding configuration of the PEA test cell can have at the same distortion due to crosstalk.

5.2.1. Experimental setup

For the test experiments it was utilized the PEA setup and HVDC cable sample described in Section 4.

For the base electrode, the configuration A of 120 mm thickness from Table 6 was utilized. This configuration was the first version of the electrode utilized for the measurements. The thickness was selected to avoid the reflections of not only the acoustic longitudinal waves (but the shear waves that propagate approximately half the speed of the longitudinal waves); the achieved delay due to the thickness also allows for further decay of the electromagnetic distortion due to the pulse injection before the arrival time of the useful acoustic signal at the sensor. Nevertheless, it is not recommended to indefinitely increase the electrode thickness as the acoustic waves does have attenuation as it propagates across the aluminium due to geometric divergence and the inherent (small) acoustic losses in the

aluminium. At the same time the thickness of the base electrode has an impact in the overall weight of the PEA test cell. A graphic description of the setup can be seen in Figure 36, where it can also be observed that the amplification of the piezo film signal is amplified for a total of 70 dB.

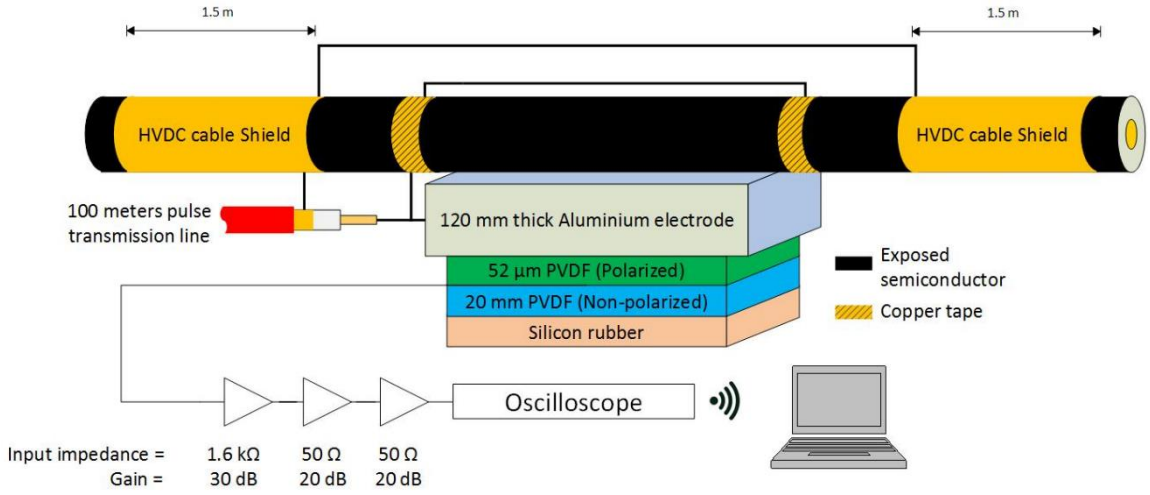

(a)

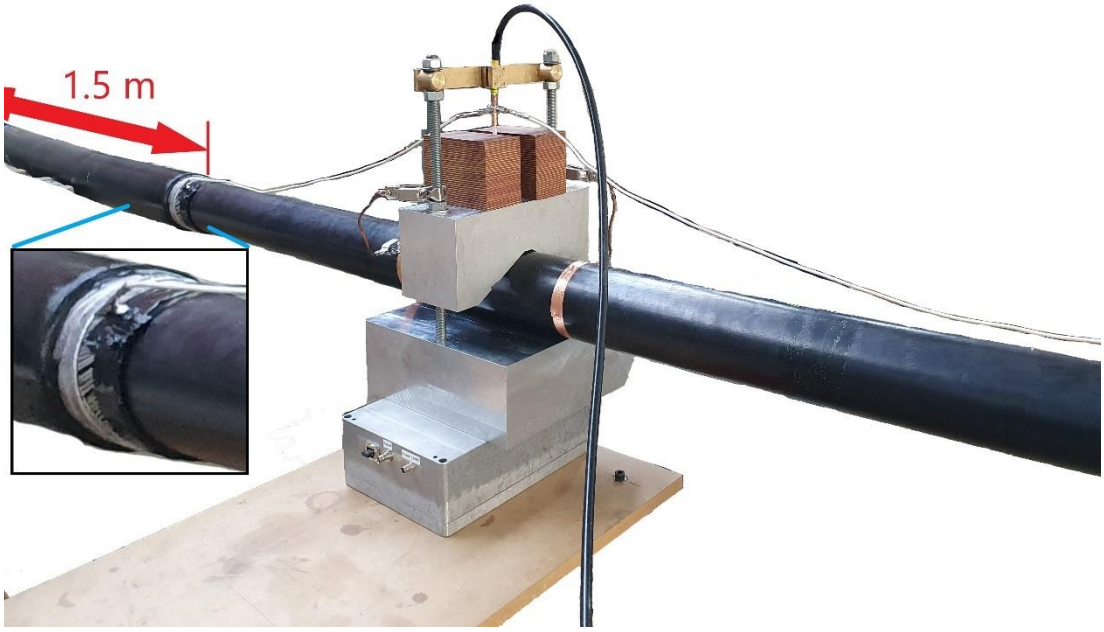

(b)

Figure 36. (a) Representation of the PEA test cell including the acoustic sensor, amplifier and oscilloscope. The sizes of the components are not at scale. (b) PEA test cell setup.

5.2.2. Test Experiments

The objective of the test experiments is to observe the impact of the pulsed voltage on the piezo-sensor distortion resulting from the current distribution across the PEA test cell during the pulse application. For this purpose, two sets of tests were performed, whose setups and results are described in Sections 5.2.2.1 and 5.2.2.2. Each set of tests consists of several cases regarding the connection's arrangements, described subsequently in this section.

In Section 5.2.2.1, a set of tests cell (Cases 1f, 1r, 2f, 2r, 3f and 3r) were performed to demonstrate the relevance in the selection of the pulsed voltage connection location at the PEA test cell for the generated piezo-sensor distortion. In Section 5.2.2.2, a set of tests (Cases 4f, 4r, 5f, 5r, 6f and 6r) were performed to compare and analyze the influence of the PEA test cell ground connection on the generated piezo-sensor distortion. In Section 5.2.2.3, the influence of the selected connection of the ICP terminal and the OCP terminal (see Figure 28) on the results in Sections 5.2.2.1 and 5.2.2.2 is discussed.

In the cases denoted with an "f" at the end of the case name, the pulse terminal ICP is connected to the PEA test cell and the OCP is connected to the external shield of the HVDC cable. The cases with the inverse arrangement are denoted using "r" at the end of the case name. In these cases, the OCP is connected to the PEA test cell and the ICP is connected to the external shield of the HVDC cable.

The tests were performed using the PEA test cell on the HVDC cable described in Section 4.3. This cable has been previously subjected to tests non-related to this work, in which HVDC has been applied. Due to this, the cable has pre-existing space charges which can be observed in the subsequent results. Nevertheless, the existence of space charges does not affect the results of this work. The measurements were performed at ambient temperature without applying DC to the HVDC cable and without a temperature gradient present. For each test, the duration of the measurements was less than 1 min.

The applied voltage at the pulse circuit was 5.5 kV, which as described in section 4.2, will propagate trough 100 meters of 50 Ω transmission cable before reaching the PEA test cell, where it is partially reflected due to the mismatching impedances resulting in a higher applied pulsed voltage at the setup.

In Figure 37, the measured voltage at the voltage divider of the pulse generator can be observed (see Figure 28), where the initial peak belongs to the outgoing pulse of the generator and the reflected voltage waveform from the test cell arrives at 1 µs. Because the pulsed voltage at the test cell is the overlapping of the incident and reflected waves, it is possible to estimate the applied pulsed voltage by adding these two pulses. In Figure 4b, one can appreciate some oscillations at the reflected signal (after 1 µs) due to the interaction of the grounded PEA test table.

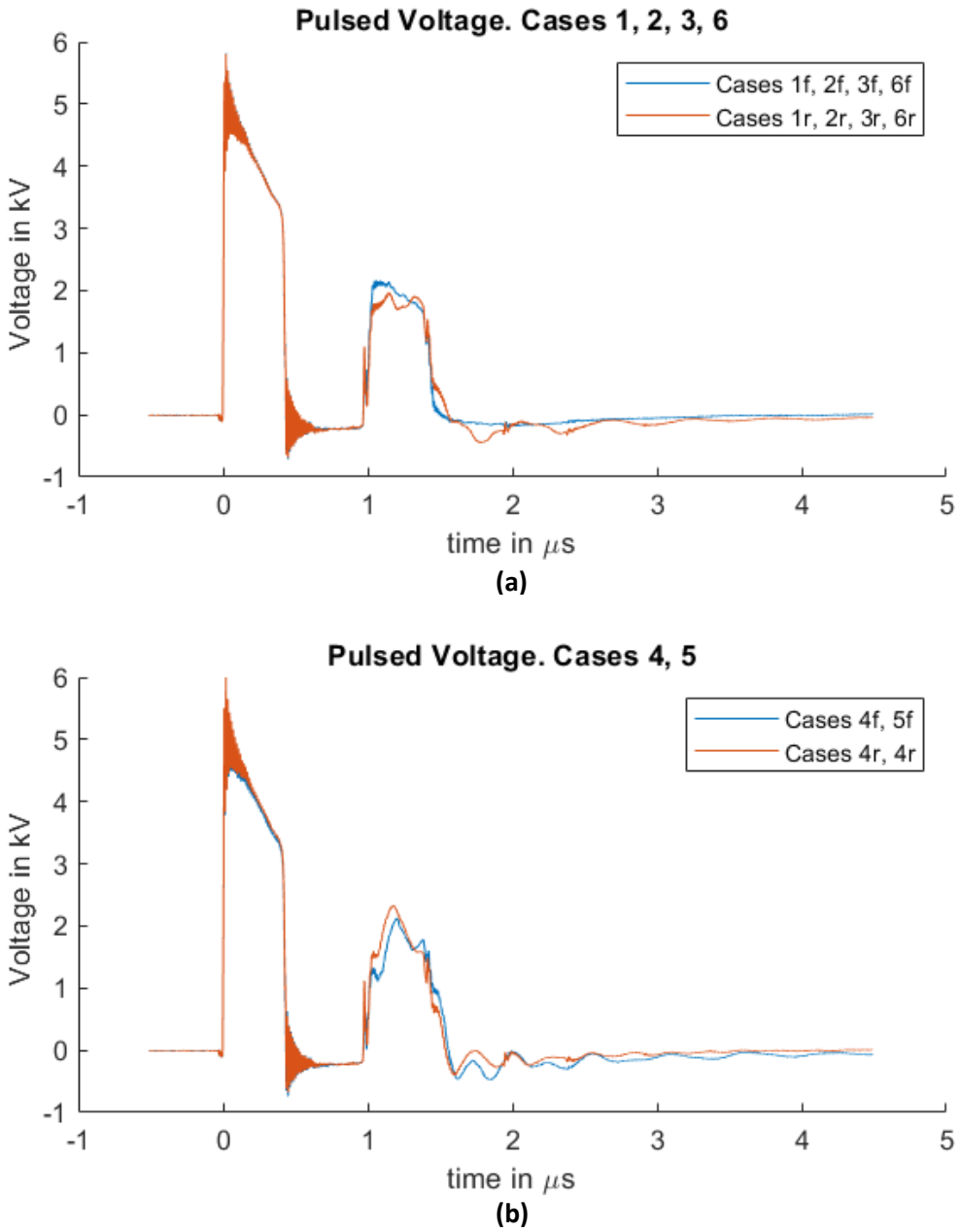

Figure 37. The measured voltage at the voltage pulse generator. The signal from 0 to 0.3 µs belongs to the outgoing pulse; the signal after 0.8 µs is the reflected voltage at the HVDC connection. (a) Measured voltage for cases 1, 2, 3 and 6. (b) Measured voltage for cases 4 and 5.

Regarding the sensitivity of the system, Figure 38 shows the measured signals with different applied DC voltages, which can be used as a reference for the sensitivity of the measuring system. The duration of the applied DC for each HVDC value was 30 s. The measured signal in the case of no voltage applied is attributed to pre-existing charges from previous HVDC with temperature tests, non-related to this work.

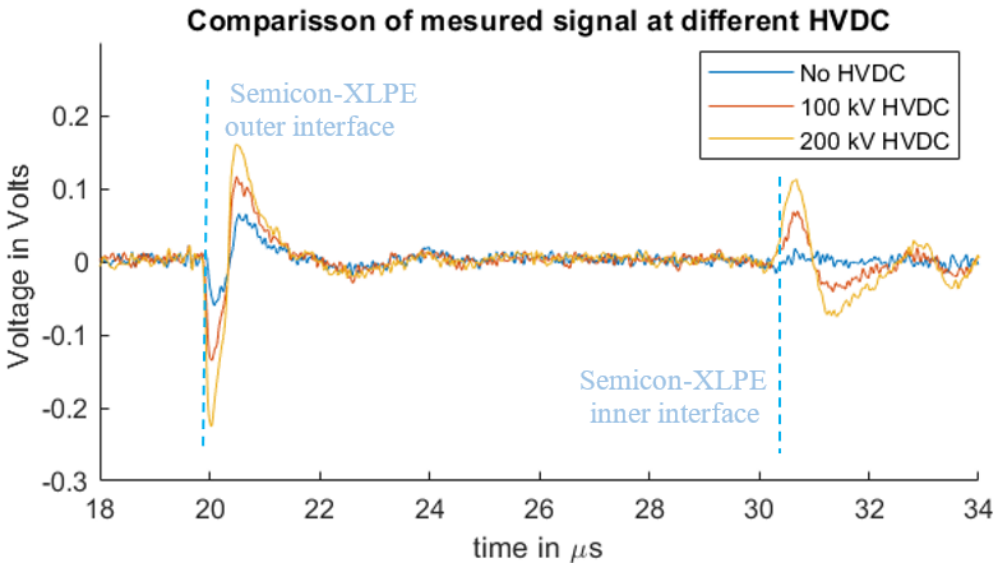

Figure 38. Measured signals with different applied HVDC magnitudes and a 5.5 kV pulsed voltage at the voltage pulse generator.

5.2.2.1. Influence of the Pulsed Voltage Connection

In this section, Cases 1f, 1r, 2f, 2r, 3f and 3r were compared to observe the influence that the physical location of the terminal connection of the pulsed voltage at the PEA test cell has on the piezo sensor distortion. In this section it is described the setup configurations used for these tests followed by its results and discussion.

Influence of the Pulsed Voltage Connection Test Configurations

For these tests, three different connection locations for the pulsed voltage at the PEA test cell were compared. Figure 39 illustrates the selected locations for the comparison used for Cases 1f, 1r, 2f, 2r, 3f and 3r. In these cases, there is a dielectric table between the metallic table and the PEA test cell to decrease the parasitic capacitance towards the ground.

- Cases 1f and 1r: Pulse injection between the base of the PEA test cell and the HVDC cable shield. The test cell is ungrounded. The HVDC cable shield is grounded.

- Cases 2f and 2r: Pulse injection between the lateral part of the PEA test, close to the upper surface of the aluminum electrode, and the HVDC cable shield. The test cell is ungrounded. The HVDC cable shield is grounded.

- Cases 3f and 3r: Pulse injection between the clamping screws of the HVDC cable to the test cell and the HVDC cable shield. The test cell is ungrounded. The HVDC cable shield is grounded.

An overview of the cases can be seen in Table 9.

Table 9. Influence of the pulsed voltage connection test configurations.

Case	Pulsed Voltage Configuration		Test Cell
	ICP Connected to	OCP Connected to	
Case 1f	Test cell at point "a"	HVDC Cable shield	Ungrounded
Case 2f	Test cell at point "b"	HVDC Cable shield	Ungrounded
Case 3f	Test cell at point "c"	HVDC Cable shield	Ungrounded
Case 1r	HVDC Cable shield	Test cell at point "a"	Ungrounded
Case 2r	HVDC Cable shield	Test cell at point "b"	Ungrounded
Case 3r	HVDC Cable shield	Test cell at point "c"	Ungrounded

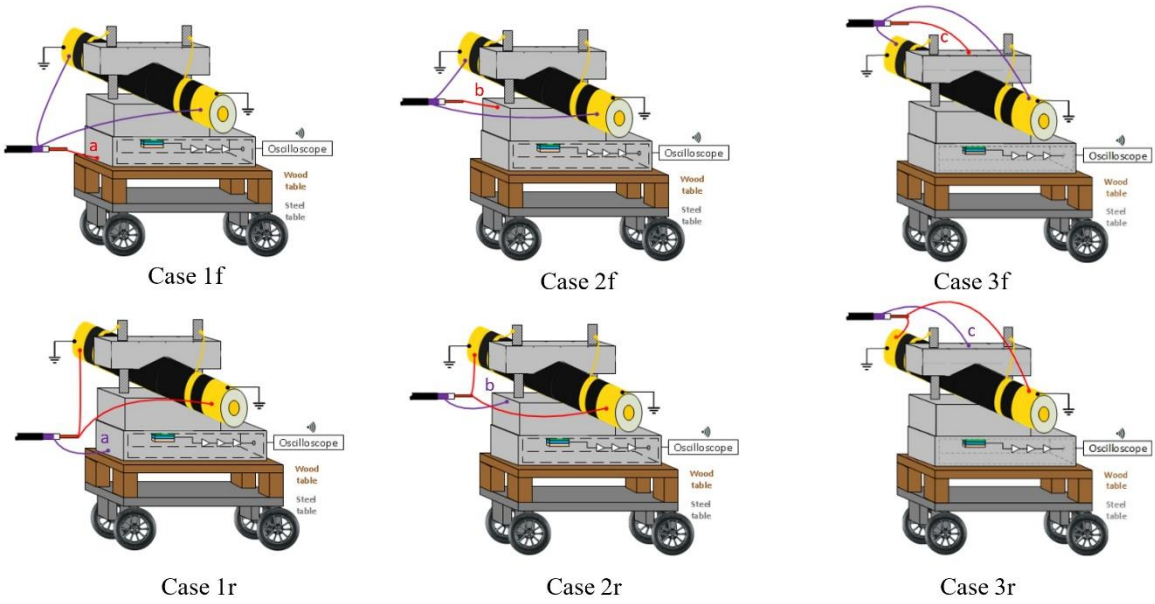

Figure 39. A 3D representation of the pulsed voltage connection locations for Cases 1f, 1r, 2f, 2r, 3f and 3r. Each of these cases has a different current distribution across the PEA test cell with a different impact in the piezo amplifier interference. The connection between the test cell and the guard is done through the yellow cables at the mechanical pressure screws.

Influence of the Pulsed Voltage Connection Results and Discussion

In Figure 40 and Figure 41, it is possible to observe the cases for different disturbances at the measured signals due to the connection configuration of the pulsed voltage at the PEA test cell. Figure 40 represents the measurements of Cases 1f, 2f and 3f. Figure 41 shows the results for Cases 1r, 2r and 3r, which are the inverse pulse connections.

It should be noted that the measured disturbance at the beginning of the signals (less than 1 µs) has a magnitude higher than 1 V, meaning that the amplifier saturated, and that the full magnitude of the waveform cannot be observed. The main objective of this work is to compare how the disturbance reaches and overlaps with the acoustic signal belonging to the space charges region. For this purpose, the focus is on the 19 µs time delay region.

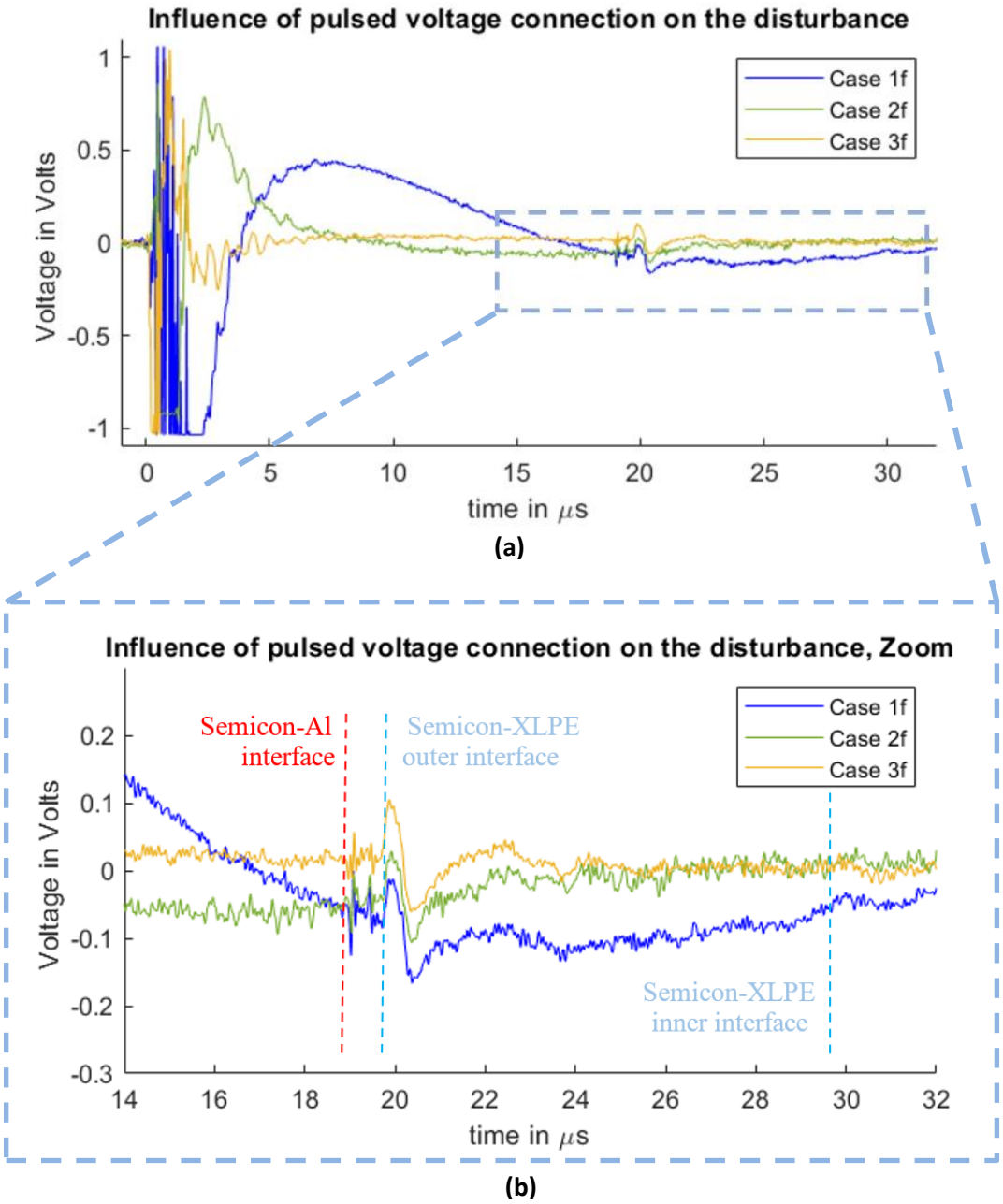

Figure 40. Measured disturbance from Cases 1f, 2f and 3f. (a) Full measured signal ranging from the instant of the pulsed voltage application up to 32 µs. (b) Zoom to the time instant of the acoustic signal arrival belonging to the charge measurements.

From the measurements, one can observe the existence of space charges at the dielectric. This generates the mirror charges at the dielectric–semiconductor interfaces of the internal and external electrodes around 20 and 30 µs. The measured signal does not represent the real space charge distribution, as the signal still needs to go through post-processing to compensate for the piezo-amplifier response, geometric divergence and acoustic attenuation losses [23–25,50,58,73–75].

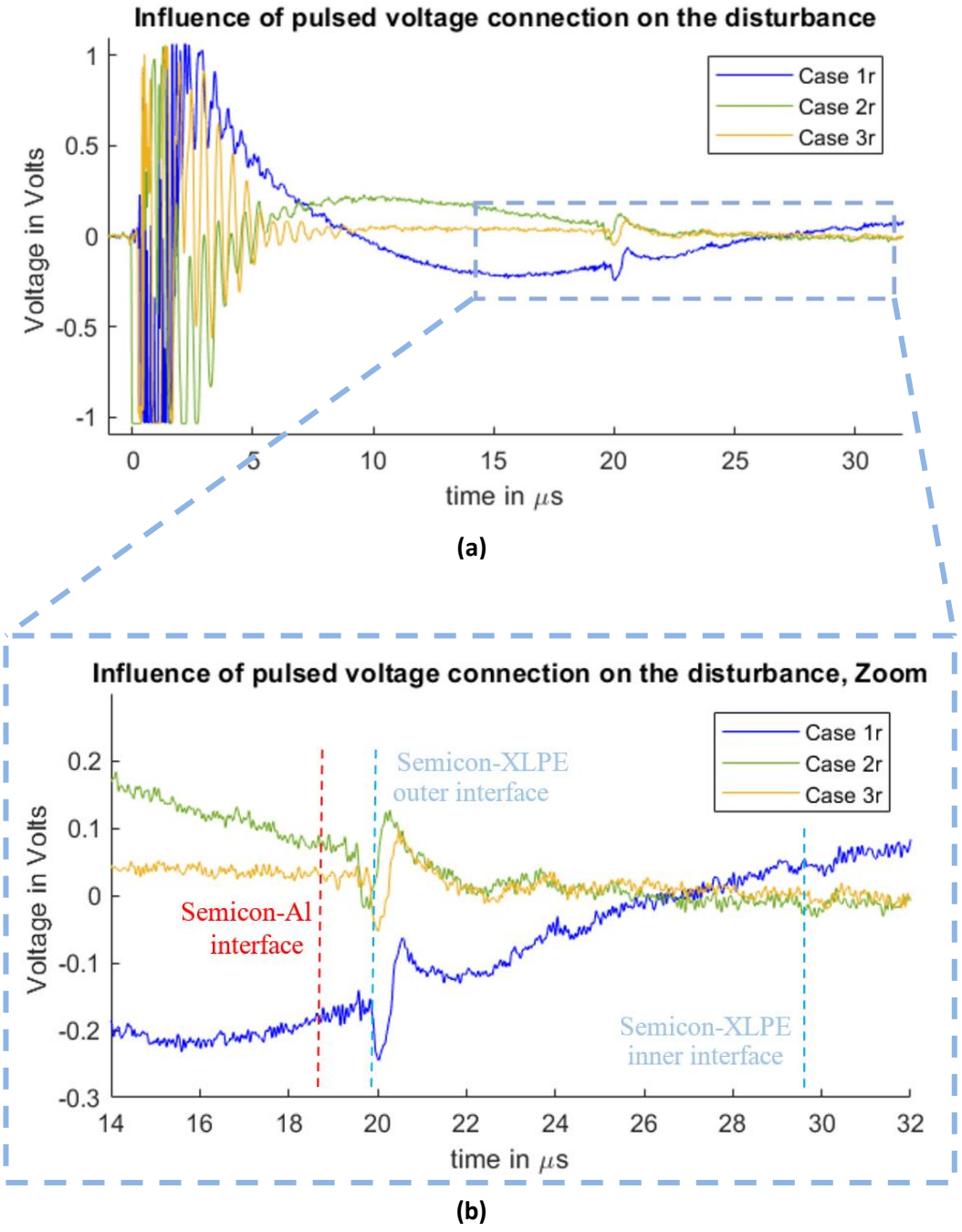

Figure 41. Measured disturbance from Cases 12, 2r and 3r. (a) Full measured signal ranging from the instant of the pulsed voltage application up to 32 µs. (b) Zoom to the time instant of the acoustic signal arrival belonging to the charge measurements.

The spike signal that can be seen at 19 µs is generated at the vicinity of the semiconductor–aluminum interface, which is attributed to the stray capacitance between the semiconductor and the aluminum [68]. This spike was reduced for Cases 1r, 2r and 3r.

From Figure 40 and Figure 41, one can observe how the pulsed voltage injection location has a different impact on the disturbance of the signal depending on the pulse current path across the PEA test cell. When the pulse injection occurs through the base of the PEA test cell (Cases 1f and 1r), the pulse current path is closer to the amplifier, which creates a higher electromagnetic interference in comparison to Cases 2f, 2r, 3f and 3r. Between Cases 2f and 3r, as well as between 2r and 3f, the difference is not as remarkable. Nevertheless, in Figure 40b and Figure 41b, one can observe how, at the arrival time of the acoustic wave from the HVDC cable, the signal in Cases 2f and 2r is still more affected by the disturbance, adding error to the measurement.

One can notice that in the measurements the disturbance reaches the relevant acoustic measurement after the delay of the aluminum electrode, Cases 1f and 1r being the worst situation.

5.2.2.2. Influence of the PEA Test Cell Grounding

In this section, Cases 4f, 4r, 5f, 5r, 6f and 6r were compared to observe the influence of the PEA test cell grounding on the piezo sensor distortion. This section describes the setup configurations used for these tests, followed by its results and discussion.

Influence of the PEA Test Cell Grounding Test Configurations

For these tests, three different grounding configurations were measured and compared, using Cases 3f and 3r from the previous section as reference. In Cases 6f and 6r, a PEA test cell bottom surface of 230 × 330 mm^2 is separated from a grounded surface by 20 mm of pressboard. This allows us to observe the impact on the distortion in the case of an increased parasitic capacitance towards the ground when the PEA test cell is ungrounded.

Figure 42 illustrates Cases 4f, 4r, 5f, 5r, 6f and 6r used to test the grounding effect of the test cell. In Cases 4f, 4r, 5f and 5r, the PEA test cell was grounded, each at a different location, while keeping the HVDC cable shield ungrounded. These ground connections do not represent a short circuit for the pulse circuit, as it is decoupled from the ground due to the length of the transmission line, as mentioned in Section 3.3. In Cases 4f, 4r, 5f, 5r, 6f and 6r,

the location of the pulsed voltage connection at the PEA test cell is between the clamping screws of the HVDC cable (as for Cases 3f and 3r).

The cases for this test are the following:

- Cases 4f and 4r: The PEA test cell is grounded at the lower point of the aluminum block electrode. Pulse injection between the clamping screws of the HVDC cable to the test cell and the HVDC cable shield. The HVDC cable shield is ungrounded except for the pulsed voltage connection.

- Case 5f and 5r: The PEA test cell is grounded at the upper surface of the aluminum block electrode. Pulse injection between the clamping screws of the HVDC cable to the test cell and the HVDC cable shield. The HVDC cable shield is ungrounded except for the pulsed voltage connection.

- Case 6f and 6r: The test cell is ungrounded, but the extra dielectric table has been removed to increase the parasitic capacitance. Pulse injection between the clamping screws of the HVDC cable to the test cell and the HVDC cable shield. The HVDC cable shield is grounded.

For all the cases, the connection of the PEA test setup to ground was done utilizing the same earth point and using a conductor of around 3 meters in length. An overview of the cases can be seen in Table 10.

Table 10 Influence of PEA test cell grounding configurations.

Case	Pulsed Voltage Configuration		Test Cell
	ICP Connected to	OCP Connected to	
Case 4f	Test cell at point "c"	HVDC Cable shield	Grounded at "a"
Case 5f	Test cell at point "c"	HVDC Cable shield	Grounded at "b"
Case 6f	Test cell at point "c"	HVDC Cable shield	Ungrounded
Case 4r	HVDC Cable shield	Test cell at point "c"	Grounded at "a"
Case 5r	HVDC Cable shield	Test cell at point "c"	Grounded at "b"
Case 6r	HVDC Cable shield	Test cell at point "c"	Ungrounded

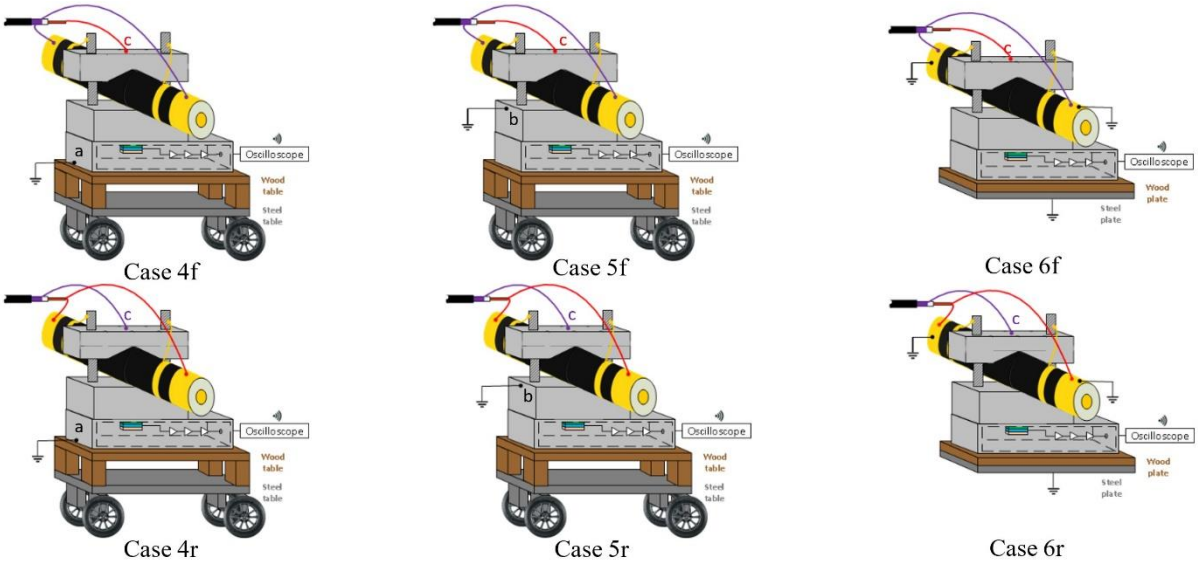

Figure 42 A 3D representation of the pulsed voltage connection locations for Cases 4f, 4r, 5f, 5r, 6f and 6r. Each of these cases has a different current distribution across the PEA test cell, with a different impact on the piezo amplifier interference. The connection between the test cell and the guard is done through the yellow cables at the mechanical pressure screws.

Influence of the PEA Test Cell Grounding Results and Discussion

In Figure 43 and Figure 44, we can observe the measured signals from the cases 3f, 3r, 4f, 4r, 5f, 5r, 6f and 6r. Each case represents a different interaction between the PEA test cell and the ground, having an influence on the disturbance waveform at the piezo sensor.

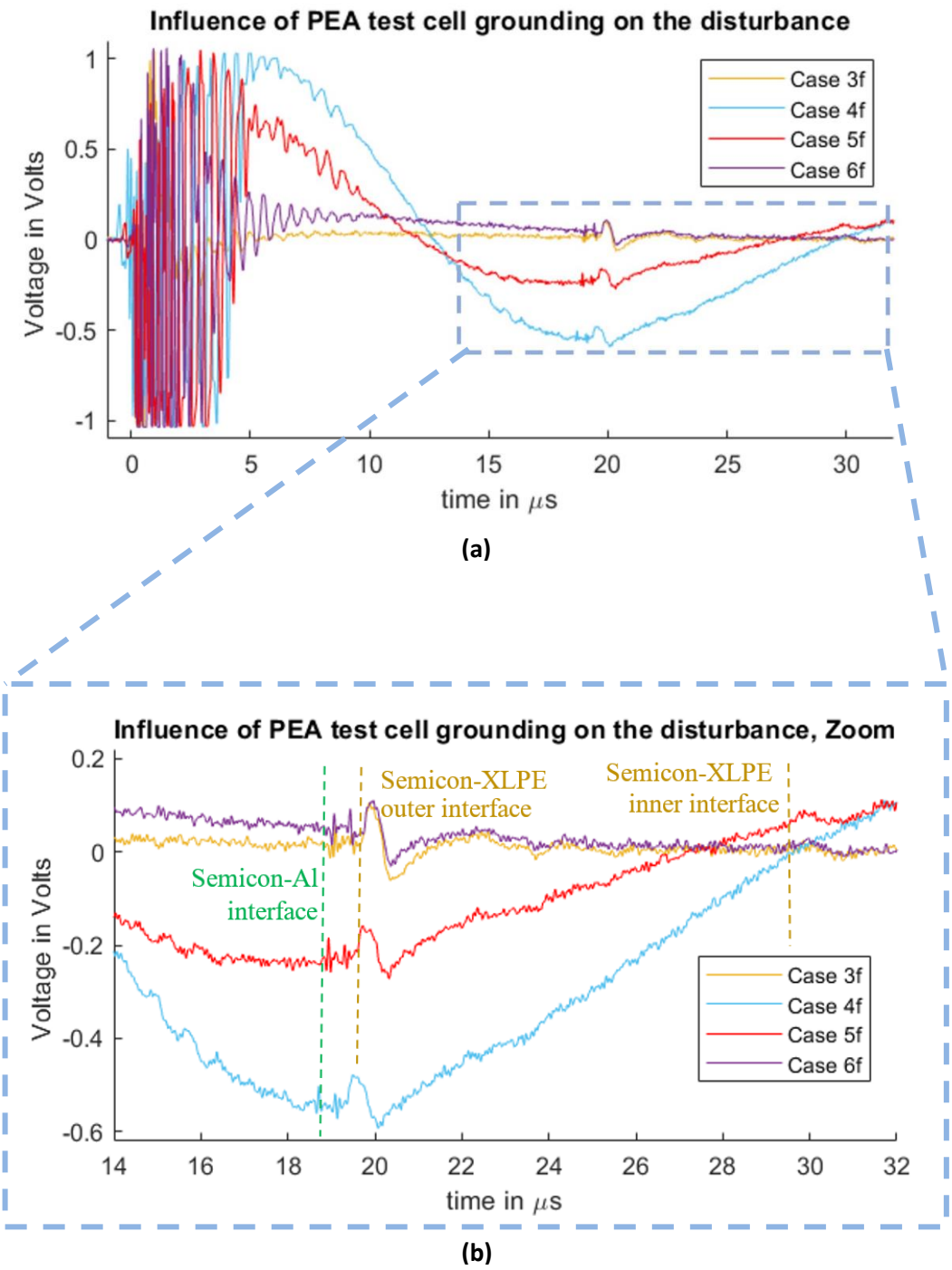

Figure 43. Measured disturbance from Cases 3f, 4f 5f and 6f. (a) Full measured signal ranging from the instant of the pulsed voltage application up to 32 µs. (b) Zoom to the time instant of the acoustic signal arrival belonging to the charge measurements.

As in the previous section, the spike signal observed at 19 µs is related to the semiconductor–aluminum interface, and its effect is reduced when the pulse injection is done via the HVDC cable shield.

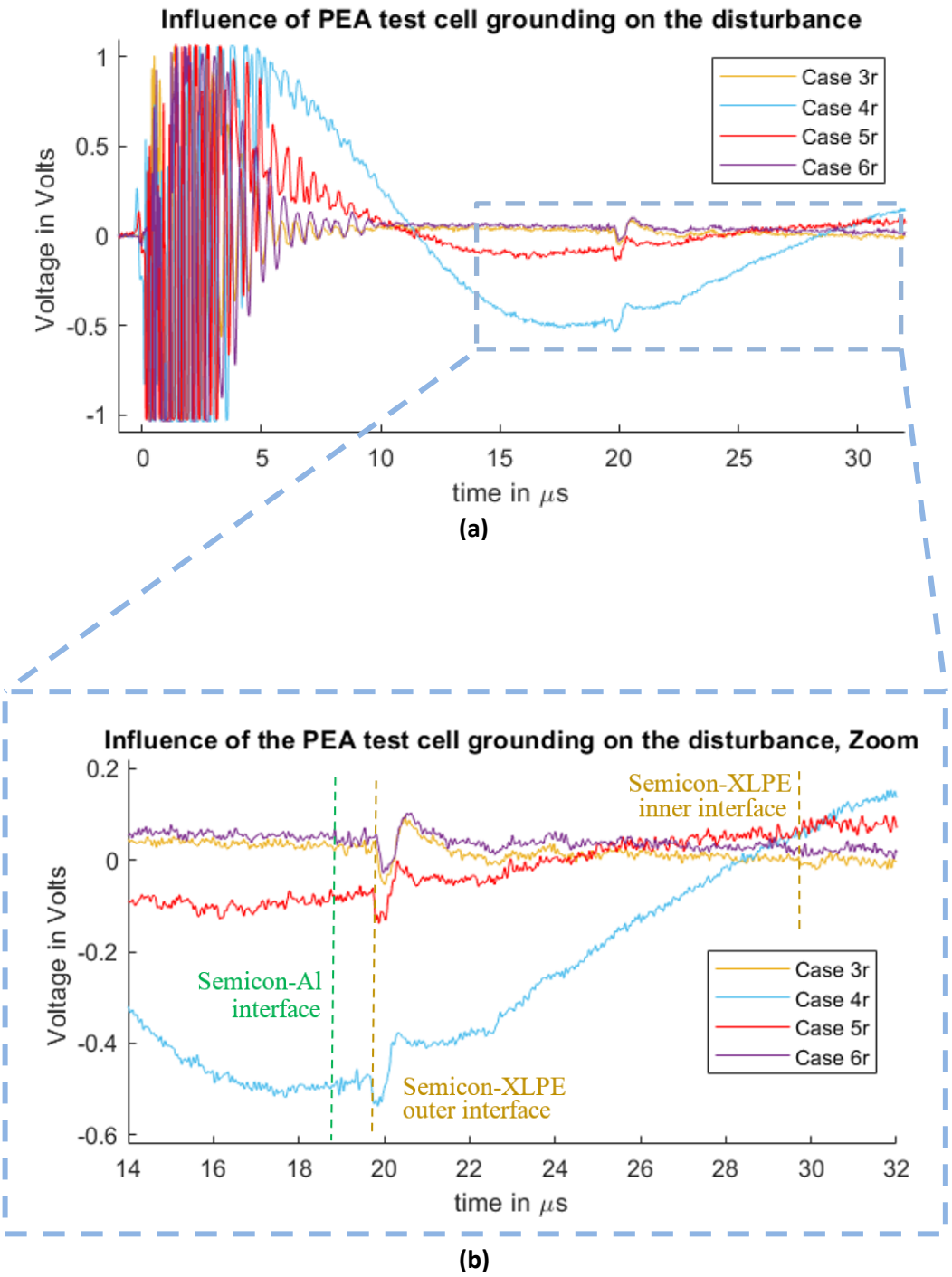

Figure 44. Measured disturbance from cases 3r, 4r, 5r and 6r. (a) Full measured signal ranging from the instant of the pulsed voltage application up to 32 µs. (b) Zoom to the time instant of the acoustic signal arrival belonging to the charge measurements.

In Cases 3f, 3r, 6f and 6r, where the test cell is electrically isolated from the ground except from the pulsed voltage transmission cable, less distortion is present when compared to Cases 4f, 4r, 5f and 5r. This can be attributed to the extra currents at the test cell towards the ground connection, for which, in the cases 5f and 5r, the ground path is closer to the sensor.

Between Cases 3f, 3r, 6f and 6r, the difference is the higher parasitic capacitance for Cases 6f and 6r. One can observe than, in Figure 43, Case 6f is more distorted than Case 6r in Figure 44. This is attributed to the connection of the ICP terminal to the PEA test cell, where the test cell acquires a higher voltage relative to ground during the pulse injection in comparison to the connection of the ICP terminal to the HVDC cable shield. In Figure 43b, we can observe that the difference between Case 3f and Case 6f is still visible, even after the acoustic delay. This exemplifies the relevance of the ground for the measurement setup, as the parasitic capacitance has an impact on the overall disturbance.

5.2.2.3. Pulse Voltage Cable Connection influence

In Figure 40 to Figure 44, the impact of the connection of the ICP and OCP to either the PEA test cell or the HVDC cable shield can be observed. Regarding the acoustic signal, the polarity is inverted, which is expected as the applied transient electric field is inverted in each configuration. Case 3 was shown to be the best result for each of the scenarios regarding the distortion. In this case, the choice of the reference (OCP) and positive (ICP) electrode does not appear to have a big impact on the quality of the signal, even since the shield of the HVDC cable is solidly grounded for all cases except 4f, 4r, 5f and 5r. This can be attributed to the fact that the current components of the pulse at the HVDC cable shield towards the grounding do not affect the current distribution across the PEA test cell to the same extent than in the other configurations.

5.3. Electromagnetic Distortion Reduction by Impedance Grounding and Pulsed Voltage Electrode Configurations

As described in Section 5.2, the distortion due to the crosstalk is influenced by the grounding of the PEA test cell, where the induced distortion in the measurement can be reduced by increasing the impedance to ground. Nevertheless, this is not always feasible, as there are cases where the grounding of the test cell might be needed, such as in the case of having a continuous measurement during long periods of cable testing which might require the powering of the PEA test cell devices during several days.

In this section it is analysed the influence of two factors at the crosstalk distortion specifically when the PEA test cell is grounded. The two analysed factors are: First, the influence of the exposed semiconductor distance between the injection electrodes and the PEA test cell. Second, the influence of adding a reactance at the grounding circuit of the PEA test cell. For the last case, the reactance at the grounding circuit is achieved by the addition of N30 ferrites at the grounding line of the PEA test cell

Moreover, both factors were also tested using an alternative developed coaxial configuration for the injection of the pulsed voltage to analyse its impact at the reduction of the crosstalk by means of a coaxial injection.

5.3.1. Experimental setup

For the test experiments, just as in section 5.2, it was utilized the PEA setup and the HVDC cable sample described in Section 4.

In this case, for the base electrode, the configuration B of 40 mm thickness from Table 6 was utilized. In this configuration, the acoustic delay by the base electrode is decreased by a factor of 3 compared to the 120 mm base electrode thickness, meaning that the overlapping of the useful acoustic signal with the crosstalk distortion signal occurs at a shorter time. Using the 40 mm base electrode, it was not noticed an impact at the measurement due to the shear waves that propagate approximately half the speed of the longitudinal waves, and it reduces the overall weight of the test cell.

For the test experiments of section 5.3, the total applied amplification to the signal of the piezo film is 50 dB. The purpose of utilizing this amplification was to allow the measurement of the full magnitude of the distortion signal at the instant of applying the pulsed voltage, without saturating the amplifiers nor the oscilloscope. A graphic description of the setup can be seen in Figure 45.

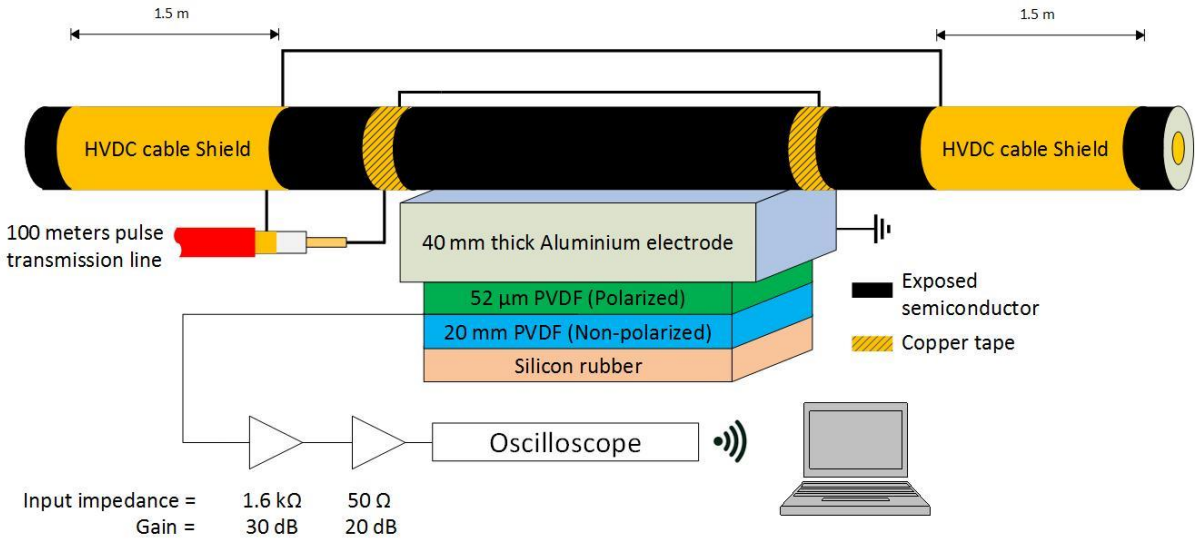

Figure 45. Representation of the PEA test cell for section 5.3 including the acoustic sensor, amplifier and oscilloscope.

The sets of experiments were performed in two different pulsed voltage injection configurations to observe the difference between a coaxial and a noncoaxial structure in relation to the crosstalk at the piezo amplifier at the instant of the pulsed voltage injection.

5.3.1.1. Non-Coaxial Pulsed Voltage Injection

The non-coaxial configuration for the pulsed voltage involves the connection between the HVDC cable shield and the guard electrodes. The guard electrodes are situated at each side of the PEA test cell, and its distance towards the test cell will be varied between experiments from 0 cm to 27 cm, depending on the test. The connection is done through a single conductor as can be seen in Figure 46. In the figure we can observe the variable "d" which stands for the distance between the injection electrode and the PEA test cell, and the inductance "L" due to the application of N30 ferrites at the PEA test cell grounding.

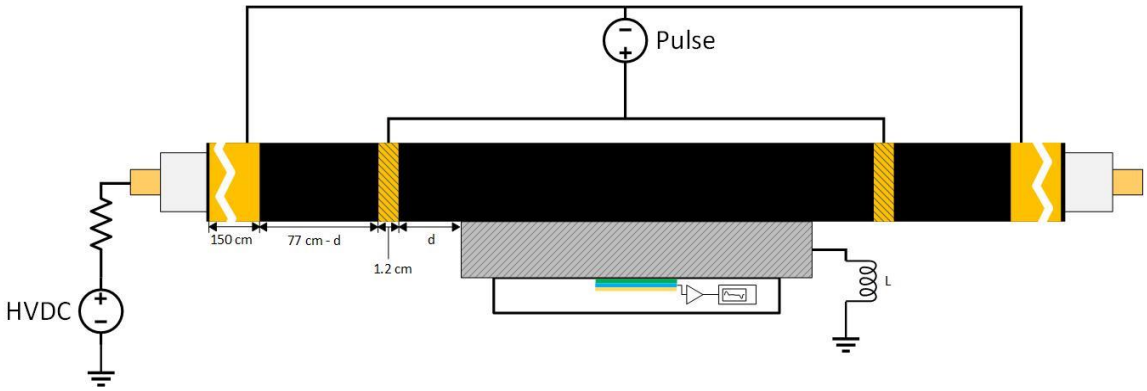

Figure 46. Application of the pulsed voltage at the HVDC test cable using the non-coaxial configuration. "d" stands for the distance between the injection electrode and the PEA test cell, "L" is the applied inductance at the PEA test cell grounding.

5.3.1.2. Coaxial Pulsed Voltage Injection

The coaxial injection consists of an array of 40-line conductors arranged in parallel around the HVDC cable test sample. In this way, the array of cables in parallel around the HVDC cable are utilized as the return conductor, while the HVDC cable (semiconductor and internal conductor) acts as the internal conductor of the coaxial structure of the pulsed voltage injection. It is important to mention that the coaxial injection is directly connected to the coaxial transmission cable of 50 Ω coming from the pulse generator to the PEA test cell, meaning that a coaxial structure is kept in the whole pulse circuit. The schematic of the injection can be appreciated in Figure 4. Just as with the non-coaxial injection, we can observe the variable "d" which stands for the distance between the injection electrode and the PEA test cell, and the inductance "L" due to the application of N30 ferrites at the PEA test cell grounding.

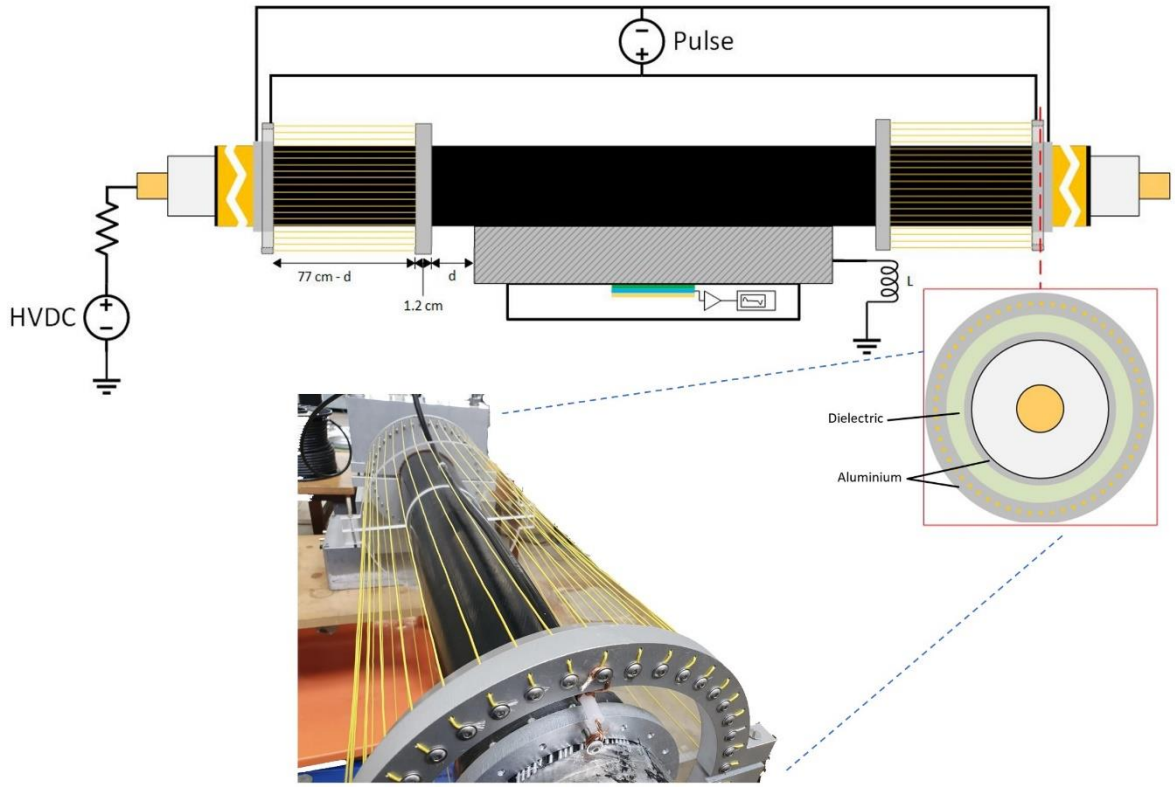

Figure 47. Application of the pulsed voltage at the HVDC test cable using the coaxial configuration. "d" stands for the distance between the injection electrode and the PEA test cell, "L" is the applied inductance at the PEA test cell grounding.

5.3.2. Test Experiments

The sets of experiments for the influence of the exposed semiconductor distance between the injection electrodes and the PEA test cell, and the influence of adding a reactance at the grounding circuit of the PEA test cell were performed in two different pulsed voltage injection configurations to observe the difference between a coaxial and a noncoaxial structure in relation to the crosstalk at the piezo amplifier at the instant of the pulsed voltage injection.

A PEA measurement was performed applying 150 kV at the test sample to be used as a reference for the sensitivity of the utilized measuring system configuration, as can be observed in Figure 48. This measurement was performed utilizing the non-coaxial injection structure with $d = 0$ cm distance between the guard electrode and the PEA test cell and no use of ferrites (which are described in section 5.3.2.1). The distortion was eliminated in post-processing by means of subtracting a measured signal with no HVDC applied (while this subtraction procedure can be utilized to observe the interface charges due to the HVDC, the

signal of the pre-existing charges is also eliminated and cannot be analysed in this way, as previously described in section 5.1). For the rest of the experiments in section 5.3.2.1 and 5.3.2.2, no DC voltage was applied to the HVDC cable, but the existing space charges from previously HV tests can still be observed.

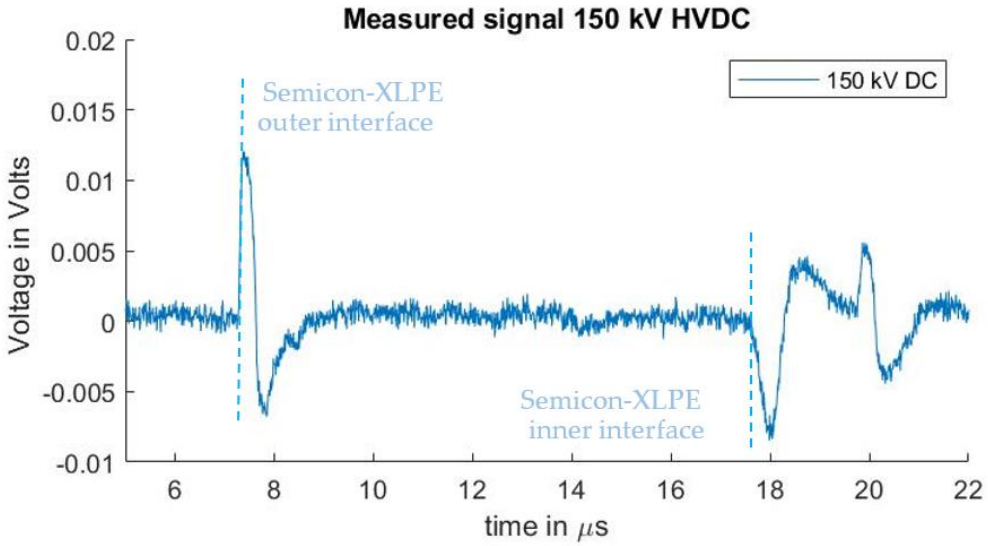

Figure 48 Measured signal with 150 kV HVDC without the distortion by means of subtracting a measure signal with no HVDC applied.

5.3.2.1. Non-Coaxial Injection Results and Discussion

In these tests, the non-coaxial injection was used. The following described test cases were performed to observe the influence of the crosstalk between the pulsed voltage and the piezo sensor by varying two parameters:

- The first parameter is the impedance between the electrode guards and the PEA test cell by increasing the semiconductor distance between them.

- The second parameter is the addition of an impedance for high frequencies at the grounding line of the PEA test cell by means of adding N30 ferrites each with an equivalent inductance of 8.7 µH per squared turn. In this work, it was utilized just one turn per ferrite.

A summary of the test cases whose results are shown in this work can be seen in Table 11, where "$\boldsymbol{d}$" stands for semiconductor separation between the PEA test cell and the guard electrodes, and "$\boldsymbol{L}$" is the total inductance of the added N30 ferrites.

Table 11. Non-coaxial injection test cases

Case	Added ground inductance L	Semiconductor distance d
Case Nn0d0	0	0 cm
Case Nn0d9	0	9 cm
Case Nn0d18	0	18 cm
Case Nn0d27	0	27 cm
Case Nn4d0	34.8 μH (4 N30 ferrites)	0 cm
Case Nn8d0	69.6 μH (8 N30 ferrites)	0 cm
Case Nn8d18	69.6 μH (8 N30 ferrites)	18 cm

Non-coaxial injection at different semiconductor distances

Figure 49 depicts the measured signals from the cases Nn0d0, Nn0d9, Nn0d18, and Nn0d27, corresponding to no added external inductance and different semiconductor distances. It can be seen the whole measured signal starting at the instant of applying the pulsed voltage at 0 μs. At 7.4 μs the first acoustic peak belonging to the outer electrode of the HVDC test cable can be observed. The acoustic peak belonging to the charges in the inner conductor of the HVDC cable is at 17.9 μs, but due to the small amount of space charges, it cannot be distinguished. The acoustic peak at 20 μs is due to the reflections at the aluminum block of the PEA test cell of the acoustic signal belonging to the outer electrode.

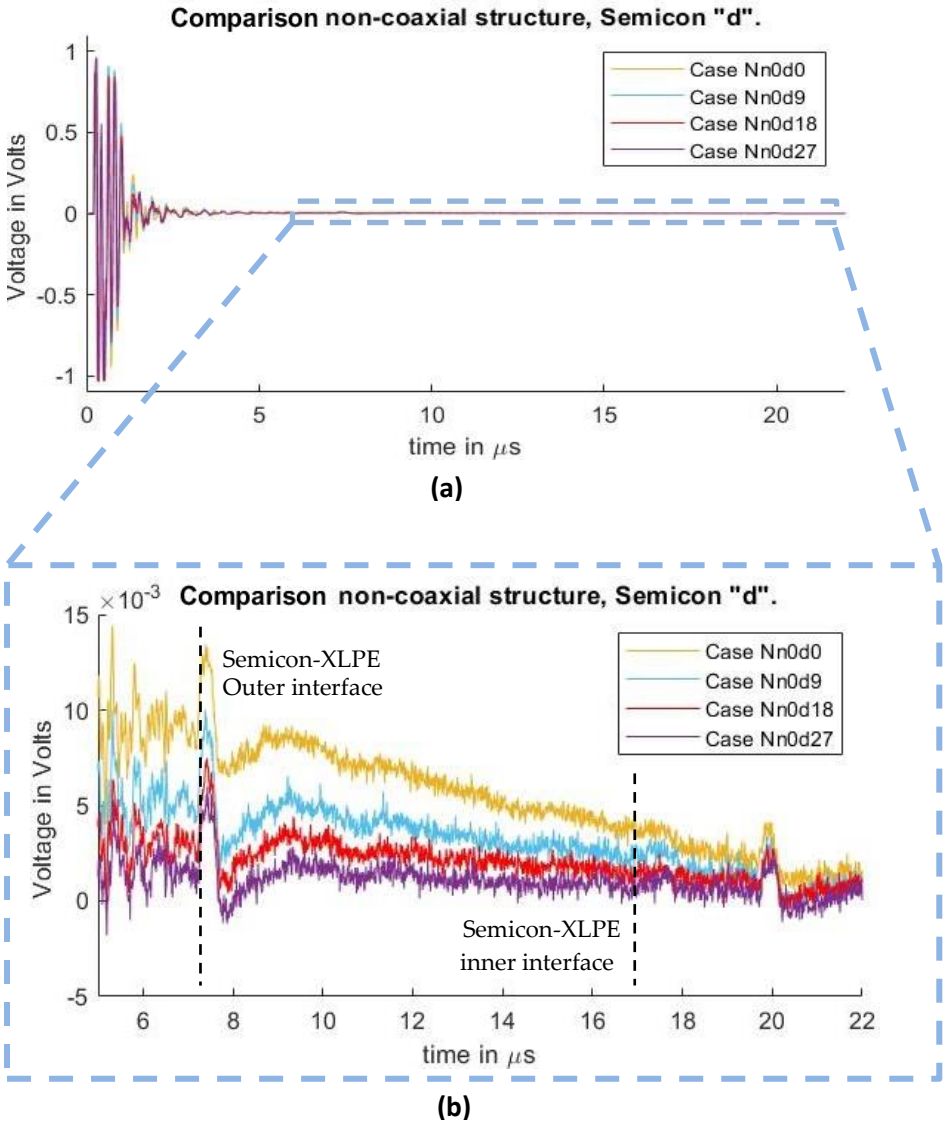

Figure 49. Measured disturbance for Cases with different distances "d" for non-coaxial injection. (a) Full measured signal ranging from the instant of the pulsed voltage application up to 22 µs. (b) Zoom to the time instant of the acoustic signal arrival belonging to the charge measurements.

In Figure 49a can be observed that due to the crosstalk between the pulsed voltage and the piezo amplifier, a distorted measured signal starting at 0 µs (instant of the applied voltage pulse) with a decaying offset, overlaps with the measured acoustic signal starting at 7.2 µs. It is also observed that the magnitude of this undesired offset is different between the different cases by increasing the semiconductor distance. The reduction of the distorted offset does not follow a linear reduction in relation with the semiconductor distance. The reduction follows an exponential decay by increasing the semiconductor distance between the guarded electrode and the PEA test cell.

To compare the acoustic magnitudes between the different semiconductor distances, a high-pass filter with a passband frequency of 500 kHz was applied to the measured signals. The result can be observed in Figure 50, with a focus on the first acoustic peak. From the figure it can be concluded that while the undesired distorted signal is reduced (Figure 49b), the magnitude of the acoustic signal does not present noticeable difference by increasing the semiconductor distance between the electrode guards and the PEA test cell. It is important to mention that the procedure of applying the high-pass filter utilized for the magnitude analysis is not a recommended practice for postprocessing elimination of the distortion offset for the actual space charge measurements, as it is possible to lose valuable data of the space charge distribution across the dielectric.

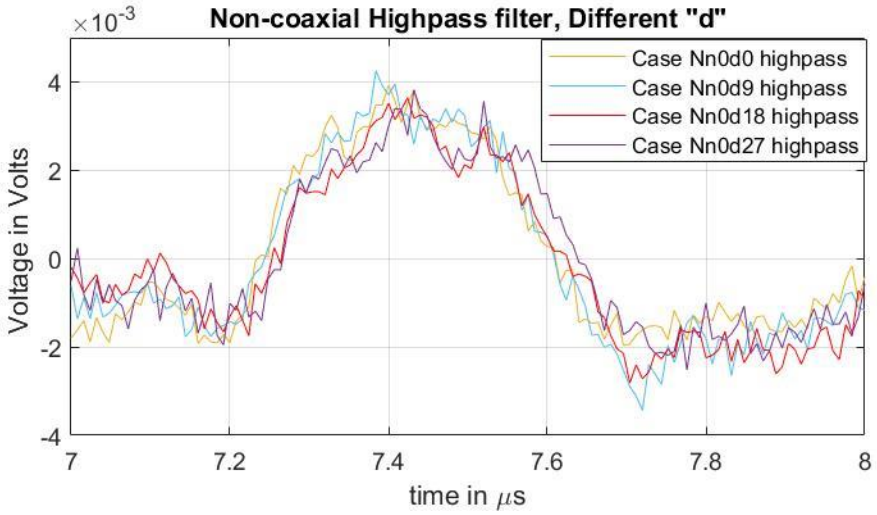

Figure 50. Acoustic magnitude comparison between the different cases of varying the distance "d" for non-coaxial injection.

Non-coaxial injection with inductive ground path

These set of tests were performed to evaluate the impact of the grounding impedance utilizing N30 ferrites, at the crosstalk distortion between the pulsed voltage and the piezo amplifier.

In Figure 51 the measured signals from cases Nn0d0, Nn4d0 and Nn8d0 can be observed. As in the test results from the previous subchapter, it can be observed the crosstalk due to the pulsed voltage and the piezo amplifier interaction, whose distorted signal overlaps with the acoustic signal starting at 7.2 μs. It can also be observed that by utilizing ferrites at the grounding conductor of the PEA test cell, this distorted signal is diminished with an exponential decay relation similar to the case of increasing the semiconductor distance "d".

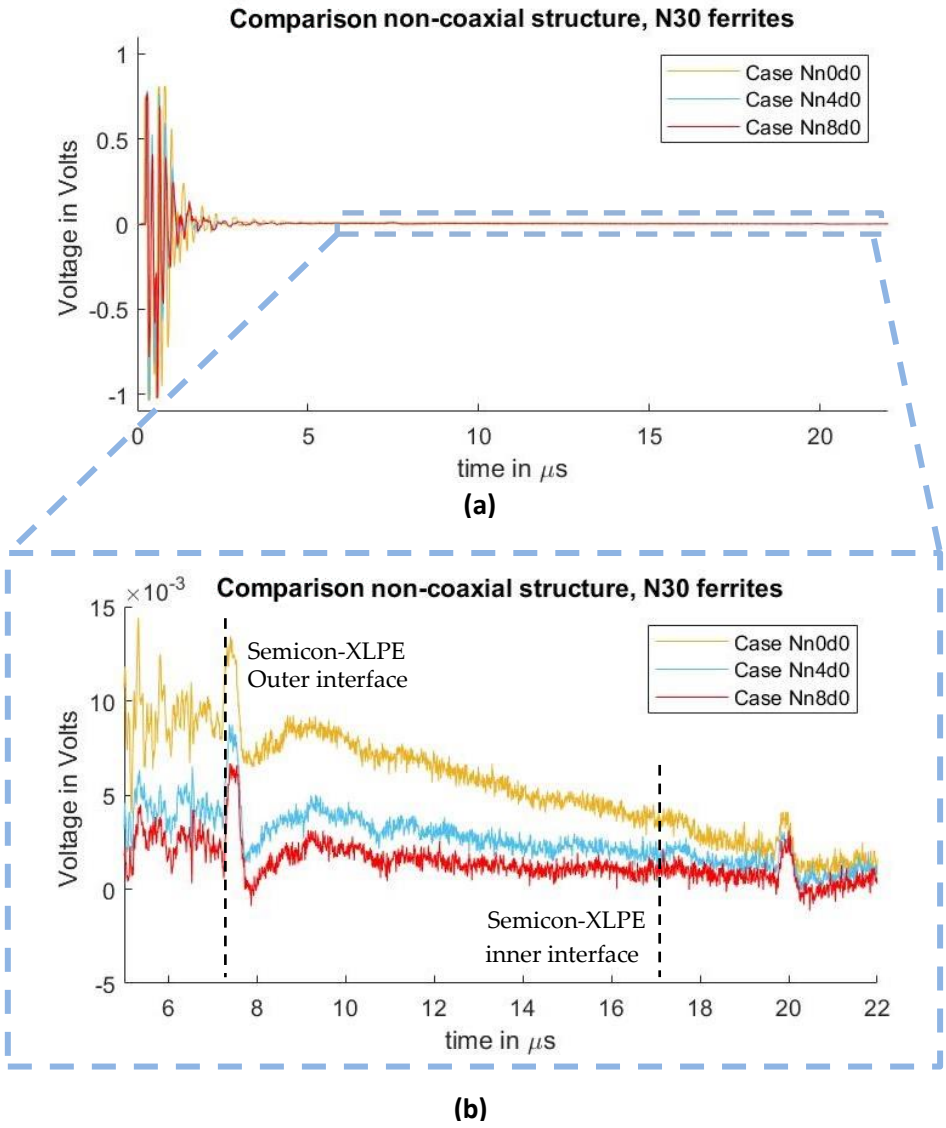

Figure 51. Measured disturbance for cases with different ground inductance "L" for non-coaxial injection. (a) Full measured signal ranging from the instant of the pulsed voltage application up to 22 µs. (b) Zoom to the time instant of the acoustic signal arrival belonging to the charge measurements.

As for the previous cases, to compare the acoustic magnitudes between different number of applied ferrites at the grounding, a high-pass filter with a passband frequency of 500 kHz was applied to the measured signals. The result can be observed in Figure 52, with a focus on the first acoustic peak. From the figure it can be noted that while the undesired distorted signal is reduced (Figure 8b), the magnitude of the acoustic signal does not present noticeable difference by adding external inductance to the ground path.

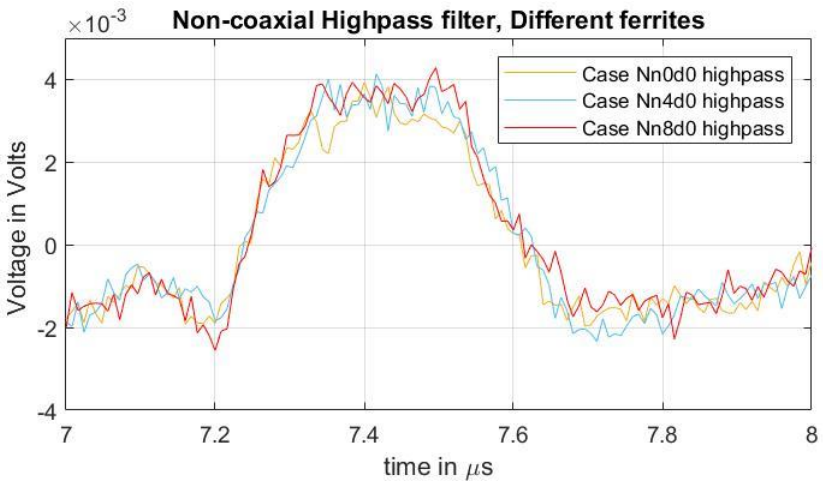

Figure 52. Acoustic magnitude comparison between the different cases of adding external inductance to the ground path.

Non-coaxial injection utilizing semiconductor distance and inductive ground path

Increasing too much either the distance between the injection electrode and the PEA test cell, or the PEA test cell grounding impedance may not always be feasible. Nevertheless, the combination of both reduction methods can be applied to further reduce the distortion. Figure 53 shows the comparison of applying an incremental number of ferrites at the PEA test cell grounding, and further reduction by combining the ferrites with the application of a distance between the guard electrode and the PEA test cell.

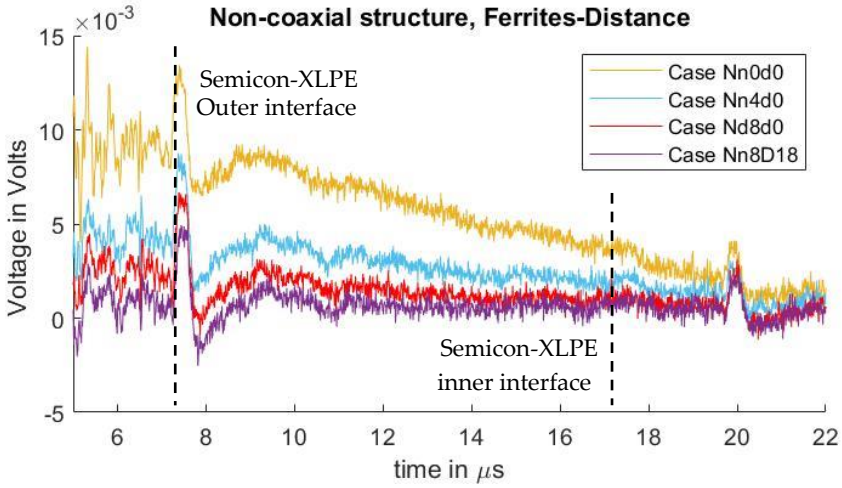

Figure 53. Comparison of measured signals with different semiconductor distance "d" combined with several ground path inductances.

5.3.2.2. Coaxial Injection Results and Discussion

In this subsection, a second set of experiments were performed to analyse the performance of the coaxial pulsed voltage injection in relation with the crosstalk distortion due to its interaction with the piezo amplifier, utilizing the coaxial structure described in section **5.3.1.2**. A similar set of tests as with the non-coaxial injection was performed utilizing the coaxial injection. The set of experiments can be seen in Table 12.

Table 12. Coaxial injection test cases

Case	Applied ground inductance L	Semiconductor distance d
Case Cn0d0	0	0 cm
Case Cn0d9	0	9 cm
Case Cn4d0	34.8 μH (4 N30 ferrites)	0 cm
Case Cn4d9	34.8 μH (4 N30 ferrites)	9 cm
Case Cn8d0	69.6 μH (8 N30 ferrites)	0 cm
Case Cn8d9	69.6 μH (8 N30 ferrites)	9 cm

Coaxial injection at different semiconductor distances

At Figure 54 it is shown the measured signals from cases Cn0d0 and Cn0d9 corresponding to no added external inductance at the grounding PEA test cell grounding circuit at different semiconductor distances d. At the measured signals, it can be observed that in relation to the induced distortion signal due to the crosstalk, the coaxial injection exhibits a similar behaviour as the non-coaxial injection. Meaning that the coaxial injection by itself does not reduce the crosstalk, and as with the non-coaxial injection, the impact of the crosstalk is reduced by incrementing the semiconductor distance d.

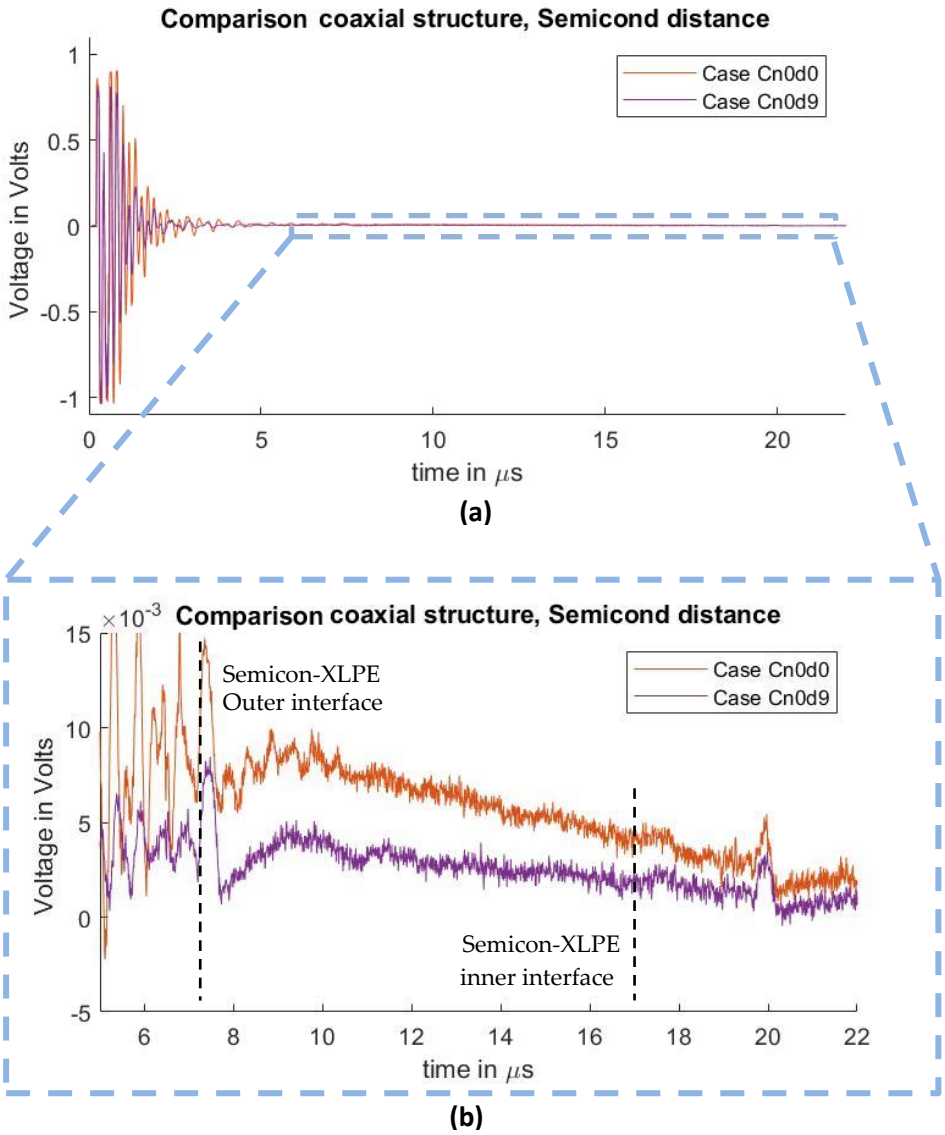

Figure 54. Measured disturbance for Cases with different distances "d" for coaxial injection. (a) Full measured signal ranging from the instant of the pulsed voltage application up to 22 µs. (b) Zoom to the time instant of the acoustic signal arrival belonging to the charge measurements.

The same behaviour can also be observed at Figure 55 where the measured signals from cases Cn0d0, Cn4d0 and Cn8d0 corresponding to the variation of the PEA test cell grounding impedance L while keeping the semiconductor distance d as zero. In the figure we can observe the same behaviour as with the non-coaxial, in which the distortion is reduced by increasing the impedance at the grounding.

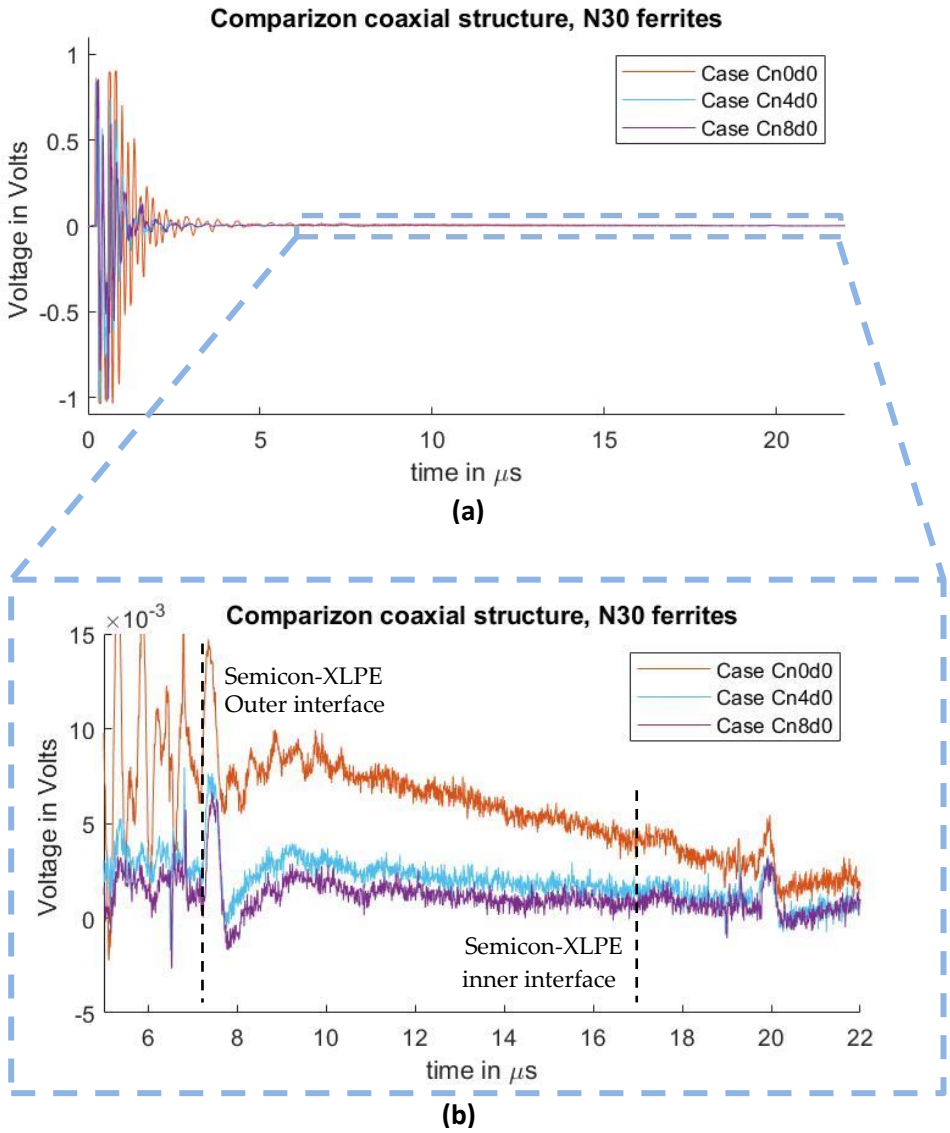

Figure 55. Measured disturbance for cases with different ground inductance "L" for coaxial injection. (a) Full measured signal ranging from the instant of the pulsed voltage application up to 22 µs. (b) Zoom to the time instant of the acoustic signal arrival belonging to the charge measurements.

Figure 56 shows a comparison between the measured signals with the non-coaxial structure and the coaxial structure. In Figure 56a, the measured signals applying eight ferrites are compared, while in Figure 56b can be seen the comparison with an applied distance "d" of 9 cm between the PEA test cell and the electrode guard (for the non-coaxial injection) or the aluminum disk (for the coaxial injection). The measurement without applied distance "d" or ferrites at the electrode guard for the coaxial and non-coaxial structure is also plotted as reference. It can be observed that there is no significant difference regarding crosstalk distortion reduction utilizing the coaxial injection.

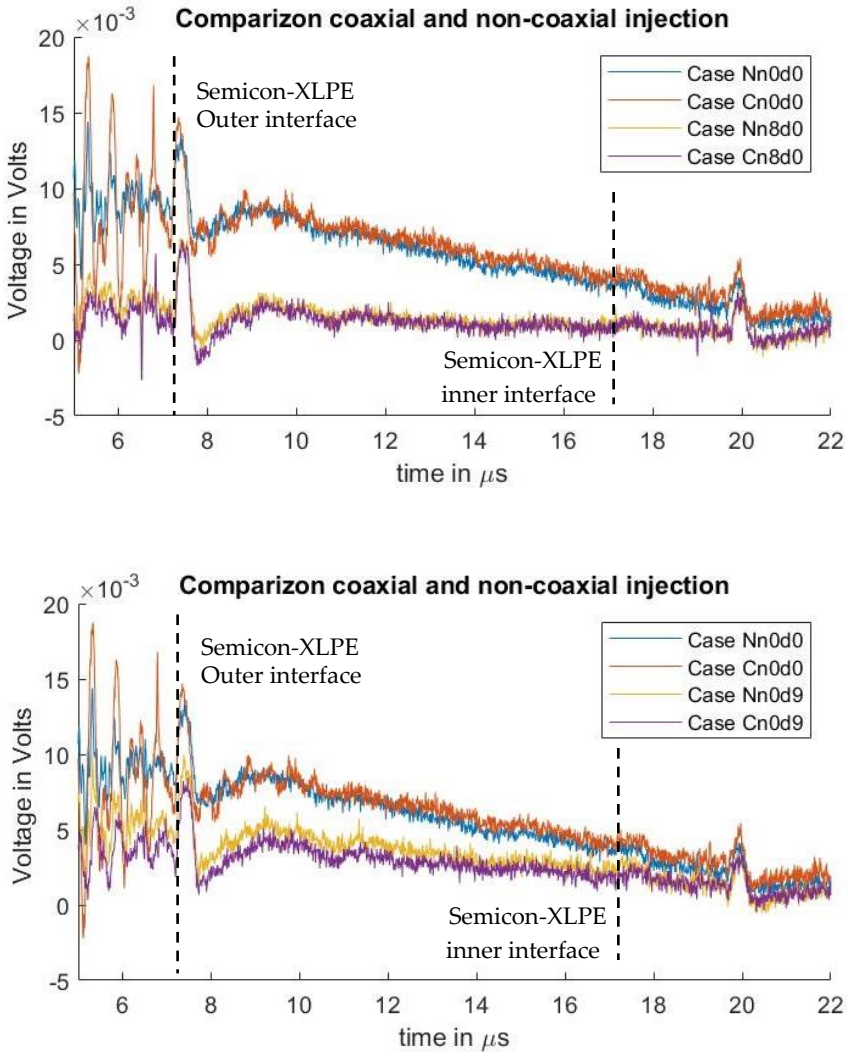

Figure 56. Comparison utilizing non-coaxial and coaxial injection regarding the distortion at the acoustic signal. (a) Comparison between 0 and 9 cm semiconductor distance "d". (b) Comparison between 0 and 69.6 µH at the PEA test cell grounding "L".

5.4. Chapter Summary

The use of a pulsed voltage in the PEA method produces an electromagnetic transient across the test cell interfering with the piezo sensor which has a decaying component that overlaps with the relevant acoustic signal used for space charge measurements. The distortion resulting from the pulsed voltage can be substantially diminished by modifying the current distribution of the pulsed voltage across the PEA test cell in relation to the piezo amplifier position. It was observed that the physical location of the pulse voltage connection at the test cell electrode had an influence on this electromagnetic interference, measured at the piezo-amplifier circuit.

It is recommended to keep the PEA test cell isolated from the ground, even in cases where the pulsed voltage is injected through the sample HVDC cable shield. The existence of a grounding path creates undesired currents at the PEA test cell during the pulse injection, which can couple with the piezo-sensor and contribute to the distortion. For that reason, the use of decoupled signal acquisition devices, such as the one used in this work, is recommended.

The stray capacitance towards the PEA test cell needs to be considered, as in some cases it might raise the distortion to undesired levels.

In the specific situations where the PEA test cell is required to be grounded, the crosstalk distortion can be reduced without having significant impact in the acoustic magnitude, by increasing the semiconductor distance between the electrode and the PEA test cell, or by increasing the ground path inductance by adding N30 ferrites at the grounding line.

The decision of which method to utilize should consider the available space for the exposure of the semiconductive layer at the HVDC test cable. For the inductance impedance at the PEA test cell grounding, one should consider the trade-off: higher impedance brings less crosstalk but increases the chance of an enhanced transient overvoltage in case of a short circuit.

The use of a coaxial injection for the pulsed voltage did not show significant improvement regarding the crosstalk distortion.

It must be noted that the measured disturbance is dependent on the specific piezo-amplifier circuit configuration, which differs between different PEA test cell designs. Nevertheless, the measured disturbance is related to the magnitude of the interference originated by the applied voltage pulse, meaning that this work demonstrates the influence of the connection configuration of the applied voltage pulse and the resulting magnitude of the disturbance in the piezo-amp circuit.

The results of this work, by means of experimental testing, serve as a guideline for best practices in HVDC cable space charge testing using PEA that minimize signal distortion and allows for simpler post-processing. The design of a PEA setup should take into consideration these factors which have an impact in the crosstalk, especially in configurations where the PEA test cell is grounded as the crosstalk distortion is higher.

6. Conclusions and Recommendations

The purpose of this work was the improvement of the application of PEA method for space charge measurements in solid dielectrics. For this purpose, two objectives were formulated

The first objective was the development of flat samples for reference, which can be used to calibrate and characterize acoustic space charge methods. For this purpose, samples were developed which emulate localized charges in the dielectric bulk and can be utilized to improve the calibration process in relation with the acoustic interface at the electrodes.

For second objective "optimize the application of the pulsed voltage at the PEA method for measurements at full size HVDC cables to enhance the quality of the measured signal with focus on electromagnetic crosstalk", optimized configurations for the pulsed voltage injection and grounding were presented, in which the crosstalk is reduced. These were achieved through experimental analysis in which different arrangements for the PEA method in full size HVDC cables were tested and compared achieving a reduced crosstalk during the application of a pulsed voltage.

6.1. Research Questions

In this section, the conclusions and recommendations addressing the research questions formulated in section 1.3 are presented:

1. **Which is the effect of different electrode materials in the acoustic calibration?**

For the post-processing of the measured signal utilizing the PEA method, it is required to perform deconvolution procedures to compensate for the attenuation of the signal due to the material acoustic losses through which the acoustic wave propagates, this is especially important as the sample thickness increases. The compensation procedure requires to utilize a transfer function whose factors are calculated utilizing the measured signals from the dielectric-electrode interfaces.

As was observed in Section 3.2, the mechanical properties of the electrode materials have a direct impact in the generated acoustic signal at their dielectric-electrode interface.

The use of different materials for the non-measuring electrode (where it is considered as “measuring electrode” the one that has a direct contact with the acoustic sensor) can result in different calculated acoustic attenuation transfer functions for the same dielectric material.

The most accurate transfer function calculation can be achieved when the non-measuring electrode has mechanical properties equal to the dielectric material. This can be achieved by utilizing higher conductive versions of the dielectric such as dispersion carbon black versions, or very thin electrodes backed with the dielectric material. Nevertheless, the electrode-dielectric interface material plays an important role in the behaviour of the space charge which means that the electrode material might not be interchangeable due to the measurement purpose.

In the case where the required non-measurement electrode material properties greatly differ from the dielectric material mechanical properties, the measurement of the acoustic attenuation transfer function can be separately calculated through a thin electrode sample as described in Section 3.2.5, and afterwards apply these factors to the post-processing of the measured signal from the measurement sample of interest.

2. **Can multilayer flat samples be utilized for the characterization and calibration of space charge measurement equipment?**

The use of multilayer samples with internal thin electrodes as the ones described in Section 3.3 can represent a single layer dielectric with known charges in a localized region by means of controlling the applied voltage at the internal electrode. The use of these kind of samples can be utilized for the comparison between expected and actual measured values for PEA measurement experiments which can help to characterize and evaluate the performance of the measurement device. It is important to know that the internal charges induced by the applied internal voltage can recreate space charges across a surface (across the thin internal electrode), and not distributed across a dielectric volume, which limits the scenarios that this kind of samples can emulate.

The use of this kind of samples for the evaluation of the measurement device requires that the sample itself does not accumulate space charge, as the actual charge distribution will differ from the expected values considering only the applied voltages. This presents a limitation for the duration of the measurement and the magnitude of the applied voltage, to avoid a relevant accumulation of space charges in the calibration sample.

3. **Can the pulse injection configuration be optimized to reduce the electromagnetic interaction between the applied pulsed voltage and the piezo sensor in HVDC full size cables PEA measurements?**

The induced electromagnetic distortion due to the pulsed voltage crosstalk with the piezo sensor is influenced by the current path of the applied pulse in relation with the piezo sensor location. It is observed that by modifying the physical connection location of the pulsed voltage connection at the PEA test cell, can substantially diminish the resulting measured distortion.

It is recommended to apply the pulsed voltage connection at the PEA test cell considering the pulse current path as far as possible from the piezo sensor. At the same time, the grounding of the PEA test cell has a negative impact in the crosstalk magnitude as it influences the current distribution across the PEA test cell during the pulse application, so it is recommended to keep it isolated from ground and keep parasitic capacitance towards ground as low as possible.

4. **How can the electromagnetic crosstalk during pulse injection can be reduced when the PEA test cell requires to be grounded in full size HVDC cable measurements?**

As previously described, the grounding of the PEA test cell can have a detrimental effect in the crosstalk between the applied pulsed voltage and the piezo sensor. Nevertheless, there might be cases in which the grounding of the PEA test cell is required, such as in very long periods of cable testing in which it is required the powering of the PEA test cell devices during several days.

Two methodologies were successfully tested which can be employed to diminish the effect of the PEA test cell grounding in the crosstalk magnitude during the pulsed voltage application in the PEA method:

The first method involves utilizing the guard electrodes as the main injection electrode without a direct connection to the PEA test cell. Following this configuration, by increasing the semiconductor distance between the guard electrodes and the PEA test cell the effect of the crosstalk at the measured signal can be reduced.

The second method consists in increasing the inductance of the PEA test cell ground connection. In this work, this was accomplished by the use of N30 ferrites at the grounding line.

For the selection of the method, it should be considered the available space in the HVDC cable for the exposure of the semiconductive layer. At the same time, increasing the inductance of the PEA test cell reduces the crosstalk but increases the possibility of enhanced

transient overvoltage in case of a short circuit. Both methods can be combined for an increased crosstalk reduction.

5. **Can the utilization of a coaxial pulse injection have an impact between the pulsed voltage and piezo-sensor interaction?**

The use of a coaxial structure described in Section 5.3.1.2 for the application of the pulsed voltage at the HVDC cable was tested to analyse its impact in the crosstalk between the piezo sensor and the pulsed voltage. The test results did not indicate a reduction of the measured disturbance due to the crosstalk and showed a behaviour equivalent to the standard injection configuration.

6.2. Recommendations for future work

Samples with internal thin electrodes which can emulate localized charges at the dielectric bulk and be used as reference for measuring equipment utilizing the PEA method were developed for this thesis. The application of these samples can be explored and further developed for alternative acoustic methods such as the Pressure Wave Propagation (PWP) method.

At the same time, these reference samples were studied for flat geometries. It would be of interest to expand this method to coaxial geometries which can enable its utilization in cable measurement systems. This would be of importance for the HVDC technologies, in which most of the space charge interest is towards extruded HVDC cables.

For the pulse injection configuration in full size HVDC cable systems, the use of non-conductive acoustic delay lines can be explored. This should have a direct impact in the reduction of the crosstalk and can simplify the grounding and powering of the sensor electronics utilized at the PEA test cell.

It is recommended for testing and certification companies to get involved in the measurement and analysis of the space charge phenomena for HVDC cables. This includes the compilation of measurement data which can be utilized for the development of standards for the accepted amount and behavior of space charges in HVDC cable systems.

7. Bibliography

1. Mazzanti, G.; Marzinotto., M. *Extruded Cables For High-Voltage Direct-Current Transmission*; Mazzanti, G., Marzinotto, M., Eds.; Wiley-IEEE Press: Hoboken, New Jersey, 2013; ISBN 9781118590423.
2. Sanden, B. *XLPE Cable Insulation Subjected to HVDC Stress: Space Charge, Conduction and Breakdown Strength*; NTNU, Ed.; 1996; ISBN 8247100010, 9788247100011.
3. Born, D. Van Der Investigation of space charge injection, conduction and trapping mechanisms in polymeric HVDC mini-cables. *Thesis* **2011**.
4. Salah Khalil, M. International research and development trends and problems of HVDC cables with polymeric insulation. *IEEE Electr. Insul. Mag.* **1997**, *13*, 35–47, doi:10.1109/57.637152.
5. Takada, T. Space Charge Formation in Dielectrics. *IEEE Trans. Electr. Insul.* **1986**, *EI-21*, 873–879, doi:10.1109/TEI.1986.348996.
6. De Araujo Andrade, M.; Candela, R.; De Rai, L.; Imburgia, A.; Sanseverino, E.R.; Romano, P.; Troia, I.; Viola, F. Different space charge behavior of materials used in AC and DC systems. *Annu. Rep. - Conf. Electr. Insul. Dielectr. Phenomena, CEIDP* **2018**, *2017-Octob*, 114–117, doi:10.1109/CEIDP.2017.8257619.
7. Maeno, Y.; Hirai, N.; Ohki, Y.; Tanaka, T.; Okashita, M.; Maeno, T. Effects of crosslinking byproducts on space charge formation in crosslinked polyethylene. *IEEE Trans. Dielectr. Electr. Insul.* **2005**, *12*, 90–97, doi:10.1109/TDEI.2005.1394019.
8. Li, Z.; Du, B. Polymeric insulation for high-voltage dc extruded cables: challenges and development directions. *IEEE Electr. Insul. Mag.* **2018**, *34*, 30–43, doi:10.1109/MEI.2018.8507715.
9. Mazzanti, G.; Marzinotto., M. 4- Space Charge in HVDC Extruded Insulation: Storage, Effects and Measurements Methods. *Extruded Cables High-Voltage Direct-Current Transm. Res. Dev.* **2013**, 110.
10. Bartnikas, R. Performance characteristics of dielectrics in the presence of space charge. *IEEE Trans. Dielectr. Electr. Insul.* **1997**, *4*, 544–557, doi:10.1109/94.625644.
11. Zhang, Y.; Lewiner, J.; Alquié, C.; Hampton, N. Evidence of strong correlation between space-charge buildup and breakdown in cable insulation. *IEEE Trans. Dielectr. Electr. Insul.* **1996**, *3*, 778–783, doi:10.1109/94.556559.
12. Dissado, L.A.; Mazzanti, G.; Montanari, G.C. The role of trapped space charges in the electrical aging of insulating materials. *IEEE Trans. Dielectr. Electr. Insul.* **1997**, *4*, 496–506, doi:10.1109/94.625642.
13. Malrieu, S.; Notingher, P.; Pacreau, F.; Toureille, A. Influence of space charge on the breakdown of multilayered epoxy: a study by the thermal step method. *IEEE 1997 Annu. Rep. Conf. Electr. Insul. Dielectr. Phenom.* **1997**, *1*, 88–91, doi:10.1109/CEIDP.1997.634565.
14. Li, J.; Zhang, Y.; Xia, Z.; Qin, X.; Peng, Z. Action of space charge on aging and breakdown of polymers. *Chinese Sci. Bull.* **2001**, *46*, 796–800, doi:10.1007/BF02900426.
15. Mazzanti, G.; Montanari, G.C.; Dissado, L.A. Electrical aging and life models: The role of space charge. *IEEE Trans. Dielectr. Electr. Insul.* **2005**, *12*, 876–890, doi:10.1109/TDEI.2005.1522183.
16. Dissado, L.A.; Mazzanti, G.; Montanari, G.C. Elemental strain and trapped space charge in thermoelectrical aging of insulating materials. Part 1: Elemental strain under thermo-electrical-mechanical stress. *IEEE Trans. Dielectr. Electr. Insul.* **2001**, *8*, 959–965, doi:10.1109/94.971452.
17. Mazzanti, G.; Montanari, G.C.; Dissado, L.A. Elemental strain and trapped space charge in thermoelectrical aging of insulating materials: life modeling. *IEEE Trans. Dielectr. Electr. Insul.* **2001**, *8*, 966–971, doi:10.1109/94.971453.
18. Das, S.; Gupta, N. Effect of ageing on space charge distribution in homogeneous and composite dielectrics. *IEEE Trans. Dielectr. Electr. Insul.* **2015**, *22*, 541–547, doi:10.1109/TDEI.2014.004467.

19. Liu, Y.; Liu, H.; Yu, L.; Li, Y.; Gao, L. Effect of thermal stress on the space charge distribution of 160 kV HVDC cable insulation material. *IEEE Trans. Dielectr. Electr. Insul.* **2017**, *24*, 1355–1364, doi:10.1109/TDEI.2017.006196.
20. Chen, X.; Dai, C.; Yu, L.; Jiang, C.; Zhou, H.; Tanaka, Y. Effect of thermal ageing on charge dynamics and material properties of 320 kV HVDC XLPE. *IEEE Trans. Dielectr. Electr. Insul.* **2019**, *26*, 1797–1804, doi:10.1109/TDEI.2019.008160.
21. Abou-Dakka, M.; Bulinski, A.; Bamji, S.S. Effect of additives on the performance of cross-linked polyethylene subjected to long term single and periodically reversed polarity DC voltage. *IEEE Trans. Dielectr. Electr. Insul.* **2013**, *20*, 654–663, doi:10.1109/TDEI.2013.6508769.
22. Hu, S.; Wang, W.; Dang, B.; Zhou, Y.; Yuan, C.; Hu, J.; Li, Q.; He, J. Thermal properties and space charge behavior of thermally aged polypropylene/elastomer blends nanocomposite. *IEEE Trans. Dielectr. Electr. Insul.* **2020**, *27*, 521–527, doi:10.1109/TDEI.2019.008602.
23. Holé, S.; Ditchi, T.; Lewiner, J. Non-destructive methods for space charge distribution measurements: What are the differences? *IEEE Trans. Dielectr. Electr. Insul.* **2003**, *10*, 670–677, doi:10.1109/TDEI.2003.1219652.
24. Imburgia, A.; Miceli, R.; Sanseverino, E.R.; Romano, P.; Viola, F. Review of space charge measurement systems: acoustic, thermal and optical methods. *IEEE Trans. Dielectr. Electr. Insul.* **2016**, *23*, 3126–3142, doi:10.1109/TDEI.2016.7736878.
25. Zhang, Y.; Li, J.; Peng, Z.; Qin, X.; Xia, Z. Research of space charge in solid dielectrics in China. *IEEE Electr. Insul. Mag.* **2001**, *17*, 25–30, doi:10.1109/57.954575.
26. Liu, R.; Törnkvist, C.; Jeroense, M. Space-charge measurement technologies and their potential applications. *Sensors Mater.* **2017**, *29*, 1089–1098, doi:10.18494/SAM.2017.1506.
27. Imburgia, A.; Romano, P.; Caruso, M.; Viola, F.; Miceli, R.; Riva Sanseverino, E.; Madonia, A.; Schettino, G. Contributed Review: Review of thermal methods for space charge measurement. *Rev. Sci. Instrum.* **2016**, *87*, 111501, doi:10.1063/1.4968029.
28. IEEE *IEEE Recommended Practice for Space Charge Measurements on High-Voltage Direct-Current Extruded Cables for Rated Voltages up to 550 kV. IEEE Std 1732™-2017*; 2017; ISBN 978-1-5044-3917-6.
29. IEC 62758 *Calibration of space charge measuring equipment based on the pulsed electro-acoustic (PEA) measurement principle*; IEC, Ed.; 2012; ISBN 9179-2-83220-336-1.
30. Takeda, T.; Hozumi, N.; Suzuki, H.; Fujii, K.; Terashima, K.; Hara, M.; Mutrata, Y.; Wantanabe, K.; Yoshida, M. Space charge behavior in full-size 250 kV DC XLPE cables. *IEEE Trans. Power Deliv.* **1998**, *13*, 28–39, doi:10.1109/61.660842.
31. Terashima, K.; Suzuki, H.; Hara, M.; Watanabe, K. Research and development of ±250 kV DC XLPE cables. *IEEE Trans. Power Deliv.* **1998**, *13*, 7–16, doi:10.1109/61.660837.
32. Takada, T. Acoustic and optical methods for measuring electric charge distributions in dielectrics. *Conf. Electr. Insul. Dielectr. Phenom. (CEIDP), Annu. Rep.* **1999**, *1*, 1–14, doi:10.1109/ceidp.1999.804581.
33. Mazzanti, G.; Chen, G.; Fothergill, J.C.; Hozumi, N.; Li, J.; Marzinotto, M.; Mauseth, F.; Morshuis, P.; Reed, C.; Tzimas, A.; et al. A protocol for space charge measurements in full-size HVDC extruded cables. *IEEE Trans. Dielectr. Electr. Insul.* **2015**, *22*, 21–34, doi:10.1109/TDEI.2014.004557.
34. Fu, M.; Dissado, L.A.; Chen, G.; Fothergill, J.C. Space charge formation and its modified electric field under applied voltage reversal and temperature gradient in XLPE cable. *IEEE Trans. Dielectr. Electr. Insul.* **2008**, *15*, 851–860, doi:10.1109/TDEI.2008.4543123.
35. Ma, Z.; Yang, L.; Bhutta, M.S.; Bian, H.; Khan, M.Z. Effect of Thickness on the Space Charge Behavior and DC Breakdown Strength of Cross-Linked Polyethylene Insulation. *IEEE Access* **2020**, *8*, 85552–85566, doi:10.1109/ACCESS.2020.2990759.
36. Bodega, R. Space charge accumulation in polymeric high voltage DC cable systems, Delft University of Technology, 2006.
37. Kreuger, F.H. *Industrial High DC Voltage*; 1995;
38. Murata, Y.; Kashiyama, S.; Igi, T.; Sakamaki, M.; Abe, K.; Katakai, S. Advanced HVDC XLPE cable

and accessories. In Proceedings of the 9th IET International Conference on Advances in Power System Control, Operation and Management (APSCOM 2012); Institution of Engineering and Technology, 2012; pp. 59–59.
39. Li, J.; Du, B.X.; Kong, X.X.; Li, Z.L. Nonlinear conductivity and interface charge behaviors between LDPE and EPDM/SiC composite for HVDC cable accessory. *IEEE Trans. Dielectr. Electr. Insul.* **2017**, *24*, 1566–1573, doi:10.1109/TDEI.2017.006198.
40. Takada, T.; Tohmine, T.; Tanaka, Y.; Li, J. Space charge accumulation in double-layer dielectric systems-measurement methods and quantum chemical calculations. *IEEE Electr. Insul. Mag.* **2019**, *35*, 36–46, doi:10.1109/MEI.2019.8804333.
41. Mizutani, T. Space charge measurement techniques and space charge in polyethylene. *IEEE Trans. Dielectr. Electr. Insul.* **1994**, *1*, 923–933, doi:10.1109/94.326659.
42. Bodega, R.; Morshuis, P.H.F.; Smit, J.J. Space charge measurements on multi-dielectrics by means of the pulsed electroacoustic method. *IEEE Trans. Dielectr. Electr. Insul.* **2006**, *13*, 272–281, doi:10.1109/TDEI.2006.1624272.
43. Nakamura, K.; Wada, Y. Piezoelectricity, pyroelectricity, and the electrostriction constant of poly(vinylidene fluoride). *J. Polym. Sci. Part A-2 Polym. Phys.* **1971**, *9*, 161–173, doi:10.1002/pol.1971.160090111.
44. M. J. P. Jeroense Charges and discharges in hvdc cables, Delft University of Technology, 1997.
45. Maeno, T.; Futami, T.; Kushibe, H.; Takada, T.; Cooke, C.M. Measurement of spatial charge distribution in thick dielectrics using the pulsed electroacoustic method. *IEEE Trans. Electr. Insul.* **1988**, *23*, 433–439, doi:10.1109/14.2384.
46. Imburgia; Antonino Modelling of Pulsed Electro Acoustic Method for Space Charge Detection on Single and Multilayer Dielectrics, Università degli Studi di Palermo, 2018.
47. Chen, G.; Chong, Y.L.; Fu, M. Calibration of the pulsed electroacoustic technique in the presence of trapped charge. *Meas. Sci. Technol.* **2006**, *17*, 1974–1980, doi:10.1088/0957-0233/17/7/041.
48. Sachse, W.; Pao, Y. On the determination of phase and group velocities of dispersive waves in solids. *J. Appl. Phys.* **1978**, *49*, 4320–4327, doi:10.1063/1.325484.
49. Li, Y.; Murata, K.; Tanaka, Y.; Takada, T.; Aihara, M. Space Charge Distribution Measurement in Lossy Dielectric Materials by Pulsed Electroacoustic Method. *Proc. 1994 4th Int. Conf. Prop. Appl. Dielectr. Mater.* **1994**, *2*, 725–728, doi:10.1109/ICPADM.1994.414113.
50. Hussaini, H.; Ahmad Adam, A.; Abimbola Susan, A. Review of Space-charge Measurement using Pulsed Electro- Acoustic Method: Advantages and Limitations. *J. Eng. Res. Appl. www.ijera.com ISSN* **2015**, *5*, 2248–962290.
51. Li, Y.; Yasuda, M.; Takada, T. Pulsed Electroacoustic Method For Measurement Of Charge Accumulation In Solid Dielectrics. *IEEE Trans. Dielectr. Electr. Insul.* **1994**, *1*, 188–195, doi:10.1109/94.300251.
52. Vissouvanadin, B.; Vu, T.T.N.; Berquez, L.; Roy, S.; Teyssèdre, G.; Laurent, C. Deconvolution techniques for space charge recovery using pulsed electroacoustic method in coaxial geometry. *IEEE Trans. Dielectr. Electr. Insul.* **2014**, *21*, 821–828, doi:10.1109/TDEI.2013.004163.
53. Morshuis, P.; Jeroense, M. Space charge measurements on impregnated paper: A review of the PEA method and a discussion of results. *IEEE Electr. Insul. Mag.* **1997**, *13*, 26–35, doi:10.1109/57.591529.
54. Maeno, T. Calibration of the pulsed electroacoustic method for measuring space charge density. *IEEE Japan* **1999**, *119*, 1114–1119.
55. Bodega, R.; Morshuis, P.H.F.; Smit, J.J. Space charge measurements on multi-dielectrics by means of the pulsed electroacoustic method. *IEEE Trans. Dielectr. Electr. Insul.* **2006**, *13*, 272–281, doi:10.1109/TDEI.2006.1624272.
56. Huang, M.; Zhou, Y.; Chen, W.; Lu, L.; Jin, F.; Huang, J. Calibration of pulsed electroacoustic method considering electrode-dielectric interface status and porosity. *Jpn. J. Appl. Phys.* **2014**, *53*, doi:10.7567/JJAP.53.106601.

57. Biwa, S.; Nakajima, S.; Ohno, N. On the Acoustic Nonlinearity of Solid-Solid Contact With Pressure-Dependent Interface Stiffness. *J. Appl. Mech.* **2004**, *71*, 508, doi:10.1115/1.1767169.
58. Takada, T.; Holboell, J.; Toureille, A.; Densley, J.; Hampton, N.; Castellon, J.; Hegerberg, R.; Henriksen, M.; Montanari, G.C.; Nagao, M.; et al. Guide for Space Charge Measurements in Dielectrics and Insulating Materials. *Tech. Broch. TF D1.12.1* **2005**, 1–6.
59. Holbplll, J.T.; Henriksen, M.; Brandby, D.- Dielectric sample with narrow bulk charge distribution. **2001**, 493–496.
60. Conference, A.R.; Holbsll, J.T.; Henriksen, M.; Rasmussen, C. Dielectric sample with two-layer charge distribution. *Most* **2002**, 648–651.
61. Cheeke, J.D.N. *Fundamentals and applications of ultrasonic waves*; 2nd editio.; Boca Raton: CRC Press, 2012;
62. Blitz, J. *Fundamentals of ultrasonics*; 2nd editio.; London: Butterworths, 1967;
63. Li, Y.; Murata, K.; Tanaka, Y.; Takada, T.; Aihara, M. Space charge distribution measurement in lossy dielectric materials by pulsed electroacoustic method. In Proceedings of the Proceedings of 1994 4th International Conference on Properties and Applications of Dielectric Materials (ICPADM); IEEE, 1994; Vol. 2, pp. 725–728.
64. Holé, S. Behind space charge distribution measurements. *IEEE Trans. Dielectr. Electr. Insul.* **2012**, *19*, 1208–1214, doi:10.1109/TDEI.2012.6259992.
65. Wu, K.; Cheng, C. Interface charges between insulating materials. *IEEE Trans. Dielectr. Electr. Insul.* **2017**, *24*, 2633–2642, doi:10.1109/TDEI.2017.006442.
66. Das, S.; Gupta, N. Interfacial charge behaviour at dielectric - Dielectric interfaces. *IEEE Trans. Dielectr. Electr. Insul.* **2014**, *21*, 1302–1311, doi:10.1109/TDEI.2014.6832278.
67. Bodega, R.; Morshuis, P.H.F.; Redjosentono, E.; Smit, J.J. Dielectric interface characterization by means of space charge measurements. In Proceedings of the 2003 Annual Report Conference on Electrical Insulation and Dielectric Phenomena; IEEE, 2003; pp. 728–733.
68. Fu, M.; Chen, G.; Davies, A.E.; Tanaka, Y.; Takada, T. A modified PEA space charge measuring system for power cables. In Proceedings of the Proceedings of the 6th International Conference on Properties and Applications of Dielectric Materials (Cat. No.00CH36347); IEEE; Vol. 1, pp. 104–107.
69. Imburgia, A.; Romano, P.; Chen, G.; Rizzo, G.; Riva Sanseverino, E.; Viola, F.; Ala, G. The Industrial Applicability of PEA Space Charge Measurements, for Performance Optimization of HVDC Power Cables. *Energies* **2019**, *12*, 4186, doi:10.3390/en12214186.
70. Zheng, H. Application of PEA Technique to Space Charge Measurement in Cylindrical Geometry HV Cable Systems, University of Leicester, 2015.
71. Wang, X.; Hao, J.Q.; Xiong, J.Z.; Chen, C.; Wu, K.; Fu, M.L.; Chen, G. Comparison and analysis of three pulse injection methods in the pulsed electroacoustic technique used for long cables. *IEEE Electr. Insul. Mag.* **2018**, *34*, 17–31, doi:10.1109/MEI.2018.8430040.
72. Holé, S. Behind space charge distribution measurements. *IEEE Trans. Dielectr. Electr. Insul.* **2012**, *19*, 1208–1214, doi:10.1109/TDEI.2012.6259992.
73. Choo, W. Space charge determination in HVDC power cable and its influence on electric field. *Thesis* **2010**.
74. Takada, T.; Holboell, J.; Toureille, A.; Densley, J.; Hampton, N.; Castellon, J.; Hegerberg, R.; Henriksen, M.; Montanari, G. C.; Nagao, M.; Morshuis, P. Space charge measurement in dielectrics and insulating materials. *Tech. Broch. 288 Cigre task force D1.12.01* **2006**, 1–51.
75. Zhang Yewen; Yang Baitun; Tu Demin; Liu Yaonan Measuring distribution of carrier trap energy state density at interface of dielectric with step pressure wave method. In Proceedings of the Conference on Electrical Insulation and Dielectric Phenomena; IEEE, 1989; pp. 303–308.

List of Publications

1. Mier-Escurra, G.; Rodrigo-Mor, A.; Vaessen, P. A Calibration Method for Acoustic Space Charge Measurements Using Multilayer Samples. Sensors 2018, 18, 2508, doi:10.3390/s18082508.

2. Mier Escurra, G.; Rodrigo Mor, A.; Vaessen, P. Influence of the Pulsed Voltage Connection on the Electromagnetic Distortion in Full-Size HVDC Cable PEA Measurements. Sensors 2020, 20, 3087, doi:10.3390/s20113087.

3. Mier Escurra, G.; Rodrigo Mor, A.; Castro, L.C.; Vaessen, P. PEA Electromagnetic Distortion Reduction by Impedance Grounding and Pulsed Voltage Electrode Configurations. Sensors 2021, 21, 5837, doi:10.3390/s21175837.

4. Mier-Escurra, G.A.; Rodrigo-Mor, A. Influence of Electrode Material in Acoustic Attenuation Factors Calculation in Space Charge Measurements. In Proceedings of the 2019 2nd International Conference on Electrical Materials and Power Equipment (ICEMPE); IEEE, 2019; pp. 166–169.

5. Mier-Escurra, G.A.; Rodrigo-Mor, A. Influence of the pulse voltage injection configuration on the electromagnetic distortion in space charge measurements using the PEA method. In Proceedings of the 2020 IEEE Electrical Insulation Conference (EIC); IEEE, 2020.

Acknowledgements

I would like to use this section to say thanks to all the people that helped me finalize this work. Keep in mind that if your name is not mentioned here, it is just a common flaw in my memory, but it does not mean that you did not play an important role during this process, it is just me being me.

For starters, I would like to give my thanks to my co-promotor **Dr. Armando Rodrigo Mor** and promotor **Prof. ir. Peter Vaessen** who have guided me through the project, sharing your knowledge, energy, positivism (and patience of course) which have allowed me to reach this point. Thank you, **Armando**, for your great support and discussions that we have shared and of course for hearing me out and discussing every idea or "theory" no matter how crazy it sounded. Yo creo que nos quedó bien el trabajo y pues a ver si nos seguimos topando por la vida. Thank you, **Peter**, also for your continuous support, guiding me, keeping me on track and with my feet on the ground. I really enjoy our conversations work and non-work related.

I would also like to say thanks to my promotor Prof. dr. ir. **Pavol Bauer** for allowing me to follow this PhD project and your support through the whole process of it. I also appreciate your involvement with all of us including the football matches and of course the great BBQs that you hosted

Special thanks to the committee members **Peter Palenski**, **Peter Van der Wielen**, **Miguel Mudarra López**, **Stéphane Holé** and **Arno Smets** for their time reading my thesis and sharing your important notes and comments.

Sharmila Rattansingh thanks for everything, all your help in administrative things and for all the conversations and laughs that we had, you are a very enjoyable person and really one of the best the department has.

Of course, I would like to thank the "HV half" of the department with who I spent most of the time and who became good friends. Thank you, **Luis Carlos Castro**, for all your help in the testing and in the great conversations in and outside the university, you were of really great help during the last stressful moments. Thanks to **Fabio Muñoz Muñoz** "the wise man" for all your help and sharing of your knowledge, I really enjoy our conversations and discussions (I secretly celebrated the few ones that I won); together with **Luis**, we had the "all mighty just Spanish speaker's office". **Djure Wikkerink**, thanks for all your support and good vibes, from all in the group you were the one that most of the times stayed till the end with me for

celebrations; I really like the way you see and analyse life. **Huifei Jin**, even though your stay during my time was short, thanks for teaching a lot of the equipment for the HV and all the talks that we shared, I really like that we still see each other once in a while. **Dhanashree Ganeshpure**, it was very nice to talk to you and seeing you around. Thank you, **Jiayang Wu**, for all the time we shared and enjoyed with me even when you were busy; I know I tended to distract you, is just that I enjoyed talking to you. Nice that we still see each other at work (during the writing of this text). Last but not least, **Alessandro Iannarelli** thanks for all your support and friendship during the PhD, work, and life; I know we will continue to see each other (I know you moved to Utrecht for me… don't deny it), sharing talks and beers.

I would like to say thanks to everyone from laboratory of HV. Thanks **Wim Termorshuizen** and **Remko Koornneef** for helping me build all the required components (and more) with your impressive technical and craftsmanship skills. Thanks to **Paul van Nes** and **Radek Heller** for your support and understanding. Also thank you **Geert Jan Kamphuis**, who I met at the last stage and helped me finish several tests.

Thanks to the rest of my non-HV department colleagues, regrettably my contact you was slightly less, but still very important for me. **Udai Shipurkar** for being a superb tour guide during our India trip together with **Pabel Purgát**, **Mladen Gagić**, and **Minos Kontos**; I really enjoyed the trip will all of you. **Lucia Beloqui**, your energy always brings a spark to the conversations which make them quite enjoyable. **Aditya Shekhar**, you seemed you were not afraid to share your thoughts, I believe you are a very interesting person. **Soumya Bandyopadhyay**, you are one of my oldest friends in the Netherlands, I really enjoy your company and conversations, I hope we keep seeing each other. Special thanks for all the talks, laughs, coffee and beers shared with **Nils van der Blij**, **Babak Gholizad**, **Nishant Narayan**, **Jianning Dong**, **Gautham Chandra Ram Mouli**, **Victor Vega Garita**, **Laurens Mackay**, **Marco Stecca**, **Wiljan Vermeer**, **Yunhe Yu**, **Farshid Norouzi** and **Wenli Shi**.

Thanks a lot, to all my **external friends (outside of the university)** who have supported, exchanged thoughts, and kept me sane during stressful times; the list is long, and I don't want to make long lists, but be aware that I appreciate all your inputs for this work and for the journey called life.

Thanks to **DNV**, specially to **Edward Nagel** and **Riaan Marshal**, for their support and understanding during the final stages of my PhD project; it is really appreciated. I would also like to thank **Hong He** for all your help and support during the experiments at KEMA laboratories, it is really nice that we still share some projects at DNV once in a while.

I would like to give my thanks to **CONACYT** for giving me the opportunity to study abroad, leading to this accomplishment.

I would like to thank my **brothers** who directly and indirectly have supported me to go on and accomplish this work. **Erik Mier** for always keeping in touch and having conversations, even though we are some distance apart. Special thanks to my brother **Christian Mier**, who

by following a similar professional path as mine has allowed us to discuss and share technical conversations in a special way which I do not have with anyone else and which I really enjoy.

Esther, thanks for being at my side and helping me in whichever way you could. Thanks for hearing my frustrations and pushing me every time I needed it (despite my stubbornness) which kept me sane on several occasions. I can be a little crazy and hard to handle but somehow you have managed to like that… at least most of the time.

Finalmente quiero agradecer a **mis padres** quien me han apoyado desde que tengo memoria (se que incluso desde antes). Siempre han creído en mí (aun cuando yo mismo no lo he hecho) y me han guiado a ser una mejor persona, no solo profesionalmente, pero en todos los aspectos de la vida. Agradezco el gran interés que muestran por lo que hago, y por las discusiones que tenemos las cuales son bastante interesantes ya que ustedes me brindan un punto de vista diferente e interesante al que estoy acostumbrado.

For all the rest, as I am sure that I missed a lot of people who directly or indirectly deserve my acknowledgements for helping me finish this work, I say thanks a lot.

Curriculum Vitae

Guillermo Andres Mier Escurra was born on the 12th of August 1986 in Aguascalientes, México. He received his B.S. degree in Mechanical Electrical Engineering from the Instituto Tecnológico y de Estudios Superiores de Monterrey (ITESM) in 2009. He worked in the power electric industry for 4 years before joining a MSc program in 2013. In 2015 he received the MSc degree of Electrical Engineering at Delft University of Technology. In 2016 he joined the Electrical Sustainable Department at Delft University of Technology as a PhD candidate. His research topic is “Space Charge Pulsed Electro Acoustic Method, Calibration for Flat Samples and Crosstalk Reduction for HVDC Cable Measurements”. Since February 2020, he became a consultant in the Transmission and Distribution Technology group in DNV, Arnhem, the Netherlands.